Development of an SRF Reduced-beta Cavity for the Injector of the S-DALINAC

Entwicklung einer SRF-Kavität mit reduziertem Beta für den Injektor des S-DALINAC
Zur Erlangung des akademischen Grades Doktor-Ingenieur (Dr.-Ing.)
genehmigte Dissertation von Dmitry Bazyl aus Klintsy
Tag der Einreichung: 17.01.2019, Tag der Prüfung: 20.05.2019
Darmstadt — D 17

1. Gutachten: Prof. Dr.-Ing. Herbert De Gersem
2. Gutachten: Prof. Dr. Joachim Enders

TECHNISCHE
UNIVERSITÄT
DARMSTADT

Fachbereich Elektrotechnik
und Informationstechnik
Institut für Theorie
Elektromagnetischer Felder

Development of an SRF Reduced-beta Cavity for the Injector of the S-DALINAC
Entwicklung einer SRF-Kavität mit reduziertem Beta für den Injektor des S-DALINAC

Genehmigte Dissertation von Dmitry Bazyl aus Klintsy

1. Gutachten: Prof. Dr.-Ing. Herbert De Gersem
2. Gutachten: Prof. Dr. Joachim Enders

Tag der Einreichung: 17.01.2019
Tag der Prüfung: 20.05.2019

Darmstadt — D 17

Bitte zitieren Sie dieses Dokument als:
URN: urn:nbn:de:tuda-tuprints-87910
URL: http://tuprints.ulb.tu-darmstadt.de/8791

Dieses Dokument wird bereitgestellt von tuprints,
E-Publishing-Service der TU Darmstadt
http://tuprints.ulb.tu-darmstadt.de
tuprints@ulb.tu-darmstadt.de

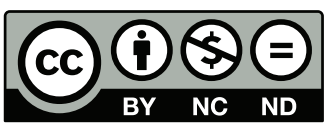

Die Veröffentlichung steht unter folgender Creative Commons Lizenz:
Namensnennung – Keine kommerzielle Nutzung – Keine Bearbeitung 4.0 International
http://creativecommons.org/licenses/by-nc-nd/4.0/

Zusammenfassung

Die neueste wichtige Verbesserung des supraleitenden Darmstädter Elektronenlinearbeschleunigers (Englisch: superconducting Darmstadt electron linear accelerator, S-DALINAC) erlaubte die ersten Funktionsprüfungen in einem Energierückgewinnungsmodus (Englisch: energy recovery linac, ERL) durchzuführen. Der Betrieb eines Beschleunigers als ERL stellt strenge Anforderungen an viele Bestandteile des Beschleunigers sowohl die Qualität des beschleunigten Strahls betreffend als auch insbesondere an die Energieverteilung innerhalb des Teilchenpakets. Gegenwärtig wird eine erhebliche Energieverteilung in der Capture Section des S-DALINAC beobachtet. Diesbezüglich soll die Capture Section des S-DALINAC Injectors verbessert werden, damit das Wachstum der Energieverteilung verringert wird.

In dieser Arbeit wird der Entwicklungsprozess einer reduzierten-β-Kavität mit 6 Zellen diskutiert. In diesem Fall ist das Design der SRF-Kavität nicht auf Simulationen des elektromagnetischen Feldes begrenzt. Es beinhaltet zudem Berechnungen der longitudinalen Strahldynamik und eine Untersuchung des mechanischen Kavitätsmodells. Die zentrale Herausforderung bestand darin, einen optimalen Verbesserungsvorschlag zu finden, der den widersprüchlichen Anforderungen mit minimierten Investitionskosten gerecht wird. In der Arbeit werden Ergebnisse von multiphysikalischen Simulationen und einer qualitativen Analyse diskutiert, die erlauben, Entscheidungen in Bezug auf Design der SRF-Kavität zu treffen. Erwartungsgemäß wird die vorgeschlagene 6-zellige SRF-Kavität Ende 2019 hergestellt. Die Inbetriebnahme ist für das Jahr 2020 geplant.

Abstract

A recent major upgrade of the superconducting - Darmstadt linear accelerator (S-DALINAC) allowed to conduct the first operational tests in an energy recovery linac (ERL) mode. The ERL operating regime imposes strict requirements for many accelerator components as well as for the accelerated beam quality and the beam energy spread in particular. At present, a significant beam energy spread is being observed in the capture section of the S-DALINAC. In that regard, the capture section part of the S-DALINAC injector needs to be upgraded in order to reduce the beam energy spread growth.

In this work, the 6-cell reduced-β cavity development process is discussed and a final cavity design is proposed. The SRF cavity design is not limited by electromagnetic field simulations, but also includes the longitudinal beam dynamics computations and the cavity mechanical model investigation. The main challenge was to find an optimal upgrade solution that would satisfy contradictory requirements with minimised investments costs. The results of multi-physics simulations and qualitative analysis that allowed to make decisions related to the SRF cavity design considerations are discussed. The suggested 6-cell SRF cavity is expected to be manufactured by the end of 2019. The cavity commissioning tests are planned in 2020.

Contents

1 Introduction

One of the first charged particle accelerators have been developed in the early thirties of last century with the aim of conducting fundamental studies in the field of nuclear physics. From the beginning of particle accelerator development and to the present day, the attained maximum energies of the accelerated charged particles increased linearly with the years [1]. The rapid development of accelerator science and the desire to increase the maximum energies of the accelerated particles was not a goal in itself, but it has been dictated by the development of nuclear physics and the high energy physics that emerged from it. The first accelerators made it possible to accelerate particles to energies of the order of several MeV. Presently, the beam in the Large Hadron Collider (LHC) reaches a maximal energy of 6.5 TeV.

In addition to the use of charged particle accelerators in fundamental research, particle accelerators have been designed for other purposes as well. One of the most important applications is found in the field of medicine. For example, relatively compact accelerators are used for proton therapy of human cancer [2]. In addition, particle accelerators are widely used for safety screening systems [3] and sterilisation of medical devices and food [4].

In general, particle accelerators can be distinguished in two categories: linear and circular. The accelerator type is defined by the trajectory of the accelerated particles. Accelerators of charged particles are complex and are often large installations that consists of many components. Nevertheless, it is possible to list some of the key components that are present in most of the accelerators today: particle sources, radio-frequency (RF) cavities that provide the energy to particles, and magnets, which are used to guide the particles beam. This work is dedicated to the RF cavity development for the Superconducting - Darmstadt Linear Accelerator (S-DALINAC) in order to improve the quality of the accelerated electron beams.

1.1 S-DALINAC

One of the contemporary charged particle accelerators used for fundamental research in nuclear physics is the S-DALINAC, which is one of the first operational superconducting accelerators[1] worldwide [5]. The S-DALINAC layout is illustrated in Fig. 1.1. The principle of its operation can be explained in the following way. Depending on the experiment type, the electron beam is either produced by a thermionic gun (TG) with an injection energy of 250 keV or by a spin-polarised electron gun (SPG) with an injection energy[2] of up to 200 keV [6]. After the particle stream is produced by one of the guns it is guided to the beam preparation section, where it is formed into an electron bunch

[1] Historically, S-DALINAC is the third superconducting accelerator in the world.

[2] With taking into account the planned SPG upgrade.

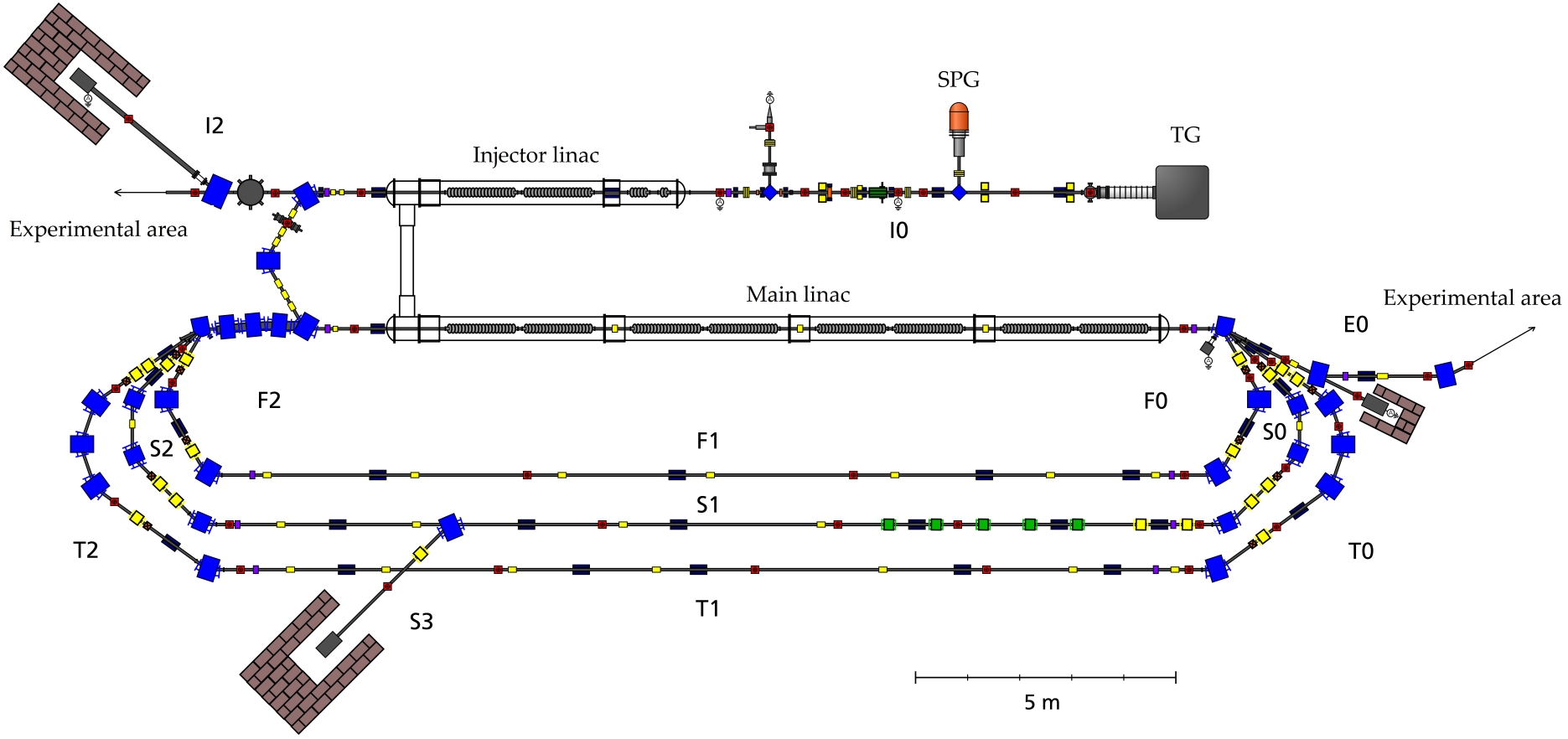

Figure 1.1: Floorplan of the S-DALINAC.

train with a bunch repetition rate of 3 GHz and an individual bunch length of 5 pS rms. Further on, the beam is accelerated to an energy of up to 10 MeV by the injector linac that consists of three superconducting radio-frequency (SRF) accelerating cavities operated at a resonance frequency of 3 GHz. After that, the beam can be either transferred to the low-energy experimental area, or the beam trajectory is bent by a magnetic field, that is produced by magnets, in a way such that the beam enters the main linac, where it is accelerated to an energy of up to 40 MeV. Further on, the 40 MeV beam can be transferred to the experimental area or it can be further accelerated in the main linac a second, third and fourth time up to an energy of 130 MeV using three recirculation beam-lines (F1, T1, S1).

The third recirculation beam line (S1) has been installed in 2016. The installation allowed to operate SRF cavities of the main linac at a lower accelerating gradient and, as a consequence, allowed to reduce the cryogenic load of the main linac. In addition, and most importantly, the third recirculation beam-line allowed to operate the S-DALINAC in the Energy Recovery Linac (ERL) mode [7]. Thus, besides experiments such as electron scattering, it became possible to carry out ERL tests of the accelerator and to investigate its performance in this operating regime.

Presently, a significantly increased energy spread of the accelerated beam is being observed at the S-DALINAC. The beam energy spread growth originates from the capture section of the S-DALINAC injector linac that is implemented in order to pre-accelerate the low-energy electron beams. The reason for the increased energy spread growth is explained by two factors. First, one of two SRF cavities of the capture section is permanently out of operation due to technical reasons and, at the moment, the beam is captured by an SRF 5-cell $\beta_g = 1$ cavity. Besides the absence of the necessary synchronisation between the accelerating field of the 5-cell cavity and the beam, recently, a notable transverse mechanical deformation of the 5-cell cavity has been reported. The transverse cavity deformation leads to a beam acceleration with an off-set from the designed beam trajectory. This leads to a significant growth of the beam transverse size. As a result, the beam quality does not match the designed values at the S-DALINAC.

The goal of this work is to develop a new SRF accelerating cavity in order to replace the 5-cell cavity with the aim to improve the quality of the beam at the S-DALINAC. The motivation for the upgrade is discussed in detail in Chapter 3. In general, the SRF cavity design mainly includes electromagnetic field simulations. However, the new cavity is intended to accelerate low energy electron beams with relative velocity values of 0.7 (70 % of the speed of light c). In that regard, a longitudinal particle beam dynamics investigation is required due to the significant beam velocity changes during the acceleration in the capture section. Furthermore, the new SRF cavity must be stable and reliable in operation. Hence, a careful analysis of the mechanical behaviour of the new cavity has been carried out.

The complex multi-physics design challenge in this work has been convoluted by the minimised investment cost requirement for the capture section upgrade. Several cavity layouts have been considered for the upgrade. The outcome of this dissertation is the proposal to replace the 5-cell $\beta_g = 1$ cavity with a 6-cell reduced-β SRF cavity. The replacement will allow to accelerate the beam in the capture section to velocities of up

to $\beta = 0.97$ with a minimised relative energy spread growth. Taking into account the fact that the beam energy spread originating from the injector linac can not be corrected in the main linac, the capture section upgrade will improve the overall beam quality at the S-DALINAC. The investment costs has been minimised by designing a cavity that is compatible with the present cooling cryostat and tuning system of the 5-cell cavity.

2 Charged Particles Acceleration in the Radio-frequency Fields

Presently, radio-frequency (RF) cavities are implemented in order to increase the energy of the charged particles in particle accelerators. The core part of this work is dedicated to superconducting RF (SRF) cavity design. Due to the fact that the new SRF cavity is intended to accelerate low energy electron beams, the beam quality of which is especially sensitive to the electric field errors in RF cavities, some theoretical aspects of longitudinal beam dynamics in the RF field are introduced shortly in Section 2.1. For the extensive theory related to the beam dynamics in particle accelerators the reader is referred to [8] and [9]. Further on, the RF cavity fundamentals as well as the principle differences between normal conducting RF cavities and SRF cavities are discussed in Section 2.2 and Section 2.3, respectively.

2.1 Some Aspects of the Longitudinal Beam Dynamics in RF Linear Accelerators

A particle accelerator, in which the trajectory of accelerated charged particles is represented, in general, by a straight line, is classified as a linear accelerator or *linac*. The motion of a particle with velocity $\vec{v}$ and charge q is determined by the Newton-Lorentz equation:

$$\vec{F} = \frac{\mathrm{d}\vec{p}}{\mathrm{d}t} = q\left(\vec{E} + \vec{v} \times \vec{B}\right). \tag{2.1}$$

The magnetic field $\vec{B}$ determines the trajectory of the particle, while the electric field $\vec{E}$ determines its energy gain.

Currently, most commonly used devices for charged particles acceleration are RF resonators (cavities) operated with time-harmonic standing electromagnetic waves. The electromagnetic field distribution in resonators is chosen in a way such that the magnetic field is absent at the particle trajectory and the electric field has a component with a direction along the particle motion. Hence, for a particle accelerated in the accelerating RF cavity, (2.1) can be written as:

$$\vec{F} = \frac{\mathrm{d}\vec{p}}{\mathrm{d}t} = q\vec{E}. \tag{2.2}$$

Now, consider the standing electromagnetic wave in the RF resonator that consist of a single accelerating RF gap with the electric field distribution, as it is schematically shown in Fig. 2.1.

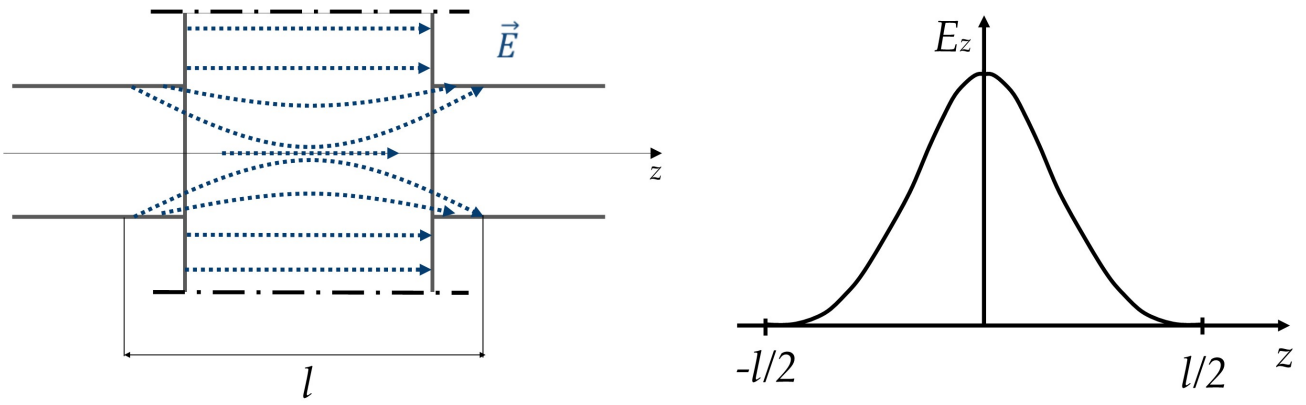

Figure 2.1: Left: Electric field distribution in the gap. Right: Electric field amplitude as a function of the longitudinal coordinate.

Next, assume that the charged particle only interacts with the electric field on the central axis z of the RF gap that is expressed as:

$$E_z(r,z,t) = E_z(0,z,t) = E_z(z)\cos(\omega t(z) + \phi), \tag{2.3}$$

where $t(z) = \int_0^z \frac{\mathrm{d}z}{\mathrm{d}v(z)} dz$ is the time at which the particle is at z and $E_z(z)$ is the longitudinal electric field amplitude at z. The particle's origin is chosen within the gap at time $t = 0$. For convenience, also assume that the *RF phase* ϕ of the RF field is relative to the field crest. The particle travelling along the z axis will interact with the electric field and will obtain the following kinetic *energy gain* [10]:

$$\Delta W = q \int_{-l/2}^{l/2} E_z(z)\cos(\omega t(z) + \phi)\, dz. \tag{2.4}$$

The particle travels with the finite velocity through the time varying electric field in the gap. Hence, the particle will not always 'see' the maximum field amplitude during its transit along the gap. In other words, a particle that is accelerated in a constant direct current (dc) field will always gain more energy, in comparison to a particle that is accelerated in a time-varying field with the same electric field amplitude, regardless of RF phase ϕ choice. Thus, the total particle energy gain in the RF gap is decreased by a certain factor, that is called the *transit-time factor* T. In this case T can be expressed as follows:

$$T = \frac{\text{particle energy gain } (v = \beta c)}{\text{particle energy gain } (v \to \infty)} = \frac{\int_{-l/2}^{l/2} E_z(z)\cos\omega t(z) dz}{\int_{-l/2}^{l/2} E_z(z) dz}. \tag{2.5}$$

Taking into account the transit-time factor, and by defining the axial RF gap voltage V_0,

$$V_0 = q \int_{-l/2}^{l/2} E_z(z) dz, \tag{2.6}$$

expression (2.4) can be written as follows:

$$\Delta W = qV_0 T \cos\phi . \tag{2.7}$$

Analysing (2.7), for the RF phase $\phi = 0$, the particle is accelerated on the electric field crest and gains maximum possible energy gain. If $\phi < 0$ the particle arrives earlier than the field crest and later if $\phi > 0$. Therefore, for a stable acceleration in N+1 RF gaps (e.g *multi-cell RF cavity*) the particle motion must be synchronised with the electric field phase.

The Phase Stability Principle has been introduced by V. Veksler in 1944 [11] and independently by E. McMillian in 1945 [12], who constructed the first electron synchrotron. The principle will be explained qualitatively using an example that describes the acceleration of the non-relativistic electron beam in the periodic standing-wave RF structure.

First, consider an array of (N+1) identical RF gaps connected by beam tubes without fields inside of these tubes. Also assume that the length of these beam tubes is matched with the beam velocities that increase after each RF gap (e.g, Alvarez-type Drift Tube Linac [10]). Assume now that there is a particle (S) with a velocity that is perfectly synchronised with the electric field oscillation in these gaps, in a way such that it will enter each gap at the RF field *synchronous phase* ϕ_s (see Fig. 2.2). This particle is called a *synchronous particle* and the phase ϕ_s is the stable *operating RF phase*. A particle (L) that will arrive in the same gap later the synchronous particle will gain more energy, hence, in the following RF gap it will arrive earlier the synchronous particle. A particle (E) that arrives earlier the synchronous particle will gain less energy and will arrive later in the following gap. In that way, particles are oscillating near the synchronous particle within the stable phase range. A particle (U) that arrives at a phase earlier or later the synchronous particle $(\pi - \phi_s)$ is clearly unstable, since it will deviate further away from the synchronous phase $(\pi - \phi_s)$ in the following gaps. Thus, for a stable particle acceleration in the RF linac, the synchronous phase ϕ_s is chosen at the positive wave slope. The principle of off-crest acceleration is useful for the acceleration of an electron beam with non-relativistic velocities. While for the acceleration of a relativistic electron beam, on-crest acceleration is preferred.

The described phase stability principle is especially important due to the fact that during the acceleration, particles are gathered into separate bunches and then accelerated in the RF field. Depending on the accelerator specifications, a single bunch might be formed by a number of particles of 10^5 up to 10^{12}. In a single bunch there is only one synchronous particle with a synchronous phase ϕ_s. Hence, a single bunch is characterised by a particular *energy spread*. The *beam phase space*, in general, represents all particles in the distribution in the chosen two-dimensional coordinates. The particle energy is used as a longitudinal variable for the bunch longitudinal phase space. Typically, in order to analyse particle properties in the beam phase space, their parameters are calculated as a deviation from the ideal (synchronous) particle parameters.

Due to large amount of data, statistical methods are typically implemented to post-process the particle's distribution of the bunch in order to characterise its properties. In this work, the bunch dimensions are described by the rms values $(\sigma_x, \sigma_y, \sigma_z)$, as shown

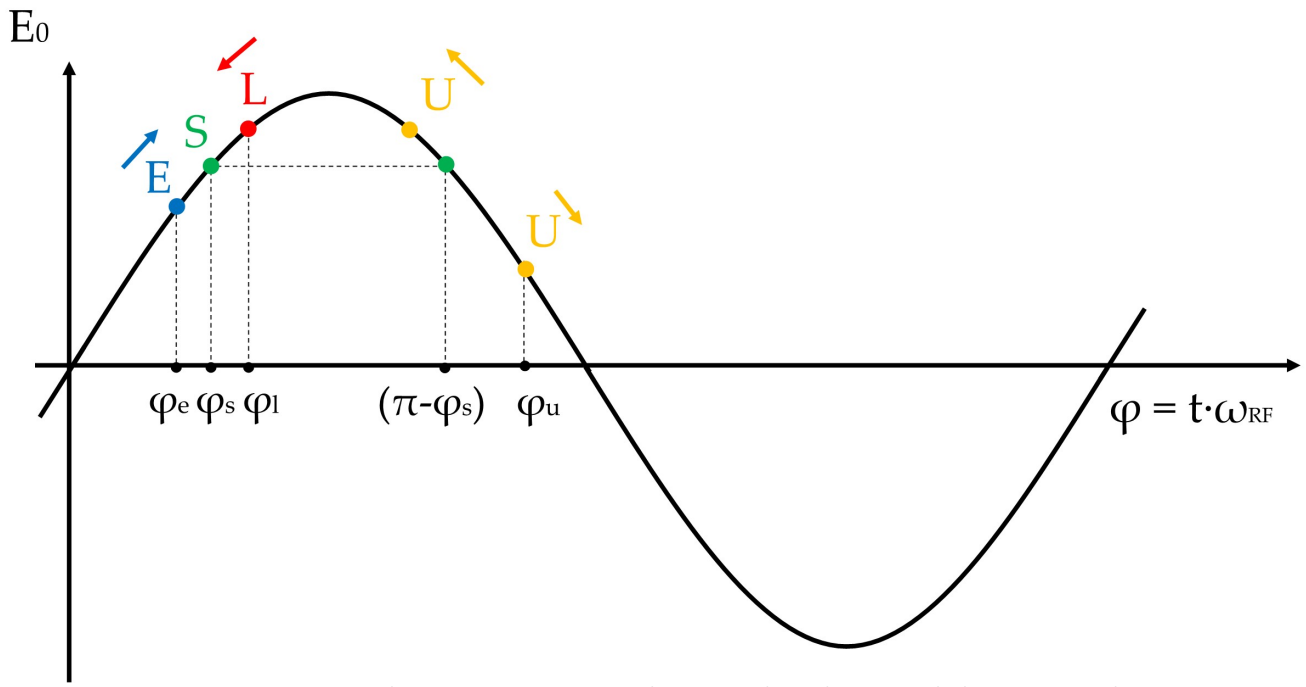

Figure 2.2: Qualitative picture explaining the phase stability principle.

schematically in Fig. 2.3 for the case of a Gaussian beam distribution. The beam *longitudinal phase space* can be represented as the beam *relative* longitudinal *energy spread* ($\Delta E/E$) as a function of time t, where ΔE [eV] is the beam rms energy spread and E [eV] is the beam average energy. In this case, the time $\Delta t = 0$ characterises the synchronous particle and the rest of particles are located within the range $\pm\Delta t$ and $\pm\Delta(\Delta E)$.

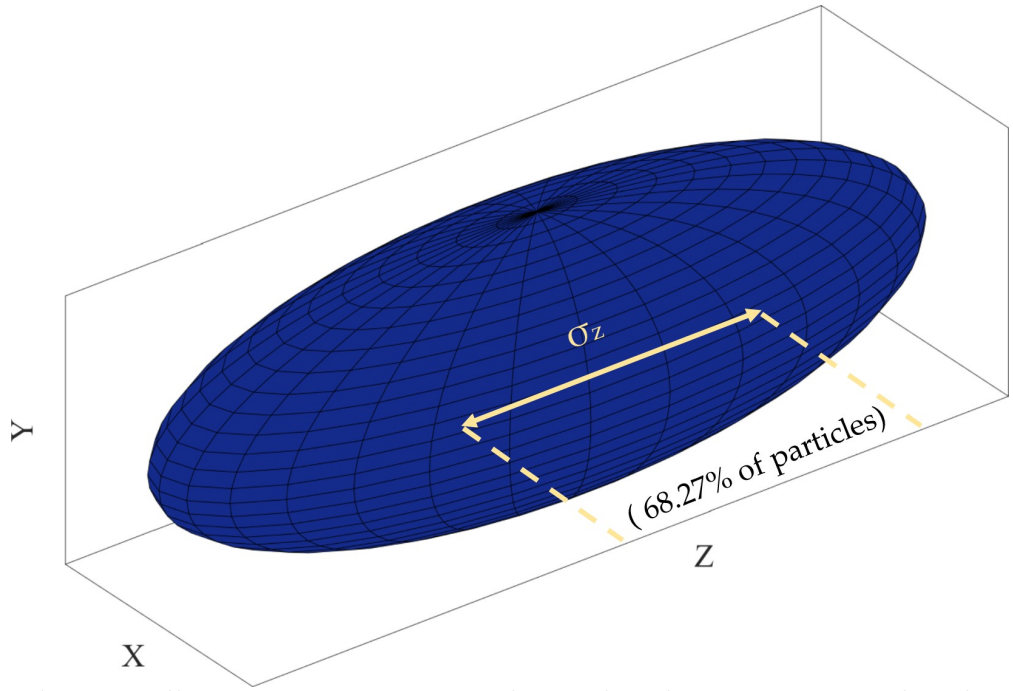

Figure 2.3: Schematic illustration of a Gaussian beam distribution in 3-D with indicated longitudinal rms bunch length σ_z.

2.2 RF Cavity Fundamentals

The goal of this section is to shortly discuss the important figures of merit that describe the accelerating RF cavity performance. In Section 2.2.1 analytic expressions that describe electromagnetic fields of a simple RF cavity are presented. Further on, by knowing the electromagnetic field distribution in the cavity, the key parameters of the cavity are introduced. For a well explained theory of electrodynamics, the reader is referred to [13]. The theory related to RF cavities for particle acceleration is discussed in detail in [10] and [14].

2.2.1 Electromagnetic Fields in the RF Cavity

The RF cavity, in general, is a volume surrounded by a metal conductor that supports the oscillation of time-harmonic electromagnetic fields with different resonance frequencies. The electric and the magnetic fields behaviour is governed by Maxwell's equations. In a space that is free of charges and currents, they can be expressed as follows:

$$\nabla \cdot \vec{B} = 0 \tag{2.8}$$

$$\nabla \times \vec{E} + \frac{\partial \vec{B}}{\partial t} = 0 \tag{2.9}$$

$$\nabla \cdot \vec{D} = 0 \tag{2.10}$$

$$\nabla \times \vec{H} - \frac{\partial \vec{D}}{\partial t} = 0, \tag{2.11}$$

where $\vec{E}$ and $\vec{H}$ is the electric and the magnetic field, respectively. The electric field displacement $\vec{D}$ and the magnetic induction $\vec{B}$, in case of fields considered in vacuum, are expressed as:

$$\vec{D} = \varepsilon_0 \vec{E} \tag{2.12}$$

$$\vec{B} = \mu_0 \vec{H}, \tag{2.13}$$

where ε_0 and μ_0 are constant values that represent the vacuum permittivity and vacuum permeability respectively ($c^2 \varepsilon_0 \mu_0 = 1$).

Assuming a harmonic dependence in time ($e^{-i\omega t}$) (2.8) - (2.11) can be reduced to[1]:

$$\nabla \times \vec{E} - i\omega \vec{B} = 0 \tag{2.14}$$

$$\nabla \times \vec{B} + i\omega \mu_0 \varepsilon_0 \vec{E} = 0. \tag{2.15}$$

Combining (2.14) and (2.15) together, the wave equations are obtained and written as:

[1] For the reminder, the electric field behaviour is considered in vacuum where $\varepsilon = \varepsilon_0$ and $\mu = \mu_0$

$$\nabla^2\vec{E} + \mu_0\varepsilon_0\omega^2\vec{E} = 0 \tag{2.16}$$
$$\nabla^2\vec{B} + \mu_0\varepsilon_0\omega^2\vec{B} = 0. \tag{2.17}$$

In cylindrical coordinates, the solution of wave equations are plane waves:

$$\vec{E}(\vec{r},t) = \vec{E}(\rho,\phi)e^{i(kz-\omega t)} \tag{2.18}$$
$$\vec{B}(\vec{r},t) = \vec{B}(\rho,\phi)e^{i(kz-\omega t)}, \tag{2.19}$$

where k is the wave number.

In Section 2.1 a simple standing wave RF gap has been considered for particle acceleration. The simplest RF gap can be represented by a cylindrical cavity with radius R and length L made of a perfect electric conductor with two openings and the beam tubes attached at the cavity end-plates that allow the particle beam to enter and leave the cavity. The described structure is referred to as a pillbox cavity and it is one of the simplest accelerating RF cavity shapes. A solution of the wave equations for such structure can be obtained analytically. For that, the beam openings are neglected and the following boundary conditions are implied:

$$\vec{n} \times \vec{E} = 0, \vec{n} \cdot \vec{H} = 0, \tag{2.20}$$

where $\vec{n}$ is a vector that is normal to the inside surface of the cavity.

The eigenmodes that are obtained by solving the wave equations for the pillbox cavity are classified in three wave types: TM (transverse magnetic) modes ($B_z = 0$) and TE (transverse electric) modes ($E_z = 0$). For the acceleration of charged particles it is obvious that the field configuration of a standing wave TM mode is the optimal choice. The standing wave TM mode exists in the pillbox cavity when the azimuthal and the radial electric field components vanish at z = 0 and z = L. This implies:

$$k_z L = p\pi, \text{ where } p \in \mathbb{Z}. \tag{2.21}$$

The field components of the standing wave TM modes in the pillbox cavity are written as follows:

$$E_z = E_0 J_m\left(j_{mn}\frac{\rho}{R}\right)\cos(m\phi)\cos\left(\frac{p\pi z}{L}\right)e^{i\omega t} \tag{2.22}$$

$$E_\rho = -E_0\frac{p\pi R}{j_{mn}L}J'_m(j_{mn}\frac{\rho}{R})\cos(m\phi)\sin\left(\frac{p\pi z}{L}\right)e^{i\omega t} \tag{2.23}$$

$$E_\phi = -E_0\frac{p\pi m R^2}{j_{mn}^2\rho L}J'_m\left(j_{mn}\frac{\rho}{R}\right)\sin(m\phi)\sin\left(\frac{p\pi z}{L}\right)e^{i\omega t} \tag{2.24}$$

$$B_z = 0 \tag{2.25}$$

$$B_\rho = E_0\frac{i\omega m R^2}{\sqrt{\mu_0/\varepsilon_0}j_{mn}^2\rho c^2}J'_m\left(j_{mn}\frac{\rho}{R}\right)\sin(m\phi)\cos\left(\frac{p\pi z}{L}\right)e^{i\omega t} \tag{2.26}$$

$$B_\phi = E_0\frac{i\omega R}{\sqrt{\mu_0/\varepsilon_0}j_{mn}c^2}J'_m\left(j_{mn}\frac{\rho}{R}\right)\cos(m\phi)\cos\left(\frac{p\pi z}{L}\right)e^{i\omega t}, \tag{2.27}$$

where J_m is the m-th Bessel function and J'_m its derivative, j_{mn}/j'_{mn} is the n-th root of J_m/J'_m. The electric field amplitude is given by E_0. The integer numbers m,n,p are used for the mode classification the following way: TE_{mnp} and TM_{mnp} modes. The number m indicates the number of the corresponding field anti-nodes in the pillbox cavity in azimuthal direction ϕ, number n stands for the number of field anti-nodes along radial direction ρ and p corresponds to the number of anti-nodes in the longitudinal direction z. The resonant frequency of the TM_{mnp} mode is defined by (2.28).

$$\frac{\omega_{mnp}}{c} = \sqrt{\left(\frac{j_{mn}}{R}\right)^2 + \left(\frac{p\pi}{L}\right)^2}. \tag{2.28}$$

In the case when $L/R < 2.03$, the pillbox cavity lowest resonance frequency corresponds to the TM_{010} mode which has only one field anti-node in z direction. The TM_{010} mode is one of the most common operating modes in RF cavities that is used for particle acceleration. Due to the lowest resonance frequency, the TM_{010} mode is sometimes referred as the cavity *fundamental mode*. In addition, the TM_{010} mode can be also referred to as the cavity *accelerating mode*. The electric and the magnetic field components of this mode are expressed as follows:

$$E_z = E_0 J_0\left(\frac{2.405\rho}{R}\right)e^{-i\omega t} \tag{2.29}$$

$$H_\phi = -i\frac{E_0}{Z_0}J_1\left(\frac{2.405\rho}{R}\right)e^{-i\omega t}, \tag{2.30}$$

where

$$Z_0 = \sqrt{\frac{\mu_0}{\varepsilon_0}} \approx 376.7\ [\Omega], \tag{2.31}$$

is the impedance of free space.

The electric and the magnetic field maps of the TM_{010} mode in the pillbox cavity with beam tubes being neglected are shown in Fig. 2.4.

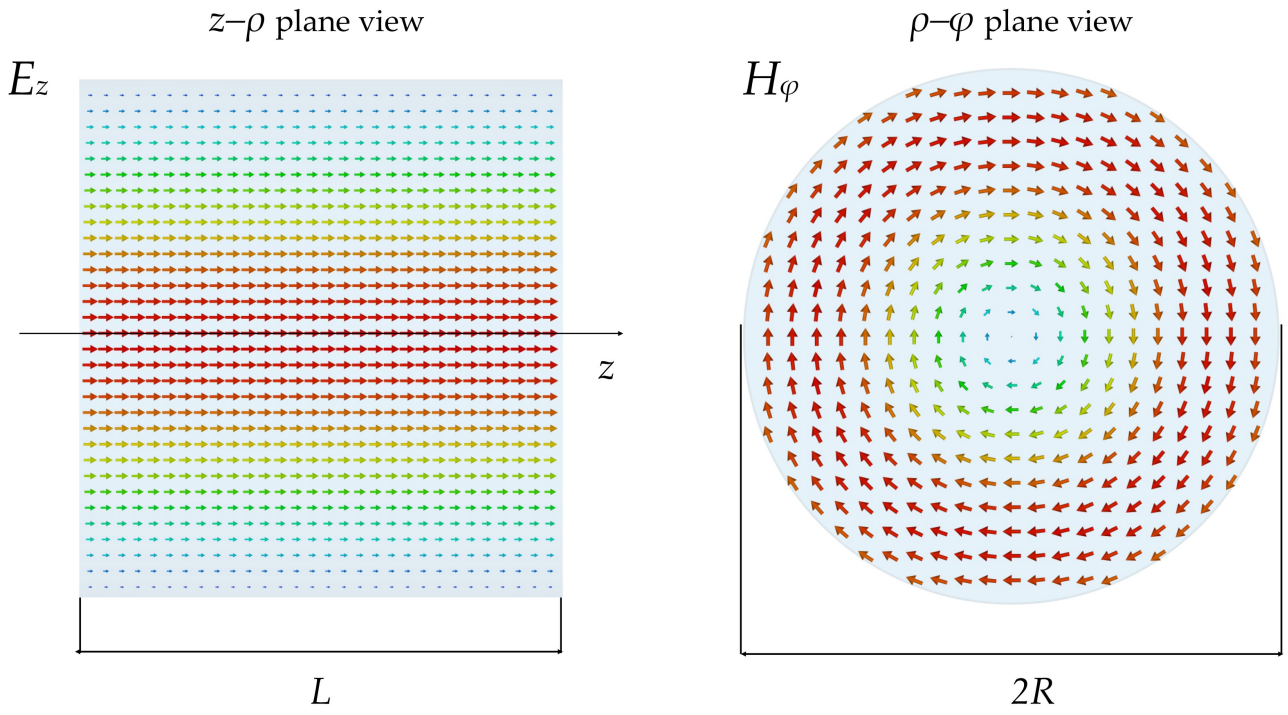

Figure 2.4: Illustration of the electric and the magnetic field distribution of the TM_{010} mode in the pillbox cavity.

2.2.2 RF Cavity Parameters

In the previous section the electromagnetic fields of the TM_{010} mode have been described analytically. Modern RF cavities have complex shapes. Due to that, for most of them, it is impossible to obtain an accurate analytic solution of the wave equations. In order to solve wave equations for RF cavities of complex shapes it is necessary to use electromagnetic field simulation software, such as e.g. CST MWS Studio® [15].

When evaluating the RF cavity parameters, in both, computations and experimental measurements, it is necessary to obtain the longitudinal electric field distribution on the cavity central axis in the first place, since most of the cavity parameters are defined by referring to the axial electric field profile $E_z(z)$. In order to explain some of the RF cavity parameters, the pillbox cavity is used as the reference cavity, due to its simple geometry.

The pillbox cavity accelerating TM_{010} mode *resonance frequency* is given by

$$\omega_{010} = \frac{2.405c}{R}. \tag{2.32}$$

It is easy to see that the resonance frequency only depends on the cavity radius R. In particle accelerators, the choice of the resonance frequency is typically motivated by the

bunch repetition rate, in order to provide the synchronisation between the RF field and the accelerated particles.

The importance of the cavity electric field profile along the accelerated beam trajectory z have been mentioned previously. One of the most important figures of merit is the cavity accelerating voltage. This parameter becomes even more important in case if one RF cavity consists of (N+1) coupled accelerating cells (RF gaps). In this case the cavity accelerating voltage will represent a sum of the accelerating voltages in each cavity cell characterising the full cavity acceleration performance. In case of the considered pillbox cavity with the beam trajectory that corresponds to the cavity central axis z, the cavity *accelerating voltage* is defined, by taking into account the finite particles velocity $\beta = v/c$, as

$$V_{\text{acc}} = \left| \int_{-L/2}^{L/2} E_z(z) e^{\frac{i\omega_0 z}{\beta c}} dz \right|, \tag{2.33}$$

where $\omega_0 = 2\pi f$ is the resonance frequency of the accelerating mode.

Due to the fact that the electric field amplitude at the central axis of the pillbox cavity is constant $E_z(z) = E_0 = \text{const}$, the analytic estimation of the accelerating voltage can be obtained for the pillbox cavity, with the beam tubes being neglected, as follows:

$$V_{\text{acc}} = \left| \int_{-L/2}^{L/2} E_z(z) e^{\frac{i\omega_0 z}{\beta c}} dz \right| = E_0 \left| \int_{-L/2}^{L/2} e^{\frac{i\omega_0 z}{\beta c}} dz \right| = L E_0 \frac{sin\left(\frac{\omega_0 L}{2\beta c}\right)}{\left(\frac{\omega_0 L}{2\beta c}\right)}. \tag{2.34}$$

For simplicity, the considered case of the pillbox cavity consists of only one accelerating cell. While in practice, these structures are typically formed by series of coupled accelerating cells. Hence, it is obvious that the cell length should be matched with the beam velocity and with the cavity resonance frequency. The so-called *synchronism condition* has been formulated by R. Wideroe [16]. For a multi-cell pillbox cavity and RF cavities that are designed in a similar way, which are operated with the $\text{TM}_{010};\pi$ mode, the length of the accelerating cells is chosen as follows:

$$L = \frac{\beta\lambda}{2}, \tag{2.35}$$

where λ is the wavelength. The value of β is typically chosen as the average relative velocity of the beam accelerated in the cavity. When characterising the cavity, the chosen value of β in (2.35) is sometimes referred as the cavity geometric beta or β_g.

The cavity average *accelerating gradient* is expressed as,

$$E_{\text{acc}} = \frac{V_{\text{acc}}}{L}, \tag{2.36}$$

here, worth noting, that with the presence of the beam tubes the *cavity effective length* L_{eff} should be specified as well along with accelerating gradient value.

Another important the cavity parameter is the *quality factor* Q_0 that is defined as

$$Q = \omega_0 \frac{\text{energy stored in the cavity}}{\text{power dissipated in the cavity walls}} = \omega_0 \frac{U}{P_\text{d}}. \tag{2.37}$$

At any given time instant, the time-averaged energy in the electric field equals the time-averaged energy stored in the magnetic field. The total energy stored in the cavity is written as

$$U = \frac{1}{2}\mu_0 \int_V \left|\vec{H}\right|^2 dV = \frac{1}{2}\varepsilon_0 \int_V \left|\vec{E}\right|^2 dV, \tag{2.38}$$

where V is the cavity volume. The power losses due to the cavity walls finite conductivity can be estimated as

$$P_\text{d} = \frac{1}{2} R_\text{s} \int_S \left|\vec{H}\right|^2 dS, \tag{2.39}$$

where R_s is the surface resistance of the cavity material.

The value of Q_0 also defines the resonance bandwidth of the cavity:

$$Q_0 = \frac{\omega_0}{\Delta\omega}, \tag{2.40}$$

where $\Delta\omega$ is the bandwidth of the resonance at the half-power value point.

In most of the practical cases the cavity material surface resistance becomes known after the cavity is manufactured. Due to that, the cavity parameters that describe the cavity performance depending on its geometry and independent of the RF losses are convenient during the RF cavity design stage. The cavity *geometry factor* is independent of the cavity size and material and only depends on the cavity shape, hence, it allows to compare the performance of different cavities. The cavity geometry factor is defined as

$$G = R_\text{s} Q_0. \tag{2.41}$$

One of the most critical cavity geometry dependent figure of merit is the *R-over-Q value*. This quantity is a measure of how efficiently the electric field of the cavity accelerating mode interacts with the beam i.e., how efficiently the beam is accelerated at a given amount of the cavity stored energy. The *R-over-Q value* is expressed as

$$\frac{R}{Q} = \frac{R_\text{sh}}{Q} = \frac{1}{2\pi f} \frac{V_\text{acc}^2}{U}, \tag{2.42}$$

where R_sh is the cavity effective *shunt impedance*. In this work, the following effective shunt impedance definition is used:

$$R_\text{sh} = \frac{V_\text{acc}^2}{P_\text{d}}. \tag{2.43}$$

The *R-over-Q value* only depends on the RF cavity shape (geometry) and independent of the RF losses. The higher the *R-over-Q value*, the more efficiently the RF cavity accelerates charged particles.

Multi-cell cavities are discussed in the following chapters and the additional figures of merit will be introduced in Chapter 4. In addition, some of the theoretical aspects related to the RF power transmission from the RF power generator to the RF cavity are discussed in Chapter 4, Section 4.4.

2.3 Normal Conducting and Superconducting RF Cavities

Normal conducting cavities are typically made of copper due to its high electric conductivity. Typical values for the quality factor of normal conducting RF cavities are in the range of $2 \cdot 10^4$. In addition, approximately 40 - 60 % of the RF power is dissipated in well prepared normal conducting cavity walls. The RF losses (2.39) in the normal conducting structure depend on the material surface resistance, written as

$$R_s = \frac{1}{\sigma \delta}, \tag{2.44}$$

where σ is the material electric conductivity and δ is the skin depth expressed as

$$\delta = \sqrt{\frac{2}{\omega \mu_0 \sigma}}. \tag{2.45}$$

The main advantage of normal conducting cavities is the possibility of operation in the pulsed regime with high accelerating gradients. On the other hand, taking into account high amounts of the dissipated power in the normal conducting cavity walls, the cavity can be operated at relatively low accelerating gradients (E_{acc} up to 1 MV/m) in continuous wave (CW) regime, in order to avoid overheating of the cavity walls. Hence, in CW regime, normal conducting linear accelerators must be designed with long enough longitudinal length in order to accelerate particles to high energies.

Integration of the superconductivity to modern high-energy accelerators allowed to provide a very efficient particle acceleration in the CW regime. Superconductivity, in general, is a term that is related to the phenomenon of zero electrical resistance[2] that has been found to occur in certain metals at particular conditions, that are characterised by critical transition temperature T_c, at which a metal becomes a superconductor. While superconductors are free of losses in case of the Direct Current (DC), the same does not apply in case of the Alternating Current (AC) regime, especially in case of RF cavities that are typically operated at the resonance frequency range of 300 MHz and higher. Superconducting radio-frequency (SRF) cavities are typically made of the type II superconductor niobium (Nb) due to its moderate value for the critical temperature T_c of 9.2 K. Presently, a well established technique that allows to cool down the cavity to an operating temperatures of 2 K and 4.2 K is available. The technique implies that the SRF cavity is

[2] In case of the direct current.

operated in a cryostat [14] that maintains the required operating temperature inside using liquid helium bath. The SRF cavity surface current behaviour in the superconducting state is described by the Bardeen–Cooper–Schrieffer (BCS) theory [17].

Moreover, the cavity made of niobium has an additional temperature-independent surface resistance that is referred as residual resistance R_0 that originates from contamination of niobium by another material causing trapped magnetic vortices [18].

As a result, the total surface resistance of the SRF cavity can be written as follows,

$$R_s|_{sc} = R_{BCS}(f, T) + R_0, \tag{2.46}$$

where R_{BCS} is the temperature and frequency dependent BCS surface resistance.

Therefore, SRF cavities are not fully free of RF losses. However, the typical R_s values for SRF cavities made of Nb are in the range of 10 nΩ up to 100 nΩ [19]. The very low surface resistance allows to operate a well prepared SRF cavity with a very low amount of RF power dissipated in the cavity walls and, as a consequence, with very high quality factors of 10^9 up to 10^{11}, while obtaining the accelerating gradient of up to 50 MV/m. Hence, the implementation of SRF cavities for the operation in CW or long-pulsed regime has an obvious advantage in comparison to the normal conducting RF cavities.

It is obvious that the increase of the accelerating gradient E_{acc} in SRF cavities, allows to significantly reduce the accelerator investment and operational costs. Over the past 40 years the accelerating gradients of SRF cavities have been successfully increased from 5 MV/m up to 55 MV/m. This was done by overcoming parasitic cavity phenomena such as multipacting and field emission, which typically arise at specific ranges of E_{acc} values, that are proportional to cavity peak magnetic and electric field at its inside surface. This was done by optimising SRF cavity shapes and by introducing special surface treatments to the SRF cavity inside surface. As mentioned previously, up to date, most SRF cavities that are currently in operation, are made of Nb, which is characterised by the empirical surface magnetic field limit of 210 mT (at $T_c = 9.2$ K), at which the SRF cavity is affected by the thermal breakdown and leaves the superconducting state. It is worth noting that besides the empirical magnetic field limit, local thermal instabilities can occur due to very small defects of the cavity inner surface. In case when the cryogenic load arising from the cavity overheated local spots, exceeds the designed cryogenic limits, the SRF cavity can loose the superconducting state at the peak magnetic fields lower then the designed limit.

Presently, in order to overcome the problem of the empirical magnetic field limitation, other superconducting materials (e.g. Nb alloys) are investigated for SRF cavity fabrication. Some of the suggested materials are characterised by higher limits of the peak surface magnetic field and, as a consequence, higher accelerating gradients can be achieved in comparison to SRF cavities that are made of Nb. The problem of achieving very high accelerating gradients of SRF cavities is beyond the framework of this work. Hence, for more details regarding the ultimate accelerating gradient limitations it is suggested to consider the following sources for more details [20], [21], [22].

3 Upgrade of the Capture Section of the S-DALINAC Injector

A two-cell cavity that is part of the capture section of the S-DALINAC is permanently out of operation due to technical reasons. The two-cell cavity was installed in order to pre-accelerate low energy electron beams such that the mismatch in phase in the following 5-cell cavity is minimised. The length of the accelerating cells of the 5-cell cavity is determined by the value of β_g of 1, while the beam velocity correspond to the value of β of 0.7. Due to that, the largest longitudinal energy spread growth of the beam at the S-DALINAC is originating from the capture section. Moreover, the beam energy spread that originates from the injector linac can not be corrected in the non-isochronous recirculation regime in the main linac [23]. Therefore, a replacement of the capture section by a new RF system is necessary in order to minimise the beam longitudinal energy spread at the S-DALINAC.

In this chapter the performance of the current setup of the capture section is examined. The necessary criteria for the new accelerating cavity will be introduced based on the existing limitations. Further on, an optimal cavity type is evaluated using the qualitative and quantitative approach.

3.1 Current Setup of the Capture Section

The injector of the S-DALINAC consists of the capture section and the main injector linac (see Fig. 3.1). The aim of the capture section is to provide the first energy to the electron beam so that it enters the main injector linac with almost the speed of light c. In the main injector linac the beam is accelerated in two 20-cell β_g=1 SRF cavities to energies up to 10 MeV.

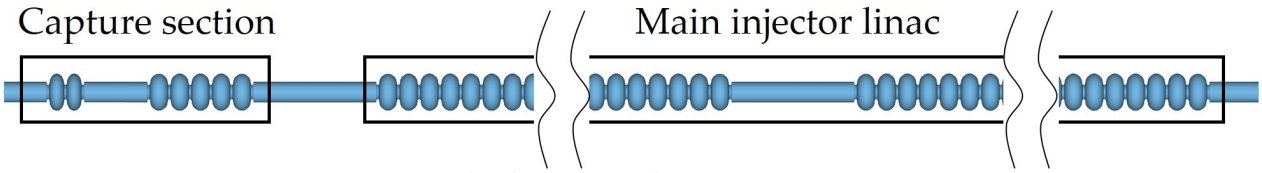

Figure 3.1: The layout of the S-DALINAC injector.

Presently, the capture section consists of a 5-cell β_g= 1 SRF cavity (see Fig. 3.2 and Fig. 3.3) and a 2-cell β_g= 0.85 cavity, implemented to pre-accelerate the beam in addition to the 5-cell cavity. Both of them are hosted in the same cryostat (see Fig. 3.4). The 2-cell cavity is no longer in operation due to a technical problem with an RF power input-coupler. The modification of the coupler would require a new cryostat. This leads to the fact that the beam with an energy of 200 keV is directly delivered to the 5-cell cavity.

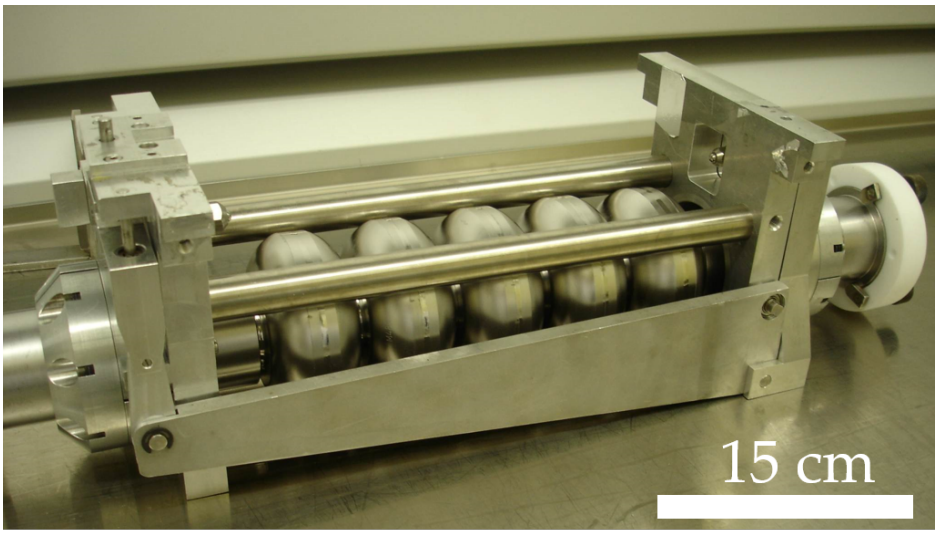

Figure 3.2: Photograph of the 5-cell $\beta_g=1$ cavity in the tuner frame.

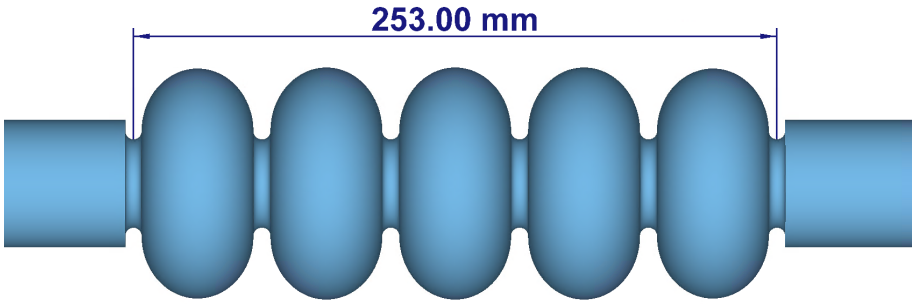

Figure 3.3: 3-D CAD model of the 5-cell $\beta_g=1$ cavity.

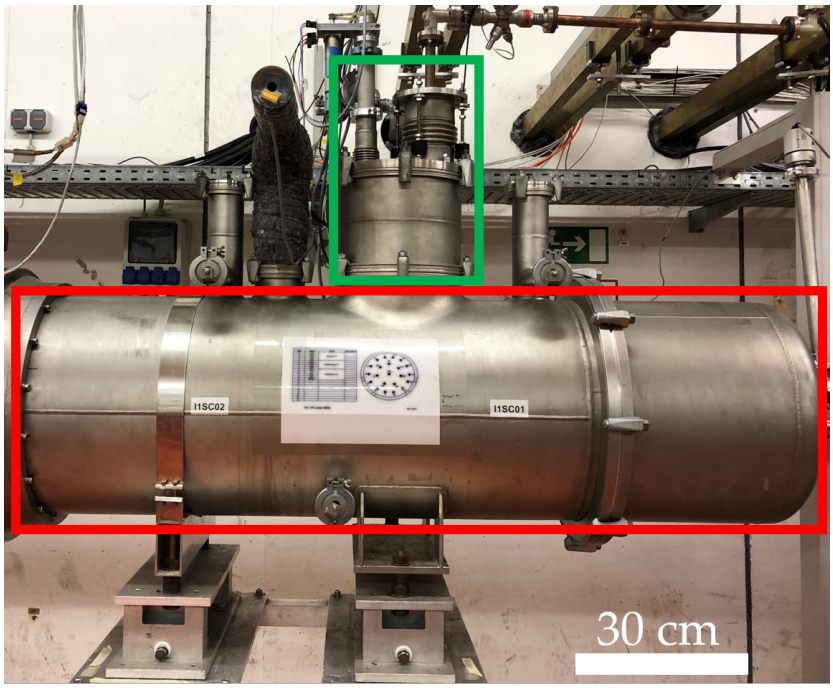

Figure 3.4: Photograph of the crystoat (red) that hosts the 5-cell $\beta_g=1$ cavity and the 2-cell $\beta_g=0.85$ cavity together with the RF power input-coupler for the 5-cell cavity (green).

The acceleration of an electron beam with an energy of 200 keV ($\beta = 0.7$) was studied for the 5-cell cavity by particle tracking simulation. Figure 3.5 shows the results of a computation which includes the energy gain and relative energy spread growth of the beam. The energy spread growth is estimated by using (3.1).

$$\delta_E(z) = \frac{\Delta E_{\text{out}}(z)}{E_{\text{out}}(z)} - \frac{\Delta E_{\text{in}}}{E_{\text{in}}} \tag{3.1}$$

In the simulated model the value of the peak electric field at the axis of the cavity is equal to 10 MV/m. The results were obtained for the initial RF phase ϕ_{RF_0} of the accelerating mode at which the maximum possible energy gain of the beam is given. The key input parameters of the cavity that were used in this computation are collected in Table 3.1.

Analysing the results one can see that the 5-cell cavity fails to provide the necessary energy gain of 1 MeV. Only in the second cell ($0.12\ \text{m} \leq z \leq 0.17\ \text{m}$) a stable beam acceleration is observed. In the rest of the cells the beam experiences not only an accelerating but also a decelerating electric field. This is caused by the absence of synchronisation between the RF EM field and the beam. The length of the accelerating cells does not match to the velocity of the beam. When the RF phase changes, the electric field points in the opposite direction which leads to a loss of energy of the beam (e.g. regions around $z = 0.1$ m, $z = 0.35$ m). The relative energy spread of the beam increases because of the mismatch in phase. This means that the current setup of the capture section fails to provide the necessary beam parameters, which disables the operation of the Spin Polarised electron Gun (SPG) at the S-DALINAC.

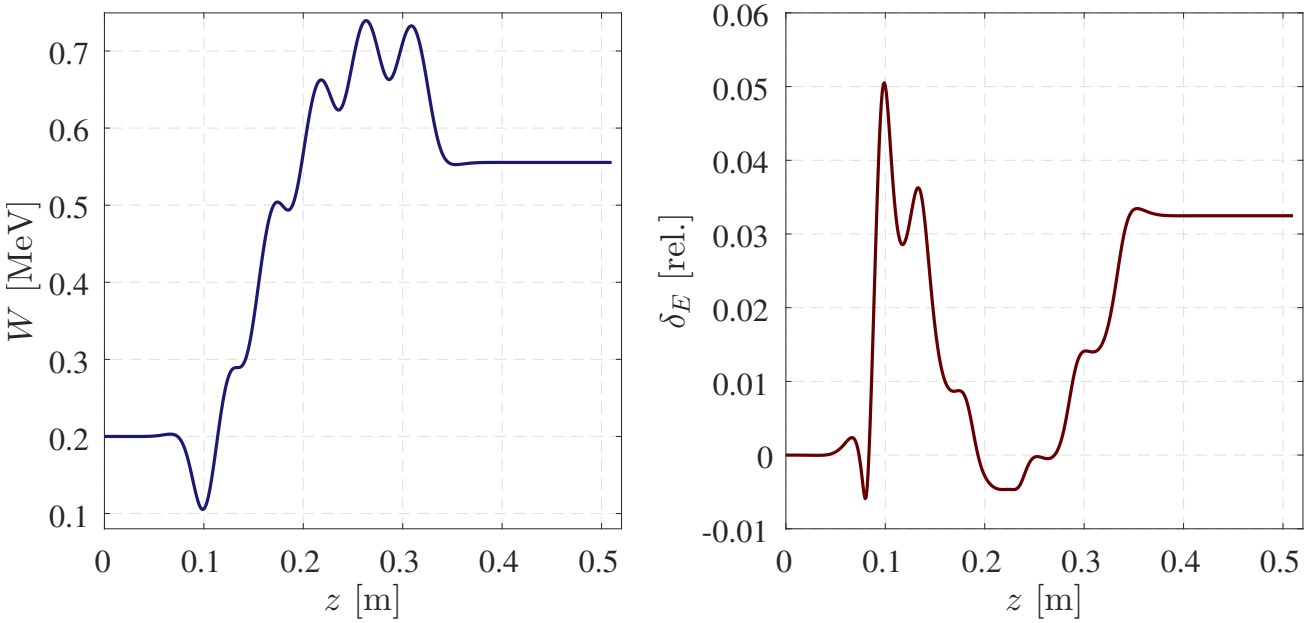

Figure 3.5: Illustration of the results of the particle tracking simulation for the 5-cell $\beta_g = 1$ cavity. The average kinetic energy E of the beam is shown at the left and the energy spread growth δ_E is shown at the right.

Parameter	Value
Accelerating mode	TM_{010}
Phase advance θ, rad	π
Resonant frequency f, GHz	3
Geometric beta β_g	1
Peak electric field on axis E_0, MV/m	10
Field flatness η, %	1.8

Table 3.1: The parameters of the 5-cell $\beta=1$ cavity that were used in the particle tracking simulation.

Besides the inability to use the SPG as a beam source and carrying out the corresponding experiments at the S-DALINAC one should consider the factor of age of the 5-cell cavity. The S-DALINAC has been operated since 1991. With time the quality of the inside surface of the 5-cell cavity went down. Often it is affected by quench which limits the operation of the accelerator. Recently it was reported that the structure is affected by a plastic deformation at the connection of the beam tubes to the end-cells.

Thus, to provide stable operation of the S-DALINAC in standard and ERL modes along with allowing the use of the spin polarized gun (SPG) as electron source, it is necessary to develop a new accelerating structure to replace the 5-cell cavity. The new accelerating cavity should match the necessary requirements that are discussed in the next section.

3.2 Requirements for the New Cavity

The requirements for the upgrade are ruled by the operating parameters of the S-DALINAC, the existing limitations and the investments costs. The following criteria were defined for the new RF cavity:

1. **Operating frequency.** The resonance frequency of the TM_{010} mode of the cavity is chosen to be the S-DALINAC operation frequency $f=3$ GHz.

2. **Energy acceptance.** The energy acceptance of the cavity must cover the range from 200 keV up to 250 keV.

3. **Amplitude of the accelerating field.** The peak amplitude of the electric field on the axis of the accelerating mode should be kept below or equal to 10 MV/m. This value corresponds to the values that are used in operation for the current setup such that the RF losses do not exceed the limits of the cooling capacity of the cryostat.

4. **Superconducting RF cavity.** Spatial restrictions at the S-DALINAC suggest the use of superconducting RF technology. For the new capture cavity, 270 mm of longitudinal space is available. The use of a normal conducting RF cavity is impossible for our needs due to the accelerating gradient limits in the CW regime. Typical values of the accelerating gradient of a normal conducting accelerating cavities usually do not exceed 1 MV/m in the CW regime.

5. **Total costs.** The total costs of the modifications involved in the upgrade should be minimised.

6. **Compatibility**. The new cavity must fit into the present cryostat and should be compatible with the present RF power input-coupler. Compatibility with the present RF power coupler means the coverage of the necessary tuning range of the coupling coefficient between the cavity and the RF power generator.

7. **Beam characteristics.** The relative rms energy spread of the accelerated beams must be kept as low as possible. The output energy of the beam should be at least 1 MeV.

8. **Mechanical stability.** The new cavity must be mechanically stable in operation at 2 K. In case if the longitudinal stiffness of the cavity can be improved by modifying the geometry of the structure this will have a priority over better electromagnetic (EM) parameters of the accelerating mode.

The last four requirements are contradictory. Prioritisation of achieving the best beam quality leads to increased costs. In the end a balanced solution is preferred. The highest priority during the selection and optimisation procedure is dedicated to the total costs and mechanical stability.

3.3 Choice of an SRF Cavity Type

The choice of a cavity type depends on the beam velocity and the resonant frequency of the accelerating mode. Low and medium-βcavities are typically implemented in heavy-ion accelerators whereas the high-beta elliptic cavities are applied for electron acceleration. The existing SRF cavity types can be classified in three major groups depending on the velocity of the accelerated particles:

- Low beta cavities ($\beta<0.6$): quarter-wave, half-wave and spoke cavities
- Medium beta cavities($0.6<\beta<0.9$): spoke and elliptic cavities
- High beta cavities ($\beta > 0.9$): elliptic cavities

Quarter-wave, half-wave and spoke cavities are based on a TEM mode while elliptic structures are operated with a TM mode [14].

In the medium-β range spoke and elliptic cavities are available. However the transverse dimension of a spoke cavity is 0.5λ compared to 0.9λ for an elliptic cavity. At the frequency of 3 GHz the wavelength of the accelerating mode corresponds to $\lambda=10$ cm. Therefore, a practical realisation of a spoke cavity becomes impossible because of the small transverse size. Thus, at this frequency an elliptic cavity type is preferred.

3.4 Considered Layouts for the Upgrade

Various configurations of an elliptic cavity differ by the number of cells and their length. This section discusses the results of an investigation of three suggested layouts. A 3-D CAD model of each layout was constructed and allows not only to calculate the electromagnetic field of the accelerating mode but also to evaluate the tunability of the field flatness.

After introducing general information about each of the suggested cavities their efficiency is compared. The output energy of the beam is the reference value in this comparison while the electric field amplitude on the central axis is kept equal. It should be noted that the initial estimations were carried out for an input energy of the beam of 100 keV (β=0.55). Further on, it was confirmed that the injection energy will go up to 200 keV after the planned upgrade of the gun. An increase of the energy affects the final choice of the number of accelerating cells and their length. However this does not impact general decisions such as: the cavity type selection or the configuration of the particular cavity type that will be discussed further on.

The design process of an SRF reduced-β cavity is shown in details in chapters 4, 5 and 6. This section only contains the outcome of the calculations. Nevertheless, it is necessary to point out that each considered cavity is operated at the TM_{010} mode with a resonance frequency of 3 GHz, a phase advance of π and a field flatness tuned below 10 %.

Two Independently Driven Cells

At the beginning it is necessary to point out that a configuration with two independently driven cells is not compatible with the present cryostat of the capture section of the S-DALINAC. Hence, it fails to satisfy the necessary requirements for the upgrade. In addition due to the cavities short effective length, the implementation of this scheme at S-DALINAC requires an accelerating gradient of 15 MV/m. However, in absence of the total costs requirement this layout can be efficiently used to accelerate low-β electron beams.

One of the possible realisations of this concept is shown in Fig. 3.6. It consists of two identical 3 GHz β_g=0.7 cells. In this setup each cell acts as a cavity and is operated completely independently from the other. The phase of the EM field can be tuned individually in each cavity thanks to the separate RF power sources. This allows to achieve synchronisation between the beam and the EM field of the accelerating mode for a wide range of operating parameters. In addition, a single cell cavity avoids the problem of the field flatness which is especially relevant for multi-cell cavities.

Thus, the main advantage of this layout is the flexibility to changes of the input energy of the beam and the peak amplitude of the electric field on axis of the cavity. For instance, at the KEK ERL particle accelerator the injector consists of three two-cell independently driven SRF cavities [24]. Another example of a successful practical implementation was reported in [25] where five 2-cell cavities have been installed at the Cornell ERL injector.

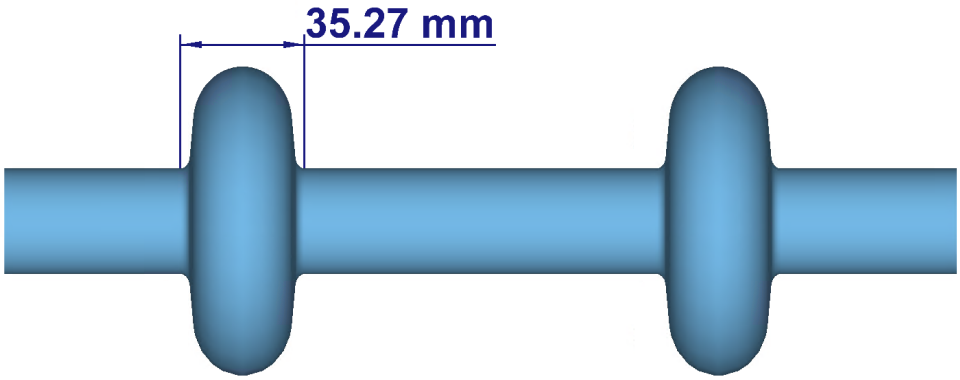

Figure 3.6: 3-D model of two identical independently driven β_g=0.7 cells with indicated length of the cells.

β-graded Cavity

During the acceleration, the velocity of electrons increases significantly faster compared to protons for the same amount of energy gain. In that regard, in electron linacs normal conducting β-graded cavities are widely used to accelerate low energy beams [26]. The main idea of these cavities is that the length of each subsequent gap (cell) increases with the increase of the kinetic energy and the velocity of the beam respectively. This approach guarantees a stable and predictable acceleration of the beam without a significant energy spread growth if all the necessary conditions for operation are satisfied.

Normal conducting β-graded cavities are the state-of-the-art technology. However, this principle has never been applied for a single multi-cell SRF cavity. A prototype of a 5-cell β-graded SRF cavity was designed and considered as one of the options for the upgrade. A 3D model of the cavity is shown in Fig. 3.7. The normalised electric field distribution on the central axis of the cavity with indication of the β_g for each cell is shown in Fig. 3.8.

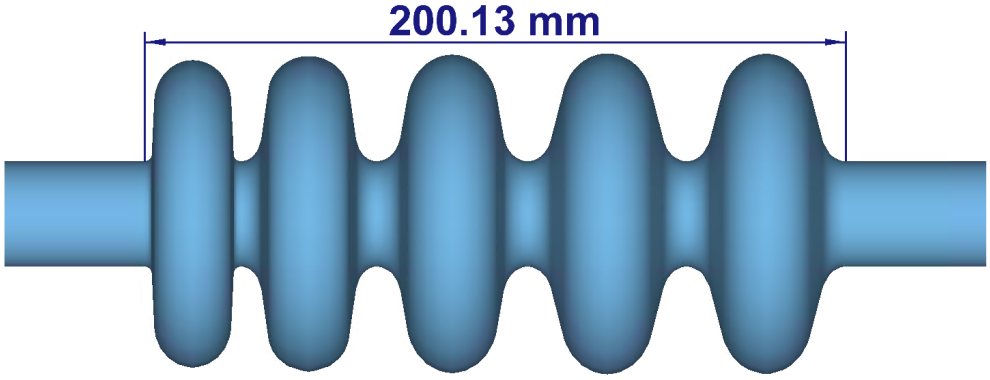

Figure 3.7: 3-D model of the 5-cell β-graded cavity with indicated effective length.

The geometry of the considered β-graded cavity is not fully optimised. The length of the last two cells is chosen to be the same to reduce the time needed for the field flatness optimisation. A field flatness of $\eta = 9.68\%$ was obtained using a genetic optimisation algorithm [27]. This value can be improved further on if necessary but it is sufficient for the needs of this initial performance study. The effect of change of the electric field

distribution due to the attachment of the beam pipes to the first and the last cell requires an additional study to estimate optimal values of β_g for these cells.

The optimal length L_n of the n-th cell can be estimated as follows:

$$L_n = \sqrt{1 - \frac{1}{\left(\frac{E_n}{mc^2} + 1\right)^2}} \cdot \frac{\lambda}{2}, \tag{3.2}$$

where E_n is the average kinetic energy of the electron beam at the entrance of the n-th cell, m is the rest mass of the electron and λ is the wavelength of the TM_{010} mode.

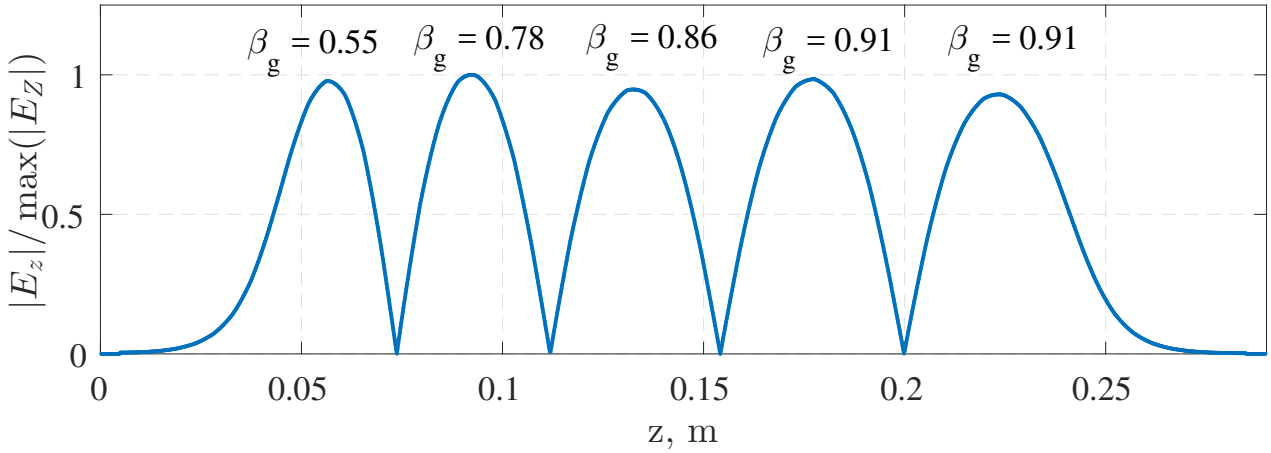

Figure 3.8: Normalised absolute electric field distribution of the TM_{010} mode on the central axis of the 5-cell β-graded cavity with indicated β_g of each cell.

A β-graded SRF cavity reaches maximal efficiency when the lengths of the cells corresponds to the local velocities of the beam. This implies that the following requirements needed to be satisfied:

1. The maximal amplitude of the accelerating field on the central axis of the cavity must be constant. Its value should be selected in advance. This value determines the length of all cells except for the first one.
2. The electric field distribution of the accelerating mode should be uniform as quantified by a value of the field flatness of η <10%.
3. The input energy of the beam is fixed.

Any deviation from one of these requirements will adversely affect the quality of the accelerated beam.

The standard technique to adjust the field flatness at the design stage of the cavity is to modify the geometry of the half-end-cells (more details are given in Chapter 4). For a typical multi-cell SRF elliptic cavity only four geometric parameters are optimised in order to obtain the necessary field flatness in most of the cases, whereas for the β-graded cavity the diameters of all cells had to be optimised as well. This led to a problem with thirteen unknown parameters and one goal value and made field flatness tuning much more complicated and time-consuming.

Reduced-β Cavity

Multi-cell SRF reduced-β cavities are typically implemented in heavy-ion particle accelerators [28]. The reduced-β denotation originates from the fact that the geometric β_g is less than one. Until now, such structures have not been applied for the acceleration of low energy electron beams. The possibility of using such cavity type is not straight forward since the synchronism condition between the RF field and the beam is not satisfied in each of the cells.

In order to validate the possibility of use of this cavity type, a prototype of a 5-cell reduced β_g=0.7 cavity was designed (see Fig. 3.9) and studied. The results of the computations are presented in the next section where the performance of the reduced-β cavity is compared to the one of the β-graded cavity.

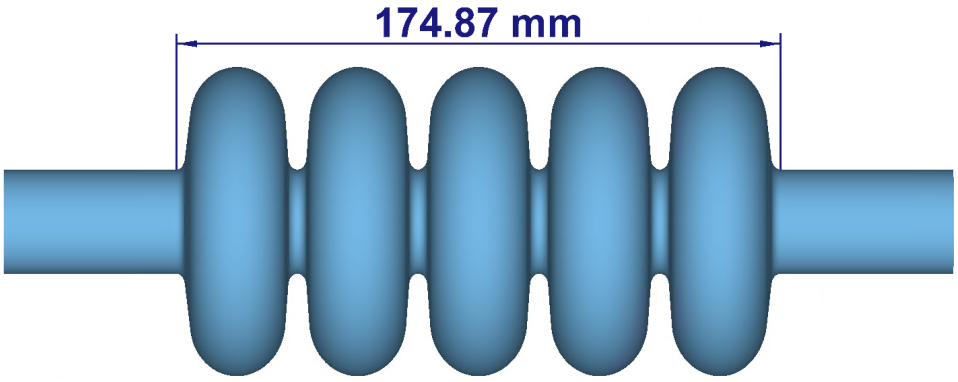

Figure 3.9: 3-D model of the 5-cell reduced-β cavity with indicated effective length.

3.5 Efficiency Comparison and Conclusion

The most efficient layout for the upgrade of the capture section of the S-DALINAC injector is the combination of two independently phased single-cell cavities. Its main advantage is the possibility of adjusting the RF phase in each cavity separately to compensate for changes of the beam parameters such as the input energy and bunch length to achieve the necessary characteristics of the beam after acceleration. However, this layout is the most expensive among the suggested possibilities. The main source of increased costs is the need for a new cryostat for the new cavity.

The principle of a β-graded cavity is well known and has been used in normal conducting accelerating structures since the beginning of the use of the RF acceleration principle. Implementing this idea for a multi-cell SRF elliptic cavity is feasible as shown by simulations. However, the main concerns are related to the practical realisation. Major difficulties during the tuning of the field flatness were encountered at the design stage of the prototype. The possibility of achieving and maintaining the necessary value of the field flatness in operation is challenging. Even though an acceptable field flatness value was obtained in the simulations, the geometry of each cell should be optimised further to avoid high electric and magnetic field amplitudes on the inner surface of the cavity

walls. Therefore, the existing models should be used to optimise the characteristics of the cavity further.

To motivate the choice between the β-graded and the reduced-β cavity their performances for the 100 keV beam have been studied. Figure 3.10 illustrates the output energy of the beam depending on the peak value of the electric field on axis. To maximise the accelerating gradient the RF phase ϕ_0 in each considered case was chosen in such a way that the beam gains the maximal possible energy.

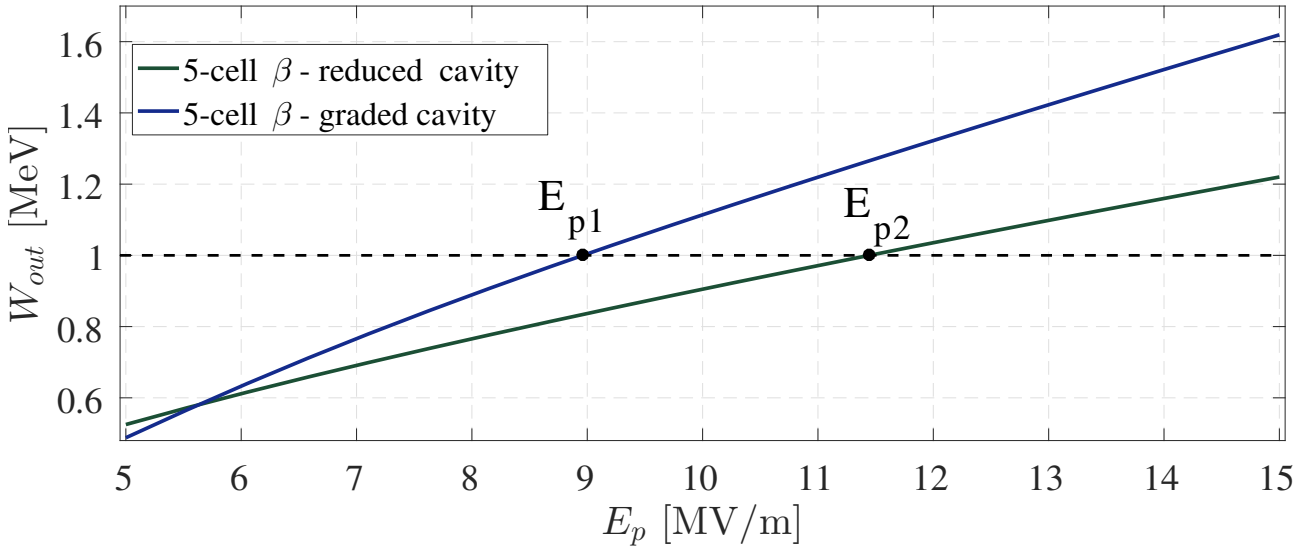

Figure 3.10: Illustration of the output energy of the beam depending on the peak electric field amplitudes on axis for the 5-cell reduced-β cavity and the 5-cell β-graded cavity.

For the β-graded cavity the value E_{p1} = 8.96 MV/m corresponds to an output energy of the beam of 1 MeV, whereas for the reduced-β cavity the value E_{p2} = 11.45 MV/m is higher by 2.49 MV/m. The necessary value of E_p for the reduced-β cavity can be lowered by optimising the number of cells and their length.

The main advantage of the reduced-β cavity over the β-graded cavity is its simple geometry while the difference in the acceleration performance for the specified requirements is not significant. The fact that the geometry of the mid-cells in the reduced-β cavity is identical means that standard tuning techniques can be applied. Further computations for the reduced-β cavity have shown that besides the necessary energy gain it is also capable of providing a reduction of the relative energy spread of the beam. From preliminary calculations the main disadvantage of the reduced-β cavity is the limited range of E_p values at which the necessary characteristics of the beam can be obtained.

Taking into account the standard manufacturing process of elliptic SRF cavities [29], the production costs of the β-graded cavity would be considerably higher compared to the reduced-β cavity which is built from identical cells. In that regard, and with respect to the potential difficulties in operation of the β-graded cavity, it was decided to proceed with the development of a multi-cell reduced-β cavity as a replacement of the current 5-cell β_g= 1 cavity.

It is worth nothing that the reduced-β cavity implementation is feasible for acceleration of electron beams with low energy and low charge, which is the case of the S-DALINAC where a single electron bunch charge is 4 pC and lower. For the acceleration of the low

energy beam with high charge in the multi-cell reduced-β cavity it is necessary to carry out beam dynamics studies while taking into account the space-charge effect.

4 RF Design of the Reduced-beta Cavity

This chapter discusses the RF design aspects of a 3 GHz reduced-β SRF cavity. First, a suitable cell shape, an optimal number of cells and a value for β_g of the cavity is evaluated, such that the requirements prescribed by the S-DALINAC are fulfilled. Further on, the RF parameters of a 6-cell $\beta_g = 0.86$ cavity operated with the $TM_{010};\pi$ mode are investigated. In order to ensure that the peak fields in the 6-cell cavity do not exceed the recommended values in operation, the peak EM field amplitudes at the inner surface of the cavity are estimated and their values are compared to experimental data available in literature.

The 6-cell cavity is planned to be equipped with the existing RF input power coupler that is available at the S-DALINAC facility. In that regard, the electromagnetic compatibility between the RF input power coupler and the 6-cell cavity is justified quantitatively. The required RF input power level for a cavity operation is analytically estimated while taking into account a proboble resonance frequency detuning. Finally, a conclusion regarding the overall RF performance of the developed 6-cell cavity is presented.

It is orth noting that a problem of higher order modes (HOM) is not encountered in the 6-cell RF design. This is explained by the fact that the S-DALINAC was initially designed for operation with a low beam current. Due to that, HOM damping systems were not considered during the RF design of the accelerating cavities of the S-DALINAC. In addition, trapped HOMs are present in 20-cell SRF cavities. These modes can not be extracted from 20-cell cavities due to the large number of cells. According to that, the beam current in the accelerator is limited to a particular level. Hence, the development of a HOM damping system for the 6-cell cavity is irrelevant when not at first HOM damping in the main linac is considered.

4.1 Shape of the Accelerating Cells

The geometric shape of an SRF cavity determine its RF parameters such as: the resonance frequency of the accelerating mode, the field flatness, the *R-over-Q value*, the peak electric fields at the inner surface of the cavity and the power dissipated in the cavity walls. Since the first use of SRF technology for particle acceleration, a number of basic accelerating cavity shapes were introduced. One of the first well optimised cell shapes is the TESLA cavity shape, that was developed by the TESLA collaboration and presented in 1992 [30]. The shape was designed with the intend to reduce the E_p/E_{acc} ratio and to minimise risks of encountering field emission in operation, which at the time was one of the main factors that limited the accelerating gradients of SRF structures.

Up to date, no fundamental limitation for the peak electric field on the surface was encountered [14]. The possibility of operation at accelerating gradients of 140 MV/m and 220 MV/m in CW and pulsed regimes, respectively, was demonstrated experimentally for test cavities made of Nb. Whereas an empirical critical peak magnetic field on the

surface exists and limits the ultimate accelerating gradients in SRF cavities. In order to overcome the problem of the magnetic field limitation and to reach higher accelerating gradients, re-entrant and low-loss (LL) cavity shapes have been developed in Cornell [31] and Jefferson Laboratory [32], respectively, with minimised B_p/E_{acc} ratio in comparison to the TESLA cavity shape. A pay-off for this advantage is an increased value of the E_p/E_{acc} ratio. The differences between the cavity shapes mentioned above are illustrated in Fig. 4.1.

It is worth noting that besides a cavity geometry optimisation, there are undergoing investigations of various cavity surface preparation techniques, Nb treatments and alternative superconducting alloys with the intend to alleviate the possible accelerating gradient in SRF cavities.

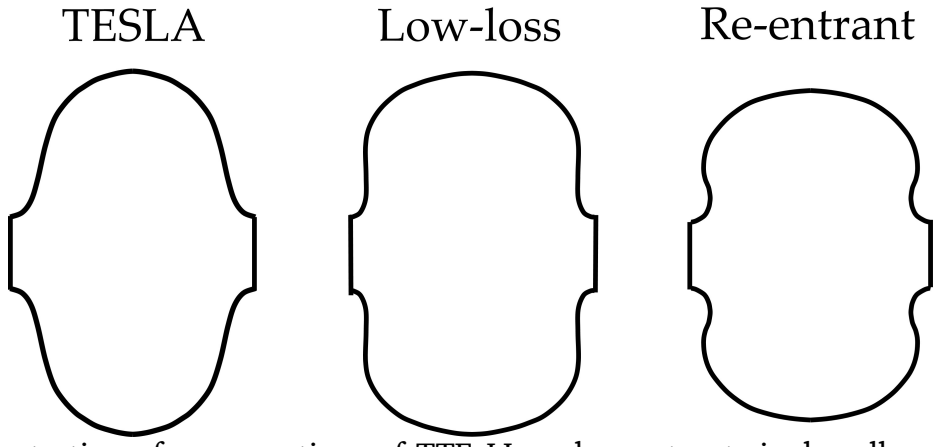

Figure 4.1: Illustration of cross sections of TTF, LL and re-entrant single cell cavities operated with the TM_{010} mode at the same resonance frequency.

The choice of a basic cell shape for the new cavity is motivated by the previously described requirements for the upgrade of the capture section. First of all, a high accelerating gradient is not a priority for the new cavity. In that regard, the re-entrant or LL cavity shape is not the optimal choice, since their main advantage over the TESLA cavity shape is an increased accelerating gradient. SRF cavities based on the TESLA shape were successfully implemented and commissioned for the European XFEL accelerator, where 816 cavities were manufactured and the vast majority of them have reached the designed accelerating gradient [33]. The RF parameters of TESLA cavities have demonstrated a lower sensitivity to external mechanical loads in comparison to LL and re-entrant cavities. Furthermore, the use of a well established technology allows to minimise the cavity production costs.

Taking into account the large experience in production and well-known inside surface preparation, the TESLA shape was chosen as reference shape for the reduced-β cavity design. The required accelerating gradient for the capture section is below 5 MV/m and can be achieved at a considerably lower peak magnetic field in comparison with the fundamental magnetic field limit that is typically encountered in operation at very high accelerating gradients.

A standard multi-cell TESLA cavity is operated at the TM_{010} mode with a phase shift θ of π and a resonance frequency of 1.3 GHz. A geometry optimisation of a 1.3 GHz TESLA

cavity for the optimal RF parameters was demonstrated in [34]. The resonant frequency of the fundamental mode depends on the size and the geometry of the cavity. This allows to normalise standard geometric parameters of the 1.3 GHz TESLA cavity such that the required resonant frequency is obtained. The main idea of an existing geometric shape scaling to another resonance frequency is to keep the same ellipsoid ratios that form a single cell shape. This gives a possibility to maintain the optimal RF parameters without additional geometry optimisation. It is worth noting that the same geometry scaling technique has been adopted for the design of a 9-cell 3.9 GHz SRF cavity [35]. Nine-cell 3.9 GHz cavities are presently in operation at the XFEL and the FLASH facilities. The layouts of the 1.3 GHz and 3.9 GHz TESLA cavities are illustrated in Fig. 4.2.

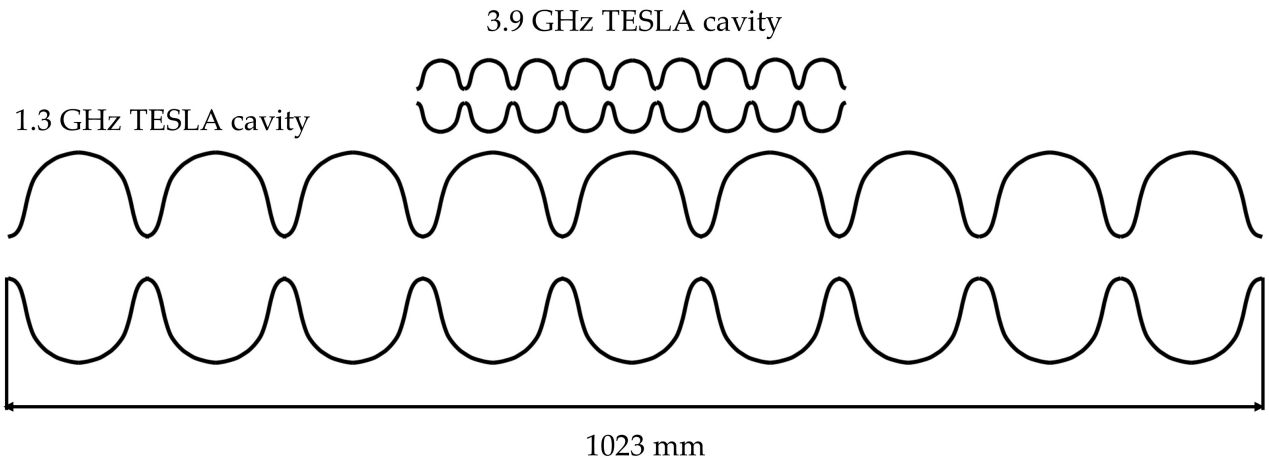

Figure 4.2: Schematic illustration of the cross sections of the 1.3 GHz and 3.9 GHz TESLA cavities.

For $\beta_g = 1$ cavities, scaling of geometric parameters depending on the required frequency is sufficient. However, the lowest velocities of accelerated beams at the S-DALINAC correspond to $\beta = 0.75$. Due to that, an optimal value of β_g is chosen below 1. When $\beta_g < 1$, TESLA shape scaling implies an additional cell geometry modification with respect to the design value of β_g. A determination of an optimal β_g value and the optimal number of cells for a reduced-β cavity based on the TESLA cell shape is discussed in the next section.

4.2 Optimal Number of Cells

The number of accelerating cells in SRF elliptic cavities is typically chosen below nine. Cavities with a large number of cells often encounter problems with field flatness tuning and trapped HOMs [14]. Cavities with a small number of cells are required to be operated with much higher accelerating gradients. In case of the S-DALINAC capture section, a 4-cell reduced-β cavity is required to be operated at $E_0 > 10$ MV/m in order to reach an output energy after the capture section W_{out} of 1 MeV. On the other hand, a 7-cell reduced-β cavity would exceed the available longitudinal space by approximately (30 ± 10) mm. As a result it is necessary to investigate the characteristics of a 5-cell and a 6-cell reduced-β cavity and motivate the choice of one of them.

EM and PT simulations were conducted with the aim to evaluate an optimal number of cells. The electromagnetic field distribution of the TM_{010}; π mode was computed for each cavity with β_g ranging from 0.8 to 0.9. Further on, beam dynamics simulations were carried out for each cavity. The RF phase has been chosen to maximise the output energy of the beam. The electric field is evenly distributed on the central cavity axis such that $\eta = (3 \pm 0.5)$ %. The results were obtained for various values of the peak electric field E_0 on the axis of the cavity. The output energy of an electron beam with an input energy E_{in} of 200 keV as a function of β_g for a 5-cell and a 6-cell cavity is shown in Fig. 4.3 and Fig. 4.4, respectively.

It is easy to see that an (N+1)-cell cavity allows operation at lower values of E_0 in comparison to an N-cell cavity to achieve the same energy gain of the beam. The optimal value of β_g depends on the operating value of E_0. For the 5-cell cavity the required energy gain is achieved for $E_0 = 7.5$ MV/m while for the 6-cell cavity a value E_0 of ≈ 6.3 MV/m is sufficient. A lower operating value of E_0 minimises the risk of field emission. Therefore, a 6-cell cavity is favoured. On the other hand, a cavity with fewer cells is mechanically more stable since the sensitivity to mechanical disturbances of the field flatness increases with an increasing number of cavity cells.

In addition, the number of cavity cells impacts the cavity longitudinal beam energy acceptance. Figure 4.5 and Figure 4.6 illustrate results of particle tracking (PT) simulations. These show the dependence of the output energy of the beam in a 5-cell $\beta_g = 0.85$ and a 6-cell $\beta_g = 0.86$ on a value of E_0 for beam initial energies varying from 50 to 250 keV with a step of 25 keV. A β_g value of 0.85 and 0.86, respectively, is motivated by an average cavity acceleration performance for values of E_0 of 6 MV/m up to 10 MV/m. Analysing the results, both cavities are capable of matching the new cavity requirements ($W \geq 1$ MeV at $E_0 \leq 10$ MV/m) for a beam injected from the SPG (200 keV) and Thermionic Gun (TG) (250 keV). However, the energy acceptance of the 6-cell cavity has a wider spectrum and includes a 100 keV beam that corresponds to an injection energy of the SPG before the planned upgrade of the gun. The effective length of the 6-cell $\beta_g = 0.86$ is equal to 253 mm which is 17 mm less compared to the available space in the existing cryostat of the capture section. Further computed results (Chapter 5) have indicated that it is possible to satisfy a minimised energy spread requirement for the 6-cell $\beta_g = 0.86$ cavity. For those reasons and taking into account the possibility of operation at a lower value of E_0 the 6-cell $\beta_g = 0.86$ cavity has been chosen for further analysis.

4.3 RF Parameters of the 6-cell Reduced-beta Cavity

Modern SRF cavities are characterised by complex geometric shapes for which the wave equation can not be solved analytically. Due to that, electromagnetic field simulations of the 6-cell $\beta_g = 0.86$ cavity have been carried out in CST MWS. A good agreement between computed results obtained in CST MWS and experimentally measured data was reported in [36] [37] [38].

A simulated model of the 6-cell cavity is represented by its inside vacuum volume surrounded by perfect electric conducting (PEC) material together with necessary boundary conditions. In that regard, RF losses are not taken into account in the simulations so far.

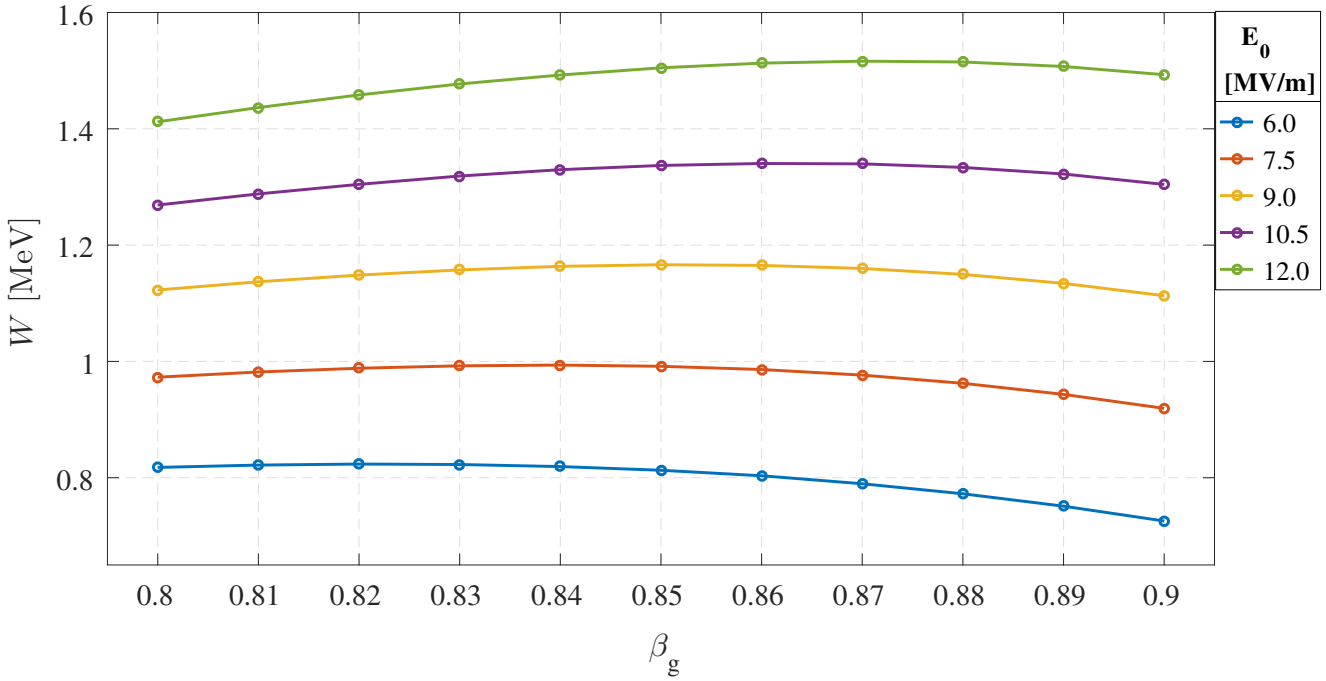

Figure 4.3: Output energy of a 200 keV beam as a function of β_g for various amplitudes of the peak electric field on the central axis of a 5-cell reduced-β cavity.

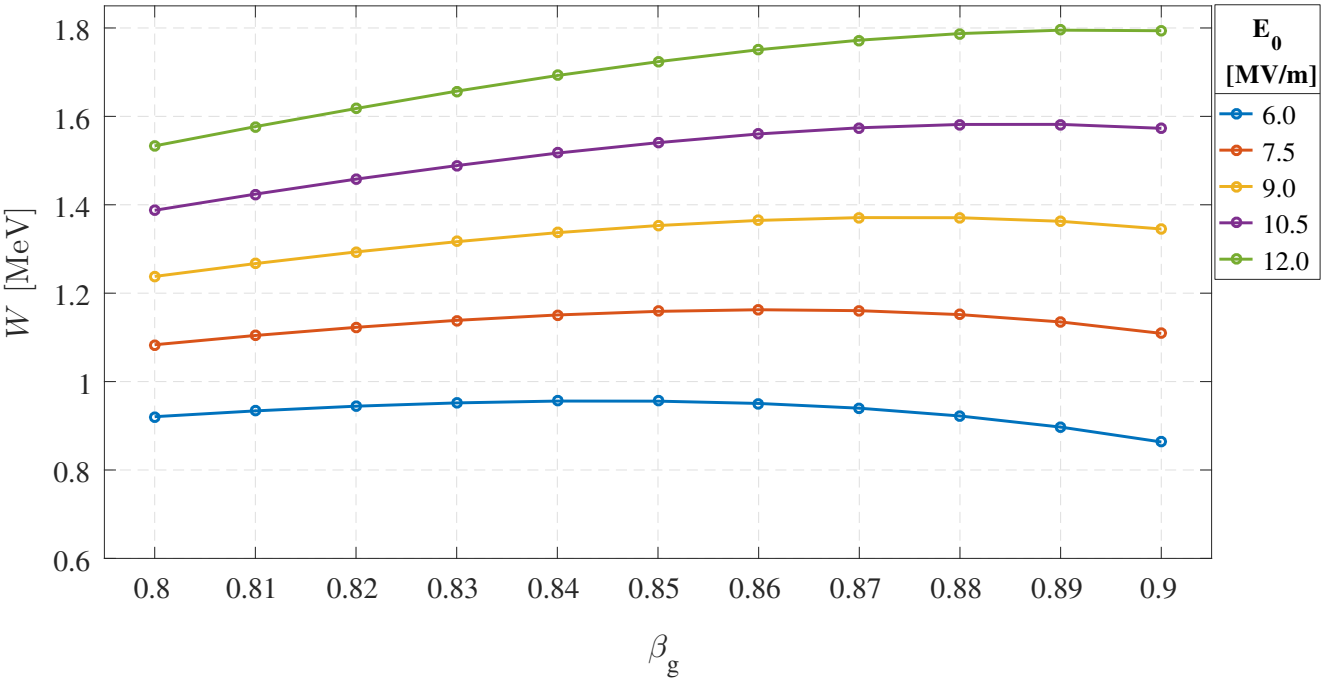

Figure 4.4: Output energy of a 200 keV beam as a function of β_g for various amplitudes of the peak electric field on the central axis of a 6-cell reduced-β cavity.

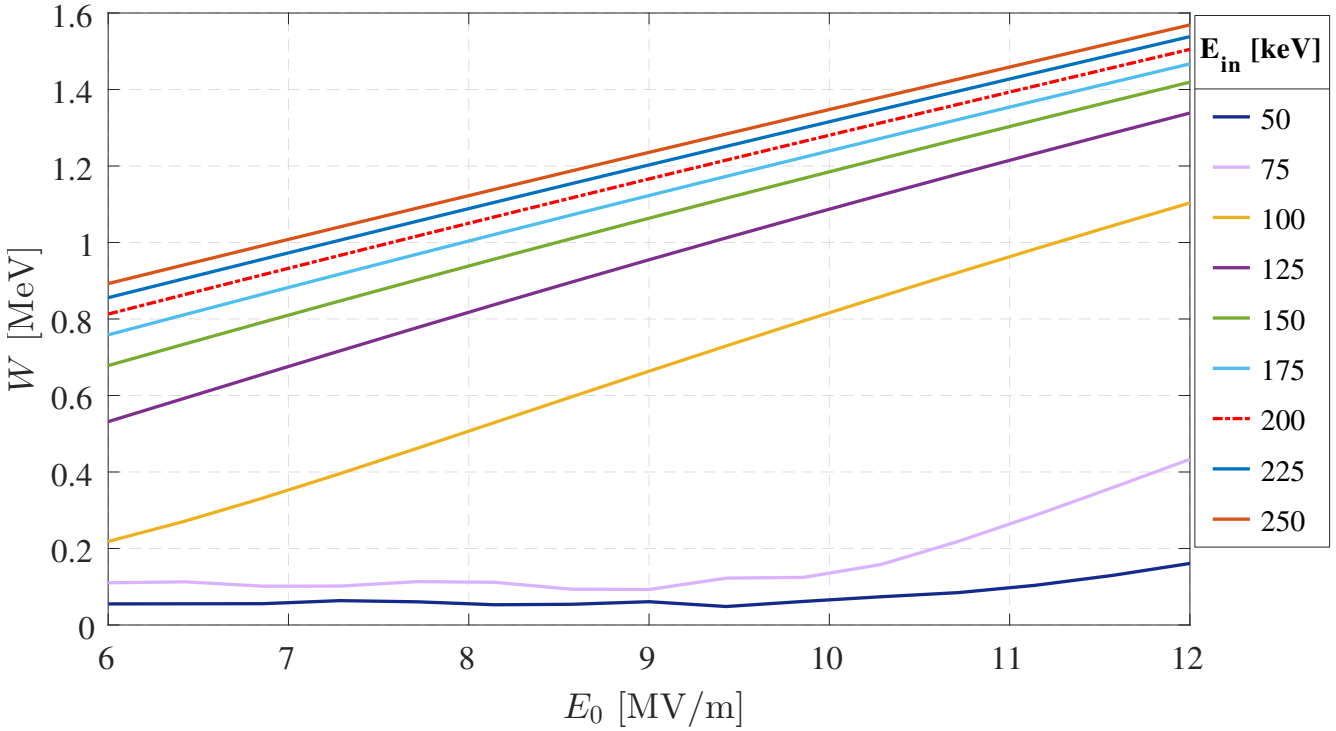

Figure 4.5: Illustration of the longitudinal energy acceptance of the 5-cell $\beta_g = 0.85$ cavity.

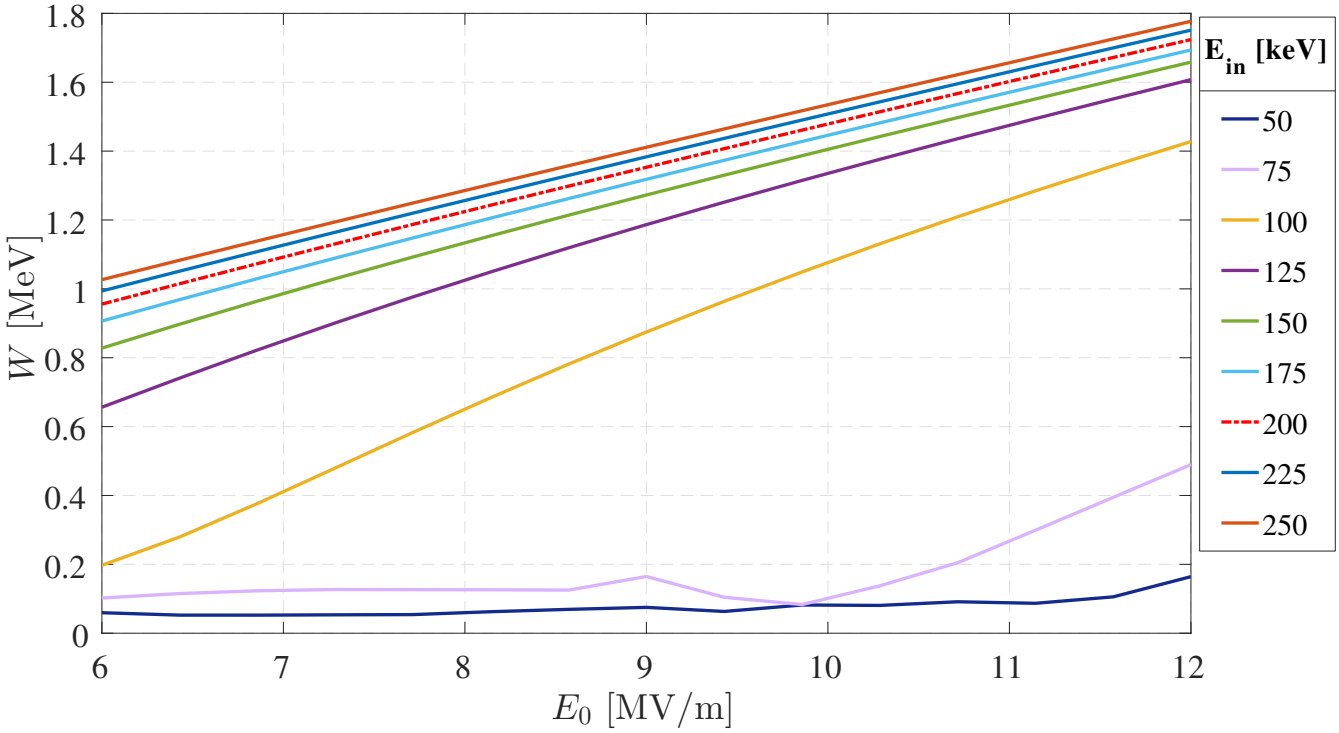

Figure 4.6: Illustration of the longitudinal energy acceptance of the 6-cell $\beta_g = 0.86$ cavity.

A full model of an RF system includes: the 6-cell cavity, beam tubes and an end-part of an RF input power coupler. The accuracy of the electromagnetic field computations in CST MWS directly depends on the model's mesh resolution. Thus, a higher calculation accuracy implies a longer computational time. The full cavity model results in a large EM problem that requires a high density meshing to obtain accurate results.

With the intend to reduce computational time, some model simplifications have been introduced. First, the full cavity model has been decoupled into two parts that are considered independently from each other (see Fig. 4.7). Second, the mid-cell group is a periodic structure that allows to consider a model of a single cell terminated by half end-cells with periodic boundary condition at the cell ends. In addition, the cavity axial symmetry has been exploited by defining the magnetic field symmetry planes for the TM_{010} mode simulations. The introduced symmetry is the same for all considered models.

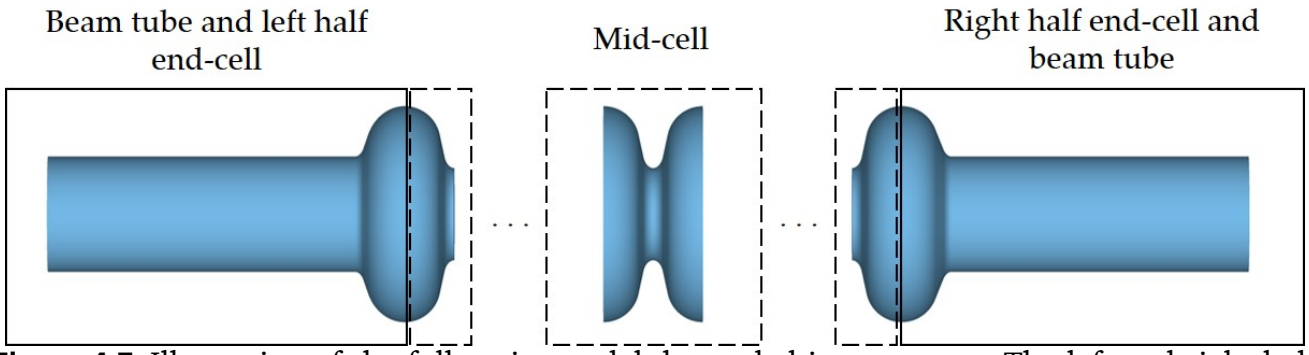

Figure 4.7: Illustration of the full cavity model decoupled in two parts. The left and right half end-cells are identical and differ from the mid-cells.

The following algorithm has been implemented and followed for the RF design of the 6-cell $\beta_g = 0.86$ cavity:

1. Design of the mid-cell.
   a) Geometry scaling of the 1.3 GHz $\beta_g = 1$ TESLA cavity to 3 GHz and additional shape modification for $\beta_g = 0.86$.
   b) Resonance frequency tuning.
   c) Investigation of the peak electric and magnetic field on the cavity inner surface.
2. Design of half end-cells. Field flatness tuning.
   a) Resonance frequency tuning of end-cells with beam pipes attached by modifying the geometry of the half end-cells.
   b) Additional field flatness optimisation for the full cavity model.
   c) Evaluation of the mode spacing for the TM_{010} mode passband.
3. Computation and analysis of the main RF parameters for the full cavity model.
4. Verification of compatibility of the electromagnetic fields and the goemetry of the designed cavity with the S-DALINAC input power coupler.

a) Justification of geometric compatibility.

b) Evaluation of coupling tuning range.

c) Analytic estimation of the required forward power value from the RF generator to the cavity with respect to resonance frequency detuning.

4.3.1 Design of the Mid-cell

The geometry of a one cell elliptic cavity is defined by two ellipsoids and a straight line connecting them (see Fig. 4.8). As it was mentioned previously, the reference shape for the 6-cell cavity is chosen to be the 1.3 GHz TESLA cavity. The geometric dimensions of the TESLA cavity have been scaled linearly such that the resonance frequency of the accelerating mode is equal to 3 GHz. Additionally, the geometry is optimised for a β_g of 0.86.

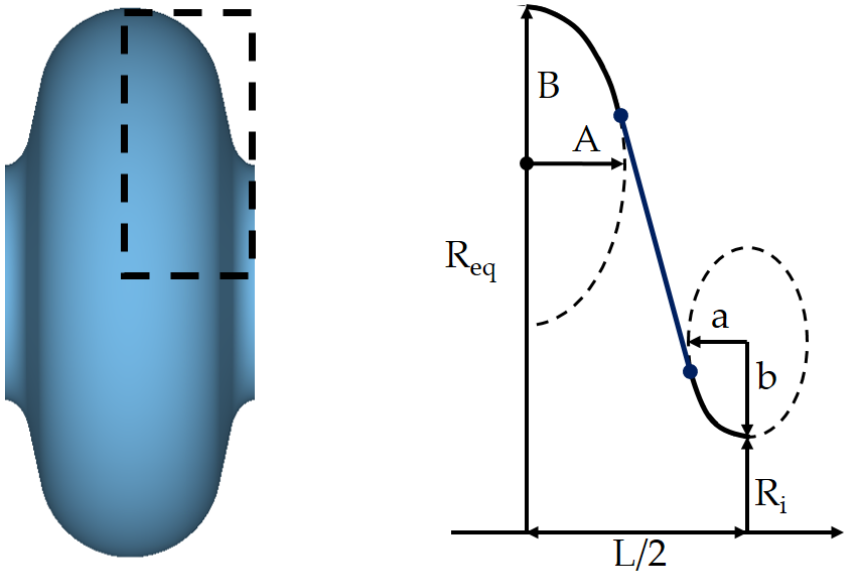

Figure 4.8: Illustration of the formation of an elliptic cavity cell shape. The shape is determined by two arcs connected by a straight line. The arcs are defined by the properties of the equator and the iris ellipsoids.

A complete model of a multi-cell RF cavity with constant cell length is a periodic structure that consists of coupled oscillators (cells). The possibility of simulating a single cell as part of a cavity with (N+1) cells is given by Floquets theorem. According to its formulation, in a passband of an infinite periodic structure, EM fields at two different cross sections that are separated by one period L differ only by a constant factor, that is in general a complex number [10]. In a lossless environment it can be expressed as follows for a cavity longitudinal electric field component:

$$E_z(x, y, z + L) = E_z(x, y, z)e^{\pm i\theta}, \tag{4.1}$$

where θ is the wave phase shift per period of a structure.

This principle has been implemented in the EM simulations by introducing periodic boundary conditions at the mid-cell half ends. Such approach allows to obtain an electromagnetic field distribution and a dispersion diagram for uniform periodic cells by choosing the necessary phase shift per period of the structure. The number of modes in the cavity passband depends on the number of cells. An N-cell cavity terminated by full cells will have N modes. An N-cell cavity that is terminated by half end-cells will have N+1 modes in the passband. A cavity simulation model with the same boundary conditions can be considered for resonance frequency tuning of a specific mode. It is worth noting that in addition to periodic boundary conditions, magnetic boundary conditions can be applied as well at the single cell ends when considering the $TM_{010};\pi$ mode.

The resonance frequency of the $TM_{010};\pi$ mode in an elliptic cavity depends on the equator radius, similarly to a pill-box cavity for which the angular frequency can be expressed analytically for TM_{010}:

$$\omega_{010} = \frac{2.405c}{R}, \tag{4.2}$$

where R is the cavity radius.

Figure 4.9 illustrates the considered 3-D model of a single mid-cell that consists of two half mid-cells with indicated boundary conditions and field symmetry planes. A $TM_{010};\pi$ resonance frequency of 3 GHz was obtained with a cell equator radius R_{eq} of 46.83 mm. The optimised geometric parameters of the central cell of the 6-cell β_g=0.86 cavity are collected in Table 4.1. These parameters apply to the remaining 4 cells which together form a group of mid-cells. The remaining two half-cells form an end-cell group and are designed independently from the mid-cells.

Parameter	Value [mm]
Equator half axis A	15.52
Equator half axis B	15.52
Iris half axis a	4.43
Iris half axis b	7.00
Equator radius R_{eq}	46.83
Iris radius R_i	20.00
Cell length L	43.00

Table 4.1: Geometric parameters of the mid-cell of the 6-cell β_g= 0.86 cavity.

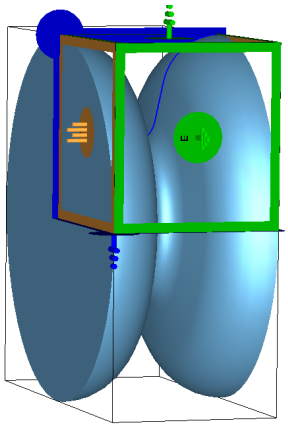

Figure 4.9: Geometry of the mid-cell of the 6-cell β_g= 0.86 cavity with indicated boundary conditions (Orange indicates a periodic boundary, blue is a magnetic field boundary and green is an electric boundary condition).

4.3.2 Peak Surface Fields

High surface EM fields in an SRF cavity can limit the cavity's acceleration performance in operation. A high surface electric field is responsible for the field emission of electrons and as a result may increase the power losses in the cavity. A high magnetic field, in turn, can potentially limit the ultimate accelerating gradient by causing breakdown of the cavity's superconductivity (quench). The probability of encountering these parasitic phenomena increases at higher field amplitudes. The impact of high surface peak fields on SRF cavities as well as cavity surface treatment techniques applied to minimise the possibility of the field emission and quench are further discussed in [19].

To investigate the surface fields in the 6-cell $\beta_g = 0.86$ cavity, a single mid-cell has been considered in EM simulations. Electric and magnetic field distributions of the TM_{010} mode are illustrated in Fig. 4.10. Black dash line indicates the curve path at which the amplitudes of the surface electric and magnetic field were evaluated. The electric and magnetic surface field amplitudes as a function of the longitudinal coordinate z evaluated on a curve that represents a part of the cavity surface are indicated in Fig.4.11. The peak fields evaluated in the EM model are the following:

$$E_{\mathrm{p}} = 17.2 \left[\frac{\mathrm{MV}}{\mathrm{m}}\right];\ H_{\mathrm{p}} = 22.3 \left[\frac{\mathrm{kA}}{\mathrm{m}}\right]. \tag{4.3}$$

The range of reliable peak field amplitudes based on operational experience for Nb cavities was reported in [39] and is the following:

$$E_{\mathrm{p.rel.}} = (30-35) \left[\frac{\mathrm{MV}}{\mathrm{m}}\right];\ H_{\mathrm{p.rel.}} = (48-56) \left[\frac{\mathrm{kA}}{\mathrm{m}}\right]. \tag{4.4}$$

The evaluated peak surface field values are well below the recommended reliable amplitude range. Hence, an additional cell geometry optimisation is not required for the 6-cell cavity. In the opposite case, when higher levels of the peak surface fields would occur the cavity, its geometry needs to be further optimised. The main geometric parameter that allows to modify the peak field values is the cavity iris radius. When the cavity iris radius is fixed due to particular reasons (HOM, coupling coefficient etc.), a modification of an ellipsoid parameter that determines the cavity iris region and of the parameters of an equator ellipse allow to further optimise the peak surface fields.

4.3.3 Field Flatness Optimisation

In a multi-cell RF cavity operated with the $TM_{010};\pi$ mode, the peak electric field amplitude E_0 on the central axis of the cavity can differ from cell to cell. A large difference results in an uneven electric field distribution on the central cavity axis. This leads to an unpredictable beam acceleration and affects all the critical RF parameters of an RF cavity. Thus, it is absolutely necessary to achieve an acceptable field flatness during the RF cavity design and in operation.

The field flatness of an N-cell cavity can be expressed as follows [40],

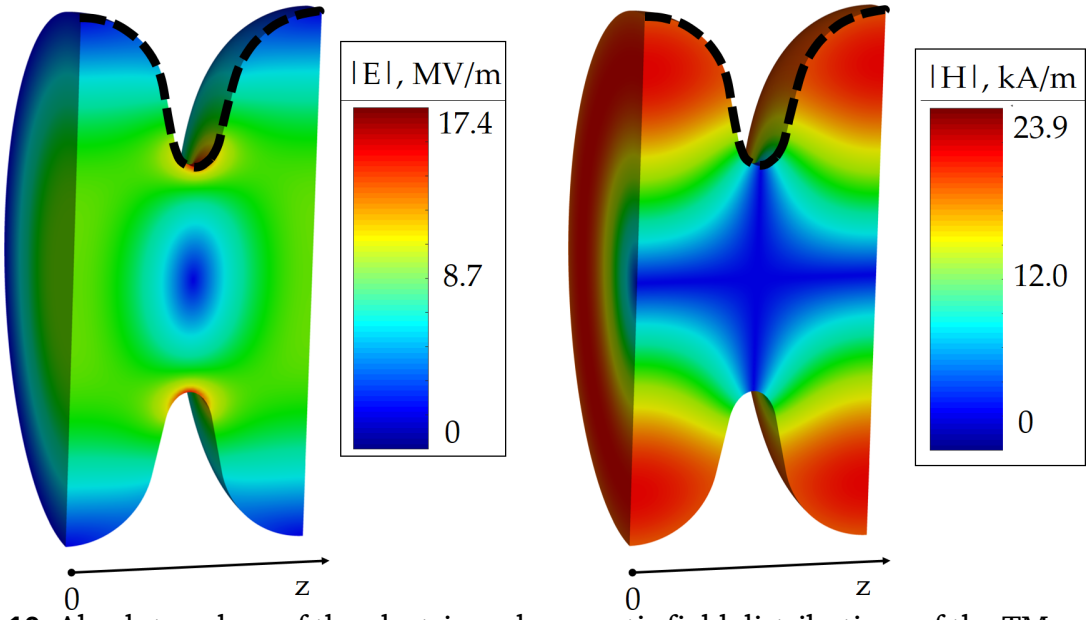

Figure 4.10: Absolute values of the electric and magnetic field distributions of the $TM_{010};\pi$ mode in the mid-cell of the 6-cell cavity. The field amplitudes are normalised to E_0=10 MV/m.

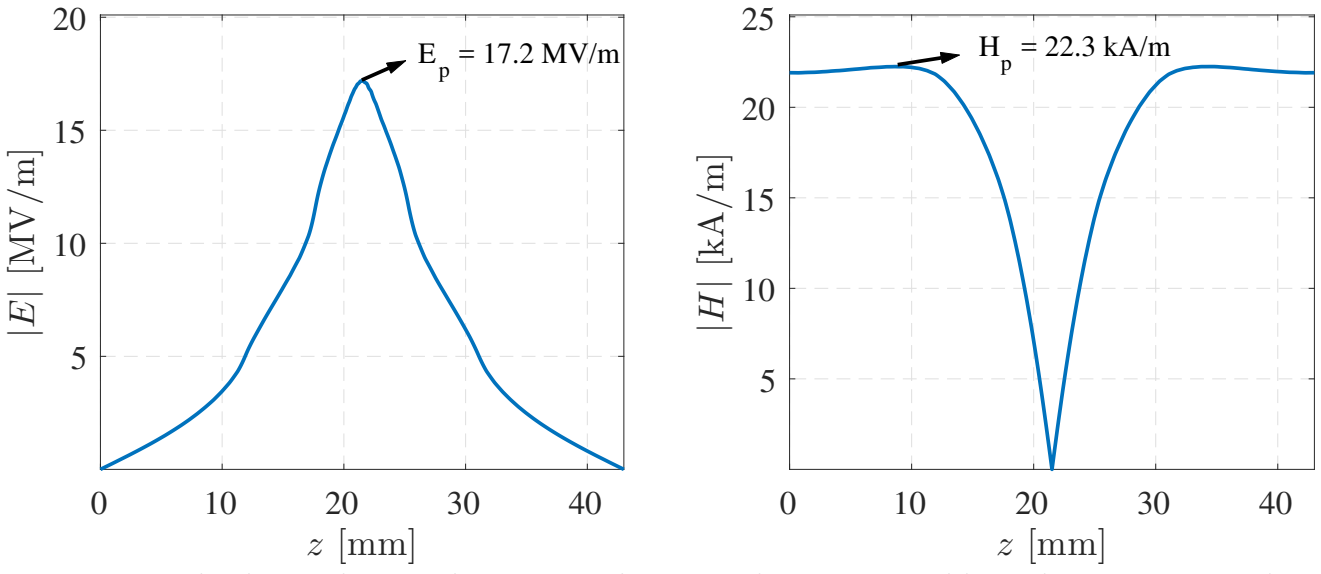

Figure 4.11: Absolute values of the surface electric and magnetic fields of the $TM_{010};\pi$ mode in the mid-cell of the 6-cell cavity. The field amplitudes have been evaluated on the black dashed line shown in Fig. 4.10. The amplitudes are normalised such that E_0=10 MV/m.

$$\eta = \frac{V_{\text{acc. max.}} - V_{\text{acc. min.}}}{\frac{1}{N}\sum_{i=1}^{N} V_{\text{acc.}i}} \cdot 100\%, \tag{4.5}$$

where $V_{\text{acc. max.}}$ and $V_{\text{acc. min.}}$ correspond to the maximum and minimum cell voltages in the cavity and $V_{\text{acc.}i}$ is the acceleration voltage in the i-th cell.

Inserting the relation between V_{acc} and E_0, expression (4.5) can be re-formulated in terms of the peak electric field on the central cavity axis:

$$\eta = \frac{E_{0\text{ max.}} - E_{0\text{ min.}}}{\frac{1}{N}\sum_{i=1}^{N} E_{0i}} \cdot 100\%. \tag{4.6}$$

Differences in geometry between the mid-cells and the half end-cells and an additional capacitance introduced to the cavity by the beam tubes leads to a non-uniform electric field distribution on the central axis of the 6-cell $\beta_g = 0.86$ cavity. The difference in geometry arise due to the fact that the iris radius of the half end-cells corresponds to the radius of the beam tubes. This was done in order to provide a smooth transition between the end-cells and the beam tubes. The smooth transition results in an increased longitudinal mechanical cavity stiffness. For a better understanding of the field flatness problem one can consider lumped circuit theory, that can be applied to an RF analysis [14]. In this approach a de-tuned cavity operated with the $\text{TM}_{010};\pi$ mode without losses can be represented by capacitively coupled LC oscillators with introduced frequency errors and additional capacitive elements representing the effects of the presence of beam tubes.

In order to obtain a uniform electric field distribution of the $\text{TM}_{010};\pi$ mode, the resonance frequency was tuned to 3 GHz for the left end-cell of the cavity with attached beam pipe. The correction to the resonance frequency has been introduced by modifying the shape of the half end-cell without changing the equator radius or the total cell length. Further on, the full cavity model was assembled. A field flatness calculation yields $\eta = 6.9$ % which is 1.9 % larger compared to the recommended value. This is explained by the fact that the magnetic field boundary conditions implemented during the end-cell frequency tuning does not represent an actual coupling between the cavity cells. An additional field flatness optimisation continued by applying a genetic optimisation algorithm for the full cavity geometry. Four geometric parameters that characterise two identical left and right half end-cells were involved in the optimisation procedure. The optimised geometric parameters of half end-cells that correspond to $\eta = 2.8\%$ are collected in Table 4.2. The electric field distributions of the tuned and de-tuned 6-cell $\beta_g = 0.86$ cavity are illustrated in Fig. 4.13

In practise, after a cavity is manufactured, the field flatness has to be tuned again due to manufacturing errors and cavity inner surface treatments, that are typically applied to obtain the necessary surface quality and eliminate inner surface defects. The tuning parameters are obtained through electric field profile measurements on axis using a bead-pull method [10]. Once the field profile is obtained, a circuit analogy of the cavity can be

Parameter	Value [mm]
Equator half axis A	15.52
Equator half axis B	15.52
Iris half axis a	4.43
Iris half axis b	7.00
Equator radius R_{eq}	46.83
Iris radius R_i	20.00
Cell length L	43.00

Table 4.2: Geometric parameters of the half end-cells of the 6-cell $\beta_g = 0.86$ cavity.

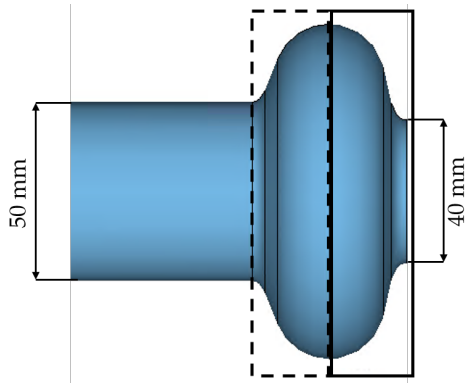

Figure 4.12: Geometry of the left end-cell of the 6-cell $\beta_g = 0.86$ cavity.

implemented. Further on, the field flatness is tuned by mechanically squeezing or stretch the body of the cavity.

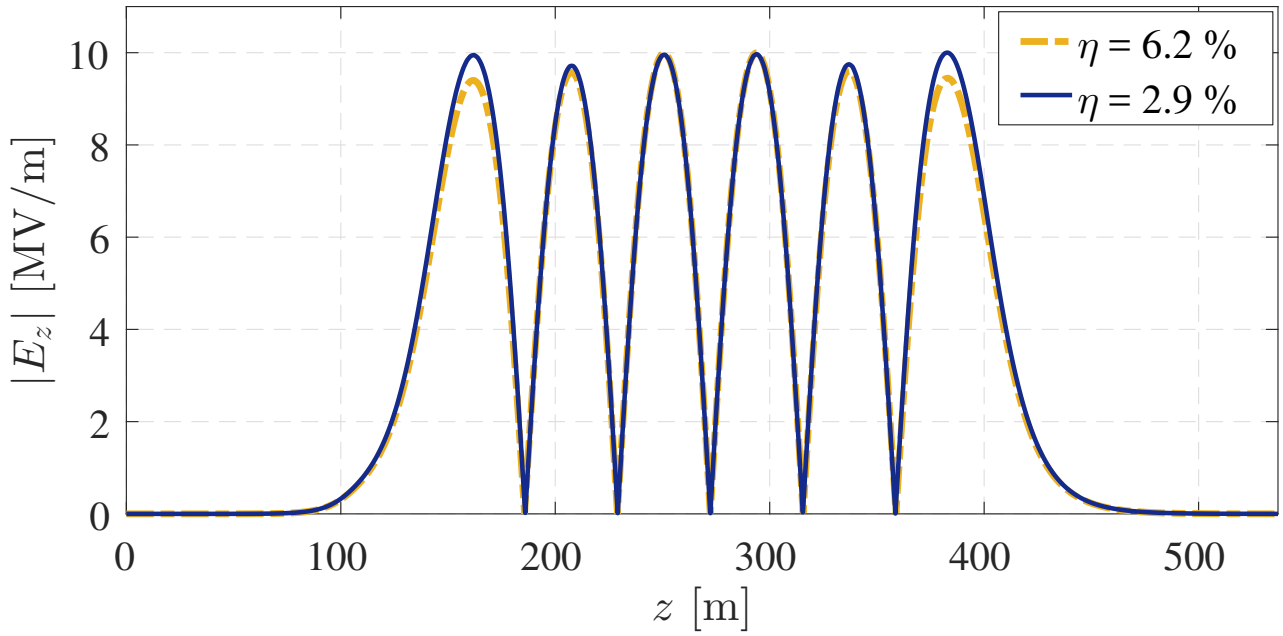

Figure 4.13: Absolute values of the longitudinal electric field distribution on the central axis of the 6-cell $\beta_g = 0.86$ cavity operated with the $TM_{010};\pi$ mode.

4.3.4 Mode Spacing

The 6-cell $\beta_g = 0.86$ cavity TM_{010} mode passband consists of 6 modes. Each mode is characterised by a field phase shift between cells and resonance frequency. These modes are present in the cavity during operation, however, their amplitudes are significantly lower in comparison to the amplitude of the accelerating mode. In a situation when one of the mode resonance frequencies is too close to the operating mode resonance

frequency it can be excited together with the operating one. This, in turn, has a negative impact on the beam quality.

It is necessary to refer to a cavity dispersion diagram that is a useful tool for the analysis of the cavity mode frequency spacing. The eigenfrequencies were computed for the TM_{010} mode of the 6-cell $\beta_g = 0.86$ cavity with attached beam pipes. Figure 4.14 illustrates the obtained dispersion diagram for the 6-cell cavity. In a multi-cell cavity operated with the $TM_{010};\pi$ mode and with cavity ends terminated by full cells, the phase shift per period (cell) θ is expressed as follows:

$$\theta = \frac{m\pi}{N}, \tag{4.7}$$

where N is the number of cavity cells, and m is the mode number

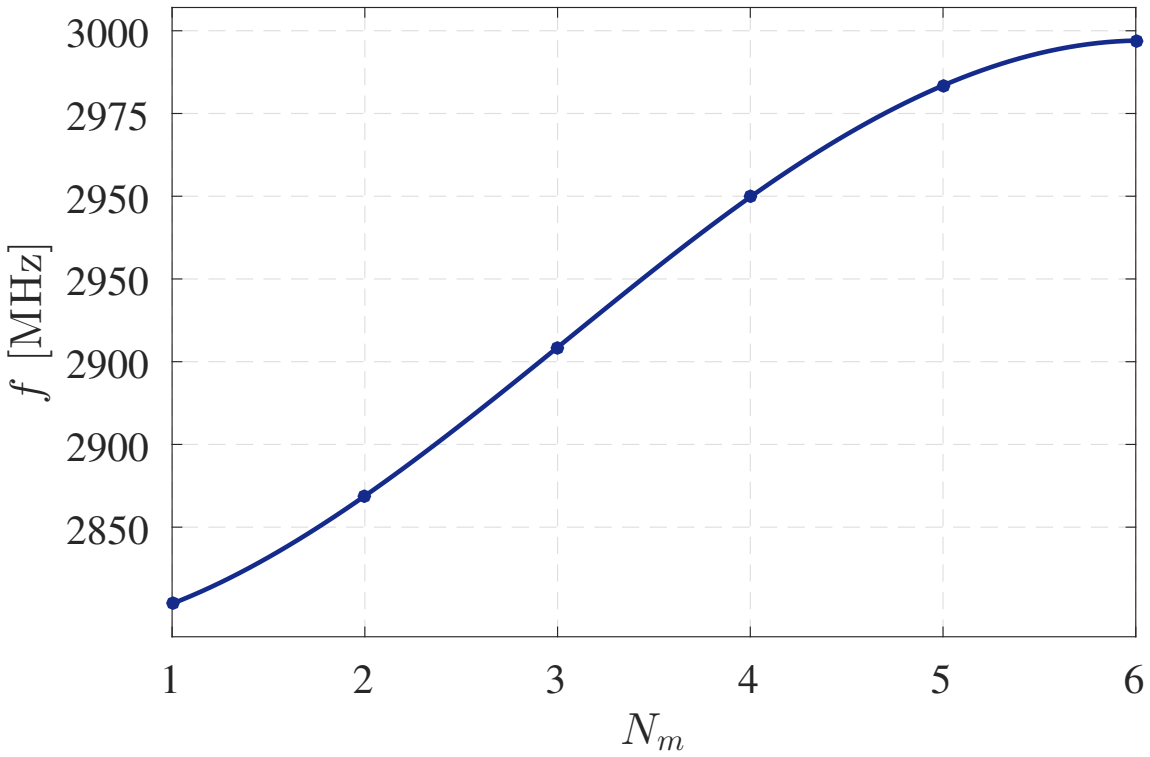

Figure 4.14: TM_{010} passband of the 6-cell $\beta_g = 0.86$. The number of modes corresponds to the number of cells.

The dispersion relation can be represented analytically for mode m as follows [14]:

$$\frac{f_m}{f_0} = 1 + 2k_c\left[1 - \cos\left(\frac{m\pi}{N}\right)\right], \tag{4.8}$$

where f_0 is the resonance frequency of an individual (not coupled) oscillator (cell), f_m is the resonance frequency of mode m, N is the number of cells of a cavity and k_c is the cell-to-cell coupling coefficient.

The cell-to-cell coupling coefficient k_c is a measure of how strong the cells are coupled. Increasing the coupling coefficient increases the mode spacing in a cavity. The cell-to-cell coupling coefficient for a cavity operated with the $TM_{010};\pi$ mode is written as follows:

$$k_c = 2 \cdot \frac{f_\pi - f_0}{f_\pi + f_0} \cdot 100\%. \tag{4.9}$$

From (4.9) the cell-to-cell coupling coefficient k_c of the TM_{010} mode of the 6-cell reduced-β cavity corresponds to 5.8 %. The value of k_c can be adapted by modifying the cavity iris radius. A typical target value of k_c for an elliptic SRF cavity is $k_c \geq 2$ % [14]. The iris radius value for the 6-cell $\beta_g = 0.86$ cavity is fixed. Hence, the coupling coefficient value is fixed and can not be modified. Due to a moderate accelerating gradient of the 6-cell cavity it is possible to allow for an operation with a large coupling coefficient and minimise risks related to field flatness detuning issues. The pay-off for an increased coupling coefficient is a decreased *R-over-Q value* and increased peak surface field values due to the large iris radius of cells. In addition, the value of the coupling coefficient affects the cavity power filling time. However, this problem is more relevant when the cavity is operated in pulsed regime.

4.3.5 Key Characteristics of the Cavity

One of the most important figures of merit that characterises the cavity performance is the effective accelerating voltage V_{acc}. The evaluation of other RF parameters such as the *R-over-Q value* and the accelerating gradient E_{acc} is based on the value of V_{acc}. By definition, the effective accelerating voltage depends on the beam velocity. The beam velocity in the 6-cell $\beta_g = 0.86$ cavity changes significantly during the acceleration process. Hence, the value of the accelerating voltage varies along the longitudinal coordinate. In that regard, RF parameters of the 6-cell cavity that are defined through V_{acc} indicate average values and characterise the full cavity and can not be used to precisely characterise the performance of a particular single cell of the cavity. Table 4.3 summarises the calculated RF parameters of the 6-cell $\beta_g = 0.86$ cavity as well as some other cavity characteristics. It is worth noting that all of the obtained RF parameters are loss-independent. The full cavity model equipped with the S-DALINAC power coupler is illustrated in Fig. 4.15.

It is convenient to compare RF parameters of a new SRF cavity to parameters of existing structures in operation. Multi-cell reduced-β cavities in the frequency range of 3 GHz that are implemented for low electron beam acceleration do not exist up to date. In that regard, the obtained RF parameters values are assessed with a reference to the available data related to operational experience of SRF cavities.

An accelerating gradient of 4.8 MV/m satisfies the necessary beam output energy requirement for the new cavity. The *R-over-Q value* could be potentially increased, however, due to the priority of mechanical stability, the cavity iris radius is fixed. The iris radius value of the half end-cells corresponds to the radius of the beam pipes that are a part of the current setup of the capture section. A payoff for the longitudinal cavity stiffness and compatibility with the coupler is a decrease of the acceleration performance in terms of

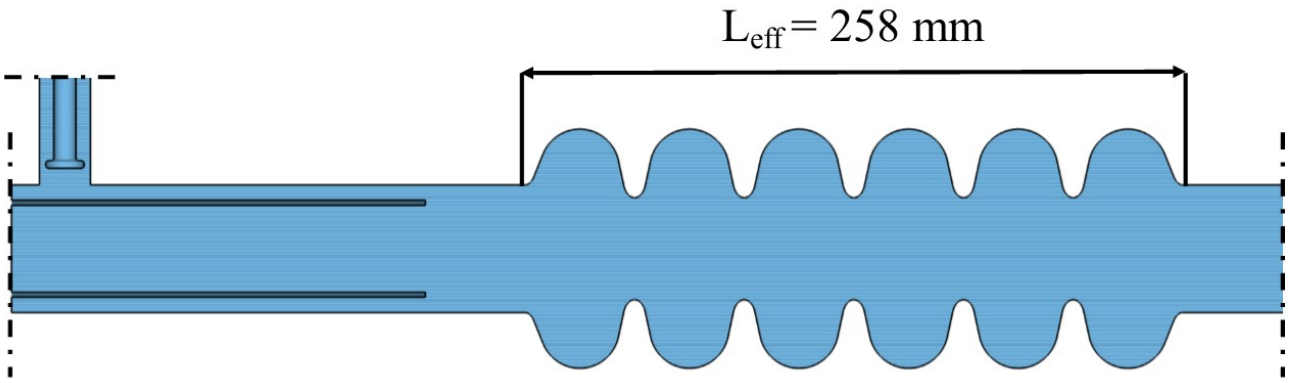

Figure 4.15: Cross section of the full cavity model with the effective length of the cavity indicated. The end part of the RF power input coupler is illustrated on the left-hand side.

Parameter	Value
Operating mode	TM_{010}
Phase shift θ, °	π
Resonance frequency f, GHz	2.997
Operation regime	CW
Number of cells	6
Coupling coefficient k_c, %	5.8
Field flatness η, %	2.8
Peak electric field on axis E_0, MV/m	10
Cavity effective length L_{eff}, mm	258
Accelerating voltage V_{acc}, MV	1.2
Accelerating gradient E_{acc}, MV/m	4.8
Quality factor Q_0	10^9
R-over-Q value, Ω	308
Geometry factor G, Ω	254
Peak surface electric field E_p, MV/m	17.2
Peak surface magnetic field B_p, mT	22.3
Cavity material	Nb
RRR	250

Table 4.3: Parameters of the 6-cell $\beta_g = 0.86$ cavity.

the accelerating voltage and *R-over-Q value*. The remaining parameters do not require additional tuning. Despite the fact that the new cavity requirements do not allow to modify some of the 6-cell cavity geometric parameters, it is necessary to explain the main dependencies of the RF parameters on changes of the iris radius. In general, there is always a trade-off depending on the desired cavity specifications. If the aim is to achieve a high accelerating gradient (25-40 MV/m) the iris radius value should be minimised. This, in turn, leads to a higher HOM impedance and reduces the cell-to-cell coupling coefficient. The effect of changes to the elliptic cavity iris radius on the cavity RF characteristics are collected in Table 4.4.

Parameter	Increase	Decrease
R-over-Q value	$R_i \downarrow$	$R_i \uparrow$
Coupling coefficient k_c	$R_i \uparrow$	$R_i \downarrow$
Peak surface electric field E_p	$R_i \uparrow$	$R_i \downarrow$
Peak surface magnetic field H_p	$R_i \uparrow$	$R_i \downarrow$

Table 4.4: Dependence of different RF parameters on the iris radius of an elliptic cavity.

4.4 Coupling of the Cavity to the Power Generator

Figure 4.16 shows a block-scheme that contains the main components of the RF power system for an RF cavity. RF power is transmitted from the RF generator to the RF cavity using waveguide transmission lines. An RF circulator is installed between the RF generator and the power coupler to ensure that EM waves reflected from the cavity are not transmitted back to the generator, but instead dissipated in a matched load. To analyse the coupling between waveguide and cavity, it is necessary to refer to quality factor definitions.

The quality factor Q_0 of an unloaded cavity is expressed as

$$Q_0 = \frac{2\pi f U}{P_{cav}}, \tag{4.10}$$

where U is the energy stored in the cavity, P_{cav} is the power dissipated in the cavity and f is the resonance frequency of the accelerating mode.

The quality factor related to an external cavity load is named as an external Q factor (Q_{ext}) and it is expressed as

$$Q_{ext} = \frac{2\pi f U}{P_{ext}}, \tag{4.11}$$

where P_{ext} is power dissipated in an external load.

The total dissipated power in the system is $P = P_{\mathrm{cav}} + P_{\mathrm{ext}}$, and the loaded Q factor is given by

$$Q_{\mathrm{L}} = \frac{2\pi f U}{P}. \tag{4.12}$$

From (4.10) - (4.12) the quality factors are related as

$$\frac{1}{Q_{\mathrm{L}}} = \frac{1}{Q_0} + \frac{1}{Q_{\mathrm{ext}}}. \tag{4.13}$$

To assess the coupling strength between the waveguide and the cavity, the coupling coefficient definition [10] is introduced and it is defined as follows:

$$\beta_{\mathrm{c}} = \frac{P_{\mathrm{ext}}}{P_{\mathrm{c}}} = \frac{Q_0}{Q_{\mathrm{ext}}} \tag{4.14}$$

The critical coupling regime corresponds to $\beta_{\mathrm{c}} = 1$, while for $\beta_{\mathrm{c}} < 1$ the cavity and the waveguide are undercoupled and for $\beta_{\mathrm{c}} > 1$ the cavity and the waveguide are overcoupled. Critical coupling implies a complete matching between the cavity and the waveguide and, thus, absence of reflected power. Therefore, this coupling regime is preferred. However, SRF cavities are operated with Q_0 values of 10^9 ... 10^{10}. Considerably high Q_0 values demand an operation with high loaded Q_{L} values $\left(Q_{\mathrm{ext}} = Q_0 \Rightarrow Q_{\mathrm{L}} = \frac{Q_0}{2}\right)$. This leads to a very narrow resonance bandwidth of only a few Hz and a great difficulty in controlling and adjusting the resonance frequency of a cavity in operation.

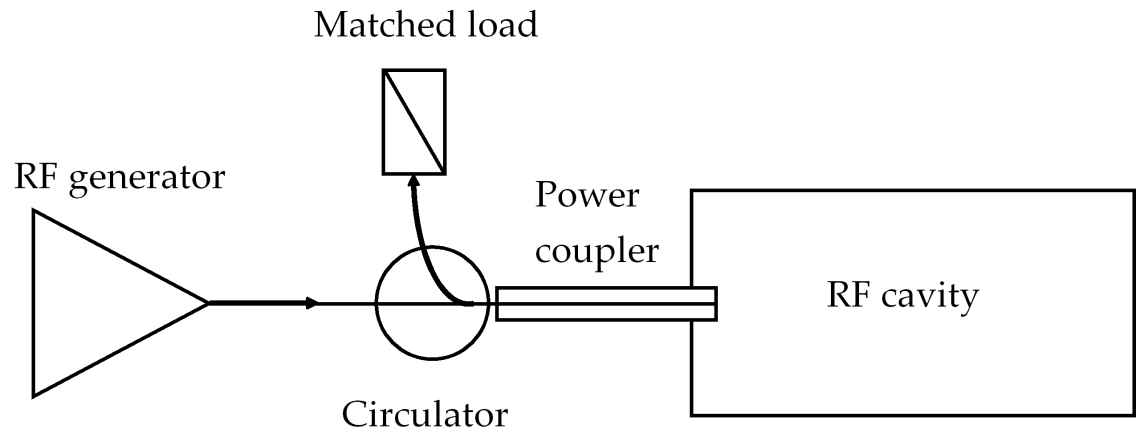

Figure 4.16: Schematic illustration of the main components that are implemented for the coupling of a cavity to an RF power source.

4.4.1 Tuning Range of Coupler

The RF input power coupler in the capture section consists of a coaxial line which is then connected to a second coaxial line for which the cavity beam pipe acts as an outer conductor. From the second coaxial line the power is transferred to the cavity.

In order to verify the geometric and the electromagnetic compatibility of the existing RF power input coupler and the 6-cell $\beta_g = 0.86$ cavity, the necessary RF computations were carried out. This includes the verification of the necessary tuning range coverage to obtain the required Q_L values. The inner conductor of the first coaxial line is movable in the x direction, so it is possible to adjust the coupling coefficient between the cavity and the coupler by manipulating Q_{ext}. The simulated model consists of the cavity and the input coupler with matched ports. The penetration depth of the inner conductor x is defined as the distance between the first coaxial line inner conductor end and the surface of the inner conductor of the second coaxial line (see Fig. 4.17).

Figure 4.18 illustrates the dependence of Q_{ext} and Q_L on the penetration depth x. The results obtained for Q_L are valid for the cavity with $Q_0 = 10^9$. Taking into account the fact that typical values of Q_L in operation range from 10^6 to 10^8 the existing RF power coupler covers the necessary coupling coefficient tuning range for the 6-cell cavity.

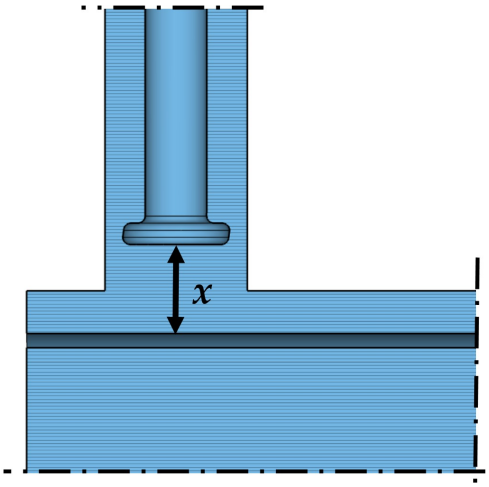

Figure 4.17: End-part of the power coupler of the 6-cell cavity.

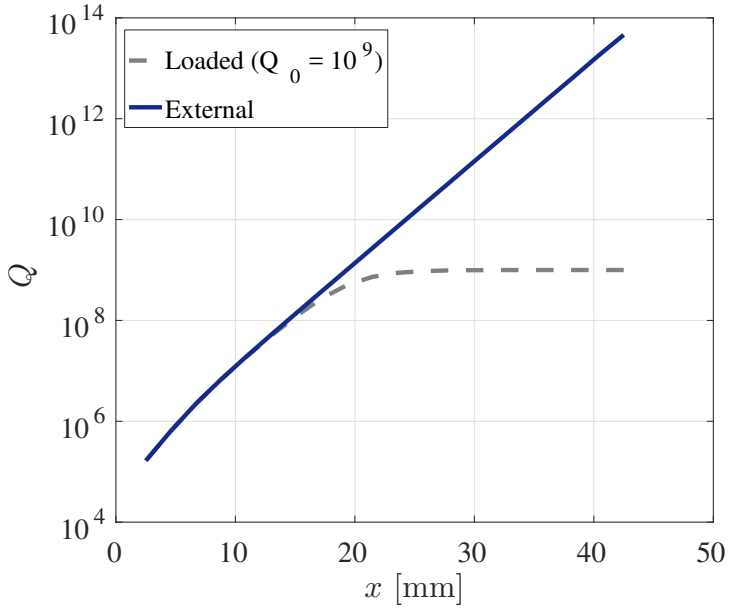

Figure 4.18: Q-factors as a function of the penetration depth of the inner conductor.

4.4.2 Necessary RF Power for the 6-cell Cavity

The forward RF power P_f from the S-DALINAC RF amplifiers is limited to 500 W. The required P_f value for the 6-cell cavity mainly depends on the beam current, the accelerating voltage, the coupling coefficient and the frequency detuning level. From the LRC-circuit analogy of an RF cavity that includes a generator, a cavity and a beam, the required forward power from the generator is expressed analytically as follows [14]:

$$P_f = \frac{V_{acc}^2}{4\left(\frac{R}{Q}\right)Q_L} \cdot \left(\left(1 + \frac{\left(\frac{R}{Q}\right)Q_L I_b}{V_{acc}} \cos\phi_b \right)^2 + \left(\frac{\Delta f}{f_{1/2}} + \frac{\left(\frac{R}{Q}\right)Q_L I_b}{V_{acc}} \sin\phi_b \right)^2 \right), \qquad (4.15)$$

where $f_{1/2}$ is the half-bandwidth of the resonance, Δf is the frequency detuning, I_b is the beam current and ϕ_b is the synchronous beam phase.

The operation of an SRF cavity with high Q_0 value assumes a narrow resonance frequency width in order of 10-100 Hz. Due to that, SRF cavities are extremely sensitive to any mechanical loads that deform the geometry and thereby perturb the resonance frequency. An SRF cavity in operation is affected by various external mechanical loads originating from pressure fluctuations in the cryostat, mechanical vibrations and beam loading. In order to compensate a resonance frequency detuning Δf digital low-level RF (LLRF) systems are implemented. A typical LLRF system monitors and controls the RF field in a cavity. Field correction is carried out by taking into account cavity probe signal errors and adjusting a low power wave that drives the RF amplifier. In addition, a cavity is equipped with fast frequency mechanical tuners that are based on piezoelectricity. However, any LLRF system has a limited tuning range. Due to that, in some cases resonance frequency detuning is present in operation but can not be fully eliminated by a frequency tuning system. The remaining frequency detuning is compensated by increasing the value of forward power.

Figures 4.19 and 4.20 illustrate the forward power as function of the loaded Q-factor for zero beam loading and for I = 20 μA, respectively. Analysing the results, it is easy to see that the beam loading of the 6-cell cavity is considerably low. The operating value for Q_L should be chosen based on the detuning level and with respect to the capability of the existing S-DALINAC LLRF systems. For the considered range of Δf the optimal Q_L value is in the range from $5 \cdot 10^6$ up to 10^8. This Q_L range corresponds to an overcoupled regime ($\beta_c > 1$). A stable operation is achieved at lower Q_L values ($5 \cdot 10^6$) due to a broader resonance bandwidth, however, more forward power is required.

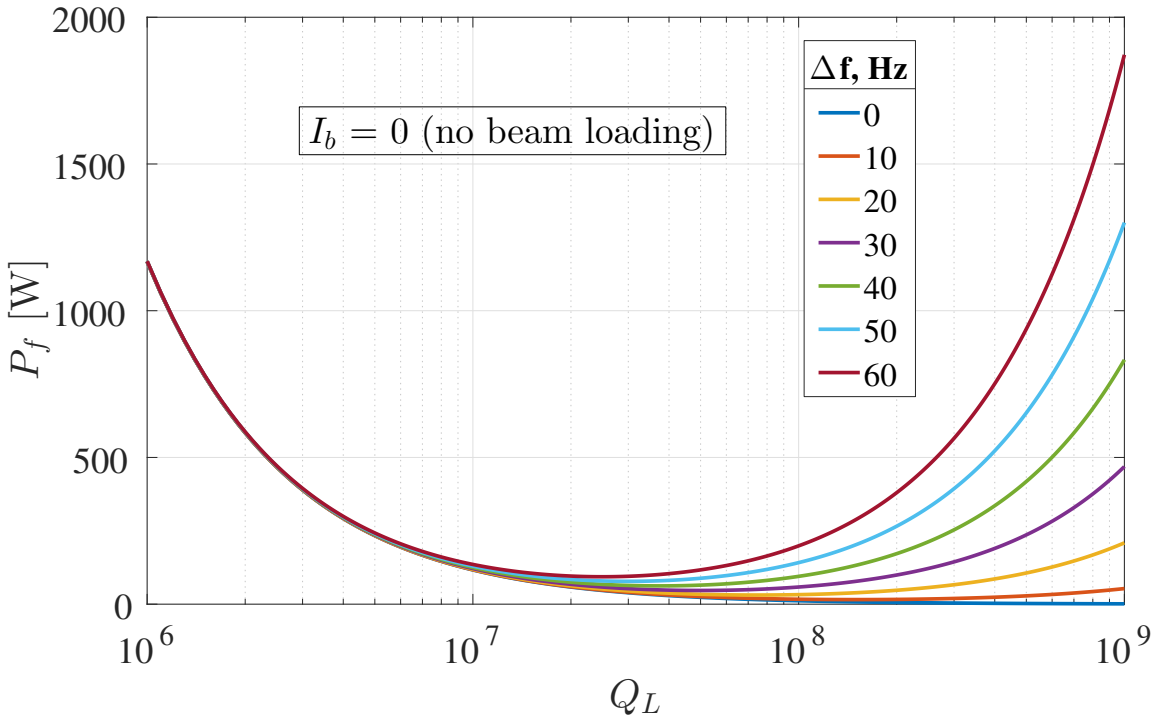

Figure 4.19: Generator forward power as a function of the cavity Q_L value for various resonance frequency detuning Δf values. The beam current corresponds is 0.

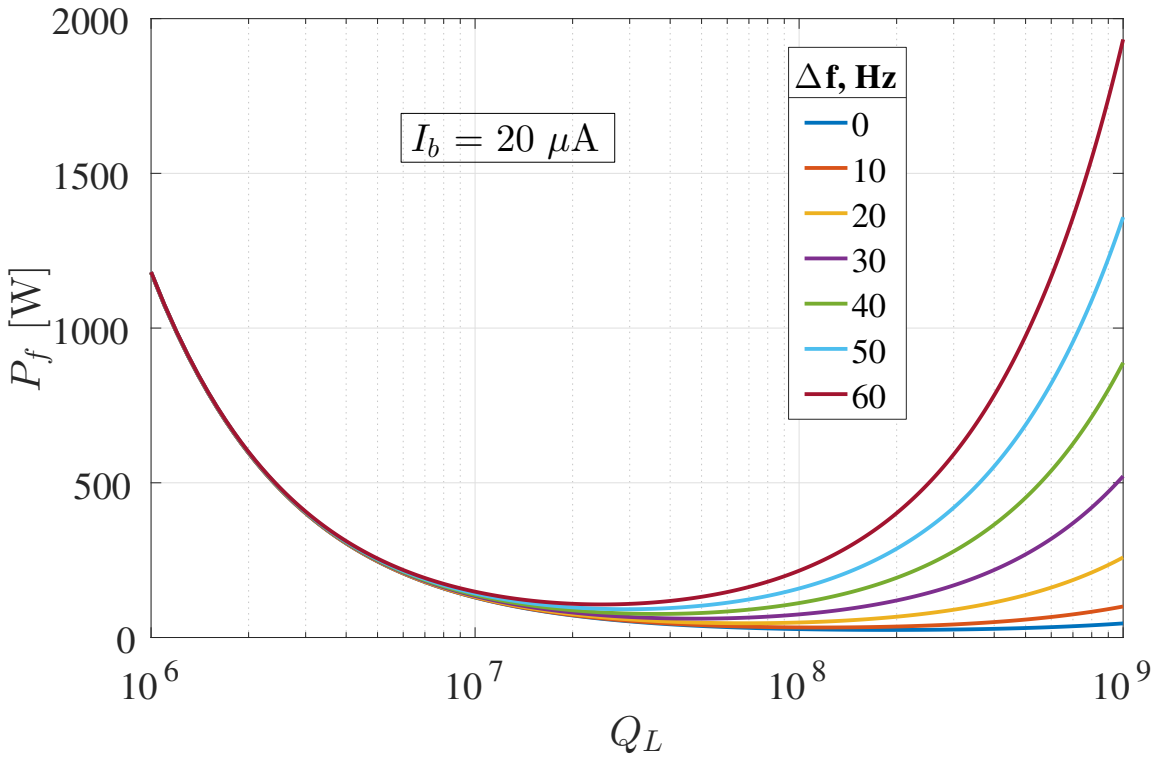

Figure 4.20: Generator forward power as a function of the cavity Q_L value for various resonance frequency detuning Δf values. The beam current corresponds is 20 μA.

To conclude, the existing RF input power coupler successfully covers the necessary tuning range of the 6-cell cavity coupling coefficient. The required generator forward power level depends on the chosen Q_L-value. For the considered model the necessary forward power is four times lower (in the considered frequency detuning range) then maximum power provided by the available RF power amplifiers at the S-DALINAC.

4.5 Conclusion

As a result of the quantitative analysis, which includes the electromagnetic simulations and the longitudinal beam dynamics simulations, an optimal value of the number of cells and an optimal value of the length of the accelerating gaps (cells) for an SRF reduced-β cavity has been determined.

The designed layout of the cavity for the upgrade of the capture section is a 6-cell structure of elliptic type. The geometry of the accelerating cells has been chosen based on the geometry of the 1.3 GHz 9-cell TESLA cavity, which was optimised for the operating frequency of 3 GHz and the geometric beta of $\beta_g < 1$. One of the main consequences of a value of $\beta_g < 1$ is an increased amplitude of the electromagnetic fields at the inner surface of the 6-cell cavity. However, a detailed analysis of the problem indicated that at the designed accelerating gradient, the amplitudes of the surface fields are in the recommended reliable range. The RF parameters of the 6-cell cavity satisfy the requirements for the upgrade of the capture section.

The possibility of operation of the 6-cell cavity with the existing RF input power coupler has been proved in EM simulations. For the designed accelerating gradient, the analytic

calculations of the required values of the input of RF power have been carried out for the 6-cell cavity. The results of the calculations allow to choose the optimal value of the loaded Q factor in operation, while taking into account the detuning of the resonance frequency of the accelerating mode of the 6-cell cavity. Taking into account the detuning of the resonance frequency, the RF power required to maintain the designed accelerating gradient E_{acc} of 4.8 MV/m, is four times lower than the maximum RF power that can be provided by the existing RF amplifier at the S-DALINAC.

5 Longitudinal Beam Dynamics in the 6-cell Cavity

This chapter discusses the results of the beam dynamics computations for the 6-cell $\beta_g = 0.86$ cavity. The goal is to evaluate the energy gain and the longitudinal energy spread of the 200 keV and 250 keV beams accelerated in the cavity at the designed accelerating gradient of the $TM_{010};\pi$ mode. In addition, the dependence of the beam characteristics on the cavity operating parameters has been studied. Based on these results, the description of the cavity, that is necessary to choose the operating beam synchronous RF phase and the operating E_0 value, has been completed.

The longitudinal beam dynamics in the 6-cell cavity have been studied by particle tracking simulations. The simulations have been carried out in the ASTRA code [41], which allows to track the charged particle beams through the imported external electromagnetic fields. It is necessary to mention that the space charge effect [8] is not taken into account in the beam dynamics simulations due to the low beam current in the S-DALINAC. The electromagnetic field distribution of the accelerating mode has been obtained and discussed in Chapter 4.

It is worth noting that the beam dynamics simulations described in this chapter have been implemented and carried out during the considerations for choosing the cavity type and, further on, for choosing the optimal number of cells and the optimal β_g value evaluation for the reduced-β cavity. Hence, the organisation of the results in three separate chapters is somewhat artificial because the design of the cavity is in reality a highly iterative process.

5.1 Simulation Model and Initial Parameters

In this section, the simulation model that have been implemented for the longitudinal beam dynamics studies in the 6-cell cavity, is discussed. The particle tracking simulation model consists of a single electron bunch that interacts with the electromagnetic field of the accelerating mode of the 6-cell cavity. The beam at the entrance of the S-DALINAC capture section is formed by the beam preparation system that is installed prior the capture section. Due to the fact that the experimentally measured beam distribution at the entrance of the capture section is not available up to date, the initial Gaussian particle beam distribution has been generated in the ASTRA code and used as the initial beam configuration for beam dynamics simulations of the 6-cell cavity. The electron bunch parameters have been set based on the existing beam dynamics simulations data for the S-DALINAC beam preparation section.

Figure 5.1 illustrates the longitudinal phase space of the 200 keV bunch that consists of 150000 particles. A similar particle beam distribution has been generated for the 250 keV beam.

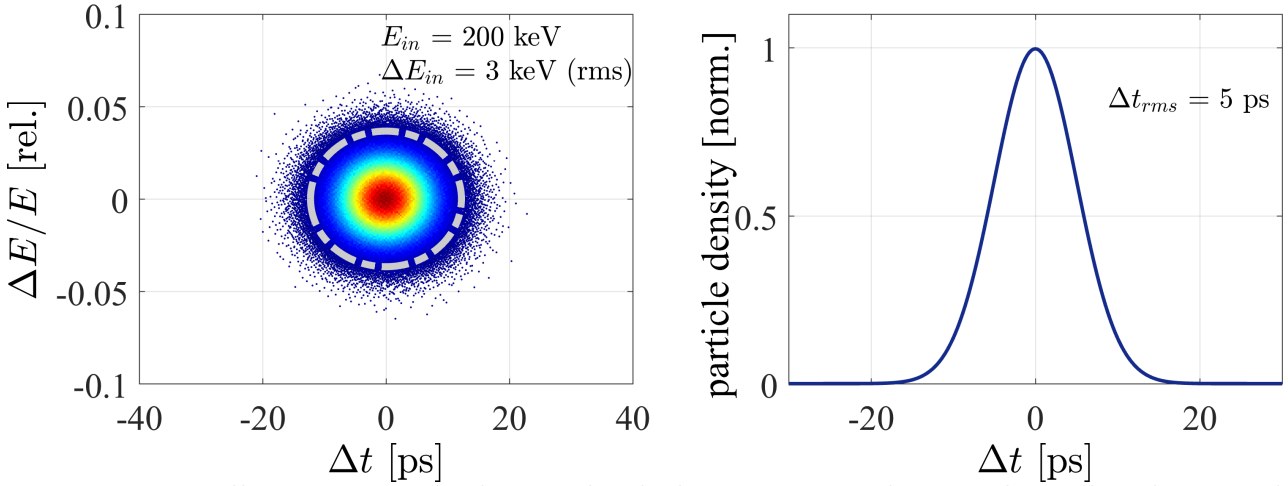

Figure 5.1: Left: illustration of the longitudinal phase space of the initial 200 keV beam. The area enclosed by the grey dashed-line ellipsoid contains 95% of particles. Right: illustration of the particle density in the initial beam with indicated rms bunch length.

5.2 Beam Dynamics Simulation Results

5.2.1 Beam Energy Gain

First, the beam energy gain in the 6-cell cavity has been studied. Figure 5.2 illustrates the beam energy gain as a function of the longitudinal coordinate of the 6-cell cavity. These results have been obtained in the particle tracking simulations of the 200 keV (SPG) and the 250 keV beam (TG). The 6-cell cavity peak electric field on axis E_0 has been set to a value of 10 MV/m. The initial RF phase of the cavity has been chosen in a way such that the longitudinal energy spread of the beam is minimised.

The obtained values for the beam output energy exceed the required beam output energy by 430 keV for the 200 keV beam and by 513 keV for the 250 keV beam. In addition, the obtained beam output energy for the 200 keV beam is 875 keV higher in comparison to the performance of the current setup of the capture section for the same value of E_0 of 10 MV/m. Further on, when analysing the curves for the beam energy gain, an energy loss of 70 keV and 56 keV can be observed in the region of $z \approx 0.14$ m for the 200 keV and 250 keV beam, respectively. These losses arise due to the presence of an de-accelerating electric field with notable amplitude at the end of the left beam tube of the cavity. This is explained by the large iris radius of the left end-cell of the cavity. The same effect can be observed at the beginning of the cavity right beam tube due to the same reason, however, the energy loss is lower due to a higher beam velocity at the end of the cavity.

Analysing the data and, by taking into account the low beam current at the S-DALINAC, the energy loss effect is negligible in terms of the overall cavity acceleration performance. Nevertheless, in order to compensate the energy loss effect in the cavity beam tubes, the cavity end-cells iris radius should be decreased in a way, such that the electric field propagates to the beam tubes with minimised peak amplitudes on the central axis. However, the 6-cell cavity iris radius is fixed for reasons of mechanical stability. Hence, the en-

ergy loss in the first and the last cell of the 6-cell cavity can not be corrected due to the restrictions imposed by the requirements for the capture section upgrade.

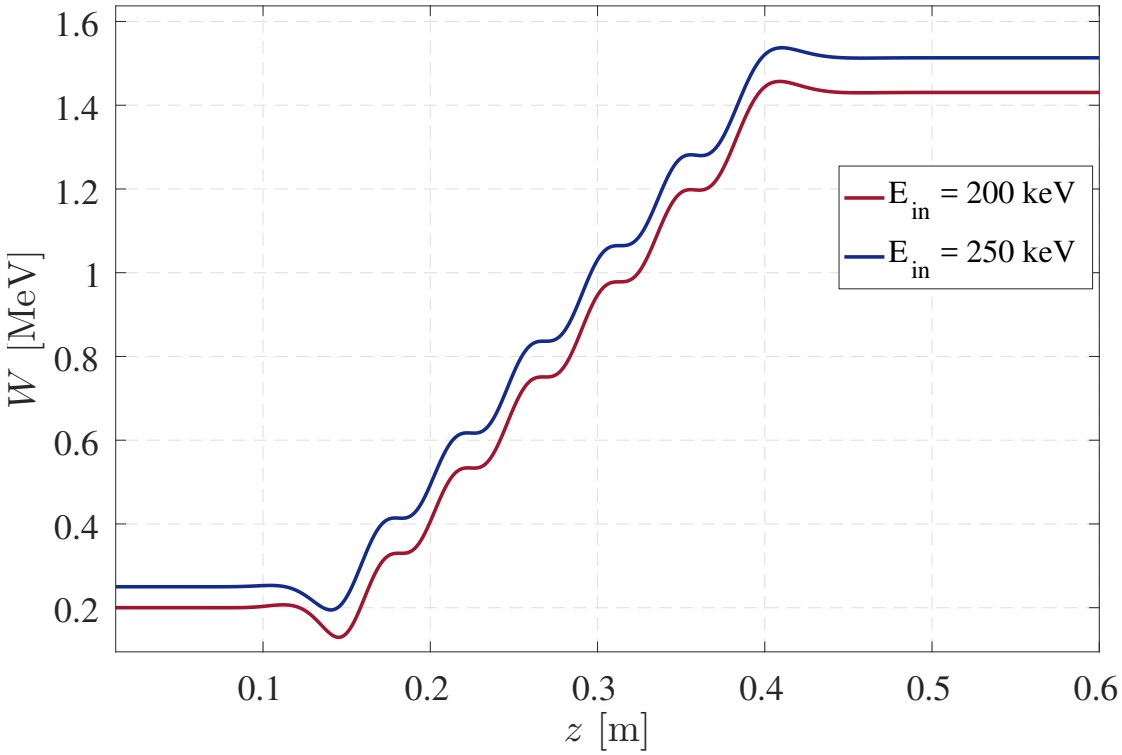

Figure 5.2: Illustration of the energy gain of the 200 keV and 250 keV electron beam in the 6-cell $\beta_g = 0.86$ cavity.

5.2.2 Longitudinal Energy Spread of the Beam

The longitudinal energy spread growth of the beam that arise when the beam interacts with the electric field of the accelerating mode of the 6-cell cavity, has been investigated in particle tracking simulations. The cavity RF phase and the peak electric field amplitude E_0 are the same as in the energy gain simulation. The computed relative longitudinal energy spread growth of the beam during the acceleration in the 6-cell cavity is illustrated in Fig 5.3. Analysing the data, the relative longitudinal energy spread growth of the beam is reduced by $1 \cdot 10^{-2}$ and $7.6 \cdot 10^{-3}$ for the 200 keV and 250 keV beam, respectively.

With respect to the obtained data and by taking into account the energy loss of the beam that was discussed in the previous section, the largest longitudinal energy spread growth arises in the region of the connection of the left beam tube to the first cell of the 6-cell cavity.

In order to get a better understanding of the longitudinal beam dynamics in the 6-cell cavity, six beam monitors have been introduced to the simulation model for the 200 keV beam. These beam monitors have been allocated after each cavity cell equidistantly from each other and their longitudinal positions correspond to the cavity regions with the electric field being almost absent. By doing so, it is possible to assess the impact of the electric field of each cell individually on the beam quality. As a result, six snapshots

of the beam longitudinal phase space have been obtained in the particle tracking simulation. The longitudinal phase space with the indicated average kinetic energy and the rms longitudinal energy spread value after each cavity cell are illustrated in Fig. 5.4. The beam longitudinal rms energy spread growth in the first cell amounting to ΔE_1 - ΔE_{in} = 3.9 keV is being corrected down to 1.9 keV in the second cell. Further on, in the following four cells, the rms energy spread growth value fluctuates in the range of (2.5 ± 0.6) keV and results in an output beam rms longitudinal energy spread growth of 3 keV. It is worth noting that a so-called beam tail can be observed in the output longitudinal phase space. However, the tail is located outside the 95% particle distribution (the area enclosed by the grey dashed-line ellipsoid). Therefore, the charge concentration in the observed beam tale is relatively low and its effect is negligible.

The presence of a rms longitudinal energy spread growth in the 6-cell β_g = 0.86 cavity is explained by the constant length of the cavity accelerating cells. Hence, a further reduction of the beam rms energy spread growth in the capture section does not seem feasible with respect to the specified requirements for the upgrade. Nevertheless, the beam rms longitudinal energy spread value obtained in the 6-cell cavity is almost 8 times lower in comparison to the value of 23 keV that is observed in the current setup of the S-DALINAC capture section.

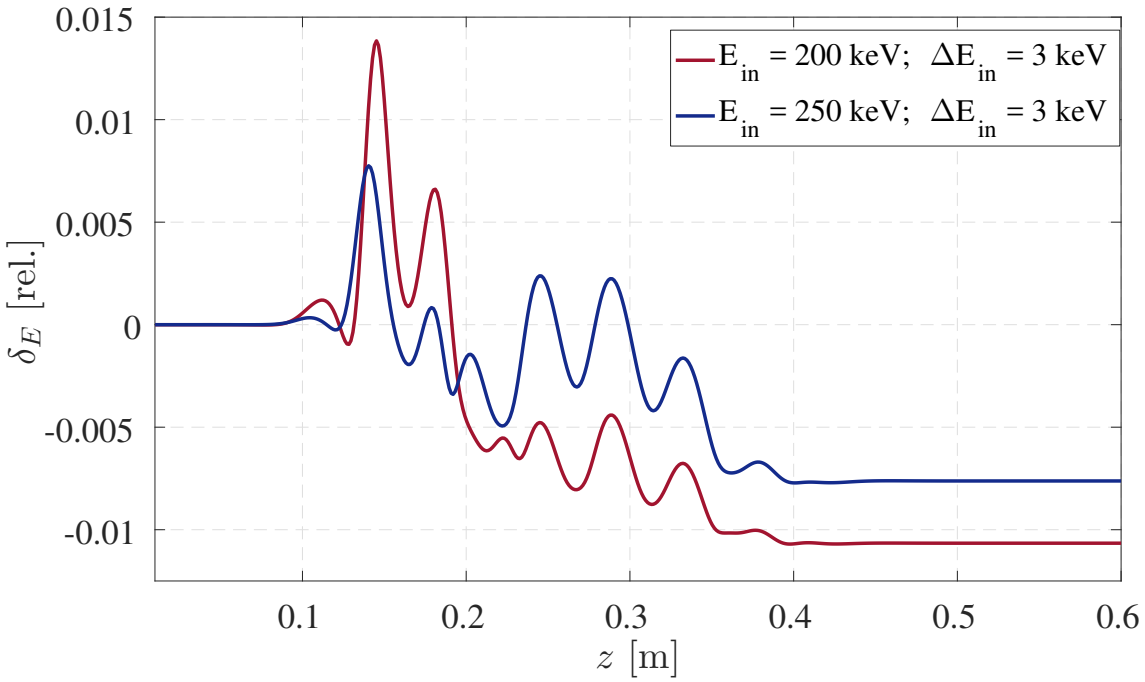

Figure 5.3: Illustration of the relative longitudinal energy spread growth of the 200 keV and 250 keV electron beam in the 6-cell cavity.

5.2.3 Initial RF phase and Field Amplitude Choice

The beam output energy and its longitudinal energy spread depend on the amplitude and the RF phase of the cavity accelerating field in operation. In case of the acceleration of

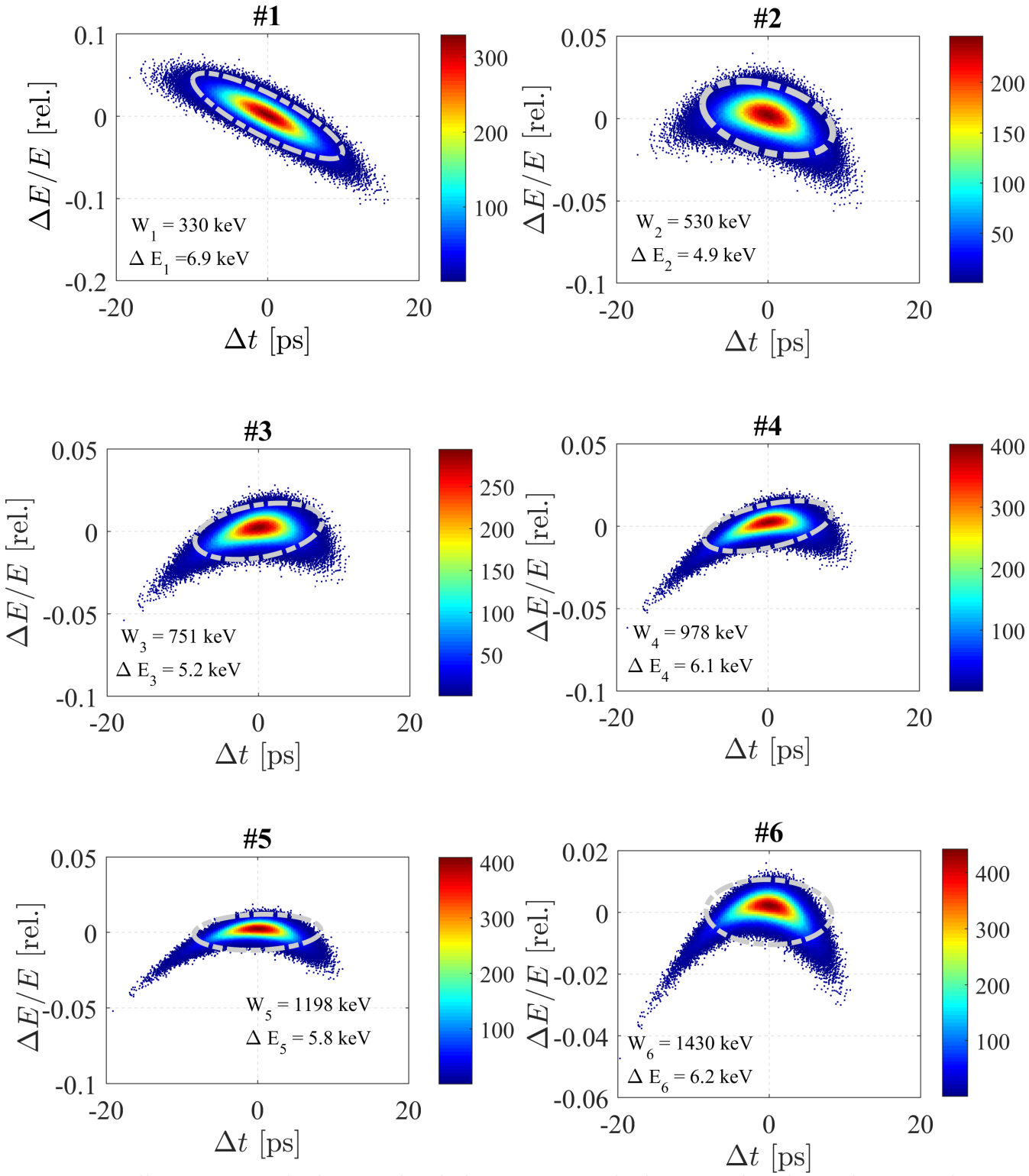

Figure 5.4: Illustration of the longitudinal phase space of the beam with indicated average kinetic beam energy and rms longitudinal beam energy spread value after acceleration in each cavity cell. The colormap on the right hand-side of each diagram shows the number of particles in one bin depending on the colour e.g, dark red colour represents the highest particle density in the phase space. The area enclosed by the grey dashed-line ellipsoid contains 95% of particles. The results are valid for an input beam energy of 200 keV, an input beam longitudinal rms energy spread of 3 keV and an rms bunch length of $\Delta t = 5$ ps.

the beam, velocities of which remain almost constant[1] during acceleration in an RF cavity, it is possible to choose either field the off-crest acceleration to correct the beam energy spread or the on-crest regime for the maximum possible energy gain at which the energy spread can not be corrected. In case of the 6-cell cavity, the beam relative velocities vary from 0.7 to 0.97 during the acceleration while the length of the accelerating gaps remains constant. Because of this, the synchronous RF phase is not the same in each cell. Hence, it is not possible to choose a specific acceleration regime (e.g. off-crest acceleration) for the 6-cell cavity.

A minimised beam energy spread is one of the important requirements for the 6-cell cavity. In that regard, it is necessary to determine the cavity RF phase, which corresponds to the minimum energy spread while the necessary energy gain is reached. In addition, it is necessary to reveal the dependence of the output energy of the beam as a function of the amplitude of the accelerating field on the axis of the structure with the cavity initial RF phase that corresponds to the minimum possible energy spread of the beam.

It is necessary to mention that the initial RF phase values ϕ_{RF_0} that are indicated in this chapter are not calibrated for the S-DALINAC operation. Instead, the values are given with the intend to demonstrate the 6-cell cavity phase range $\Delta\phi_{\mathrm{RF}_0}$ at which the specific beam characteristics can be obtained.

RF Phase

Figure 5.5 illustrate the computed beam output energy as a function of the initial RF phase of the cavity. The results have been obtained for an E_0 value of 10 MV/m. The initial RF phase of the cavity ϕ_{RF_0} corresponds to the time $t = t_1$ at which the particle tracking of the initial beam starts. The 200 keV beam reaches a maximum output energy $W_{\mathrm{out.max.}}$ of 1.432 MeV at the cavity initial RF phase ϕ_{RF_0} of:

$$\phi_{\mathrm{RF}_0}\Big|_{W_{\mathrm{out}}=W_{\mathrm{out.max.}}} = \phi_{\mathrm{W}_{\mathrm{out.max.}}} = -1.5 \text{ [deg.]}. \tag{5.1}$$

The 200 keV beam output energy varies in the range (5.2) for the phase range (5.3).

$$W_{\mathrm{out}} = (W_{\mathrm{out.max.}} \pm 2) \text{ [keV]}. \tag{5.2}$$

$$\phi_{\mathrm{RF}_0} = (\phi_{\mathrm{W}_{\mathrm{out.max.}}} \pm 5) \text{ [deg.]}. \tag{5.3}$$

As can be seen from in Fig. 5.6, the minimal rms energy spread of the output beam is observed for an cavity initial RF phase of

$$\phi_{\mathrm{RF}_0} = \phi_{\mathrm{W}_{\mathrm{out.max.}}} - 5.1^\circ = -6.6 \text{ [deg.]}. \tag{5.4}$$

Analysing the data, it is possible to distinguish two possible operational regimes of the 6-cell cavity depending on the chosen value of the RF phase. The first regime corresponds to a maximised output beam energy and a noticeably increased longitudinal rms energy

[1] For example, a relativistic electron or proton beam.

spread. The second regime is characterised by an insignificantly decreased output beam energy and a minimised longitudinal energy spread. In the second regime, the beam output energy decreases by less then 1% in comparison to the beam output energy in the first regime. Thus, the second regime is preferred due to obvious reasons.

Overall, the simulation results for the 6-cell cavity have indicated the wide phase range available for operation. The data obtained for the 250 keV beam allows to carry out similar estimations and analysis. Its is worth noting that in case of the 250 keV beam the cavity RF phase range at which the longitudinal energy spread of the output beam is minimised is narrower in comparison to the results that have been obtained for the 200 keV beam. This is explained by the fact that the 6-cell cavity has been developed with the intend to have optimal performance for acceleration of the 200 keV beam that is injected from the SPG. Nevertheless, for the acceleration of the 250 keV beam, the cavity RF phase region of stability is within a reasonable range and the output beam rms longitudinal energy spread is larger by only 0.5 keV in comparison for the 200 keV beam with higher output energy at the same time.

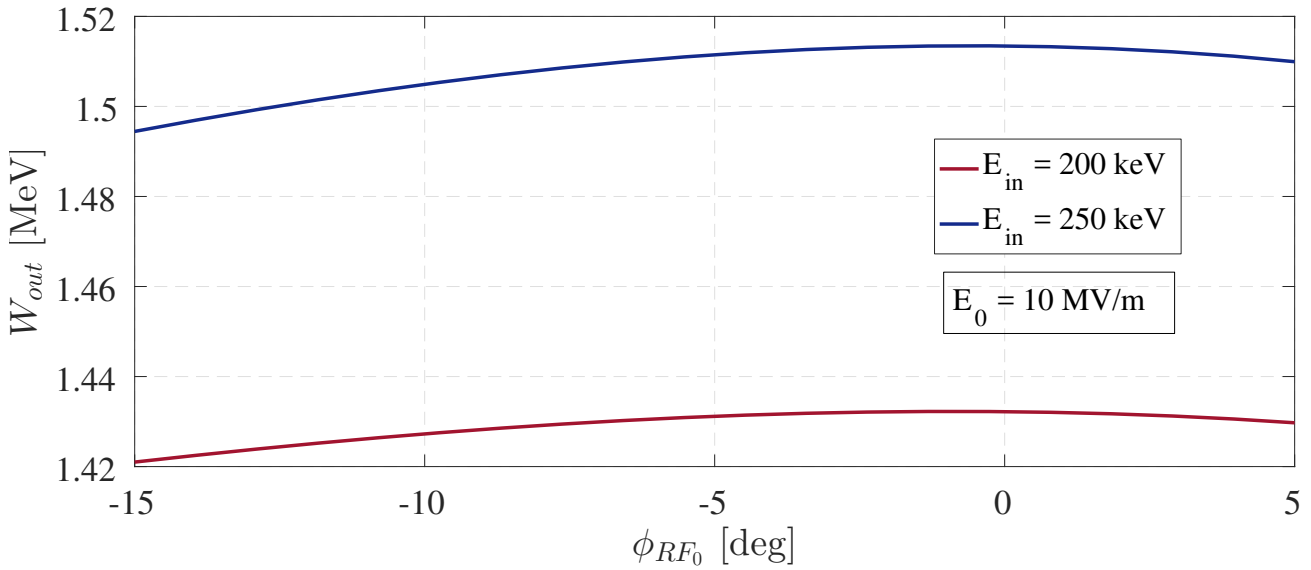

Figure 5.5: Dependence of the output beam energy on the choice of the cavity initial RF phase with indicated input parameters.

Accelerating Field Amplitude

Similarly to the previous section, simulation results are explained for the 200 keV beam, while the same analysis can be easily carried out for the 250 keV beam based on the presented data.

The 6-cell cavity is planned to be operated with a peak electric field on the cavity central axis E_0 of 10 MV/m. During the operation various limitations and changes to the accelerator operating parameters can take place. Due to that, the cavity can be operated at field amplitudes larger or smaller than the designed value. In that regard, the output beam characteristics have been studied for various peak amplitudes of the electric field on the 6-cell cavity axis.

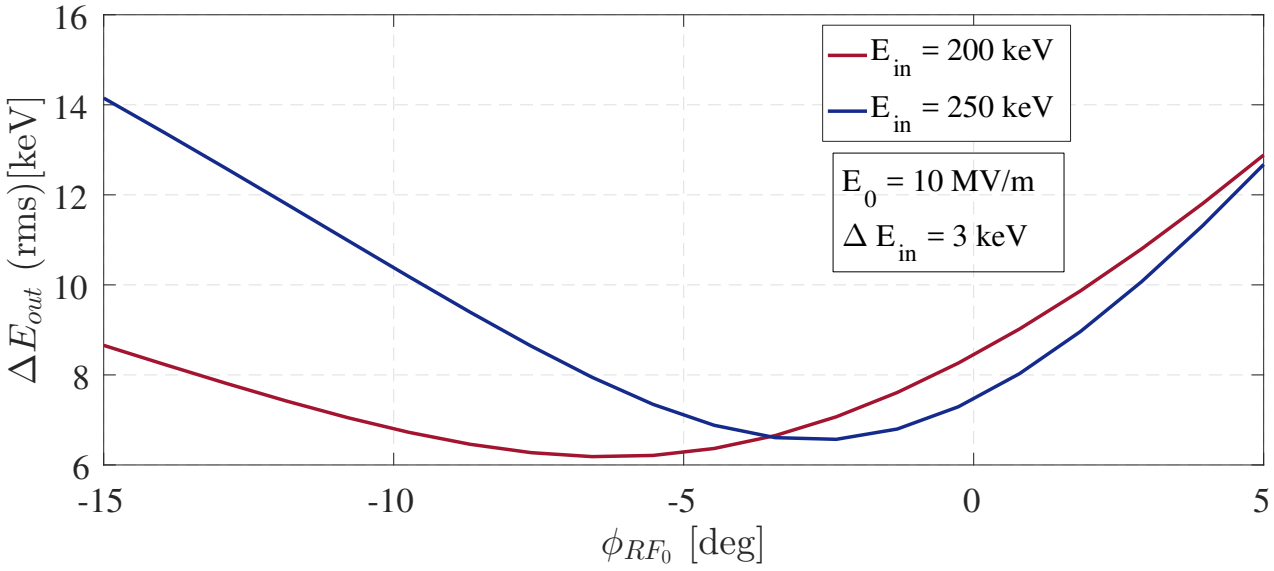

Figure 5.6: Dependence of the output beam rms longitudinal energy on the choice of the cavity initial RF phase with indicated input parameters.

The required minimum output energy of the beam of 1 MeV is achieved at a E_0 value of 7 MV/m , as can be seen from Fig 5.7. When the designed value of E_0 is doubled, the beam energy gain is $\Delta W = W_{\text{out}} - W_{\text{in}} = 2.4$ MeV, which is two times larger than the beam output energy of $\Delta W = 1.2$ MeV obtained with a value E_0 of 10 MV/m. Hence, the dependence of the beam output energy on the field amplitude is almost linear in the range of 10 MV/m $\leq E_0 \leq$ 20 MV/m. From Fig. 5.8, one can see that the minimum energy spread is observed at a field amplitude E_0 of 8 MV/m.

Analysing the data, it is possible to operate the cavity within a fairly wide field amplitude range. This indicates an optimally chosen value of β_g and of the number of cells for the 6-cell cavity. From the point of view of minimising the energy spread of the beam, the 7 MV/m $\leq E_0 \leq$ 10 MV/m range is preferred. It is worth noting that the beam energy spread increases with the increase of the electric field amplitude on the axis, due to the constant length of the cavity cells.

5.3 Conclusion

Beam dynamics computations have been performed for the 6-cell cavity. The data obtained for a value E_0 of 10 MV/m indicated that for the 200 keV and the 250 keV beam the required beam output energy of 1 MeV is exceeded by 430 keV and 513 keV, respectively. In addition, the cavity can be operated in a wide range of E_0 values of up to 20 MV/m. It should be noted that an increase of the longitudinal rms energy spread of the output beam is observed when $E_0 >$ 10 MV/m.

The relative energy spread growth is reduced for both beams at $E_0 = 10$ MV/m. Additional beam dynamics simulations have been carried out for the 200 keV beam and its longitudinal phase space has been analysed. The obtained output beam longitudinal phase space has indicated the presence of a beam tail. However, the beam tail is located outside of 95% of the particles distribution and, hence, its effect is negligible because

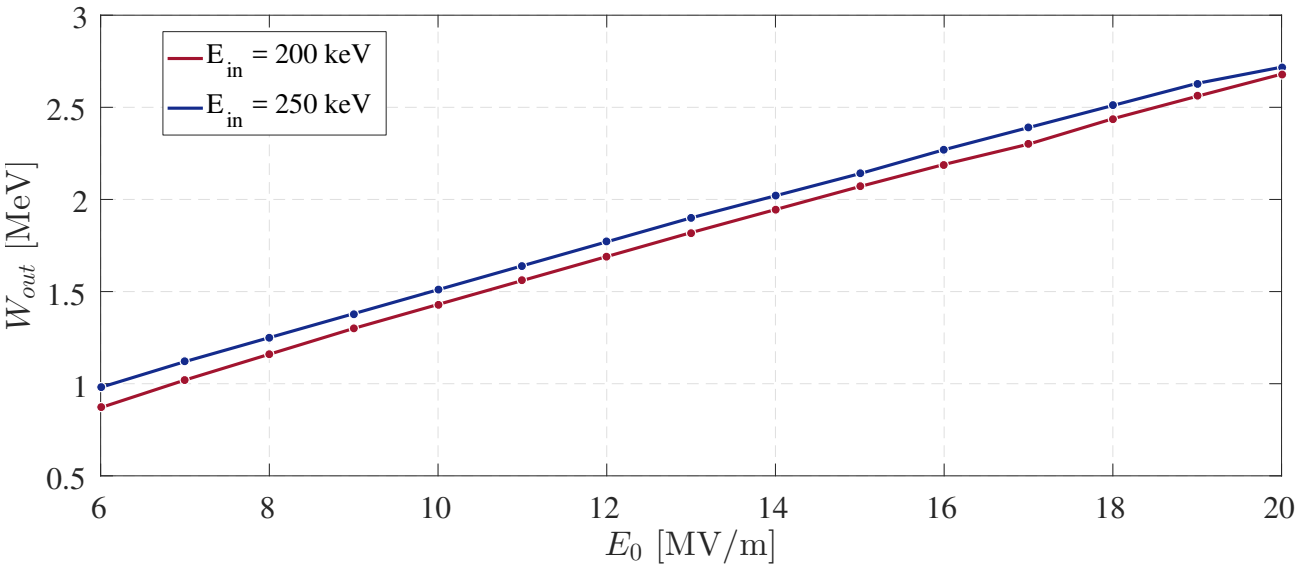

Figure 5.7: Dependence of the output beam energy on the choice of the cavity operating E_0 value. The results are valid for the ϕ_{RF_0} value at which the output beam energy spread is minimal.

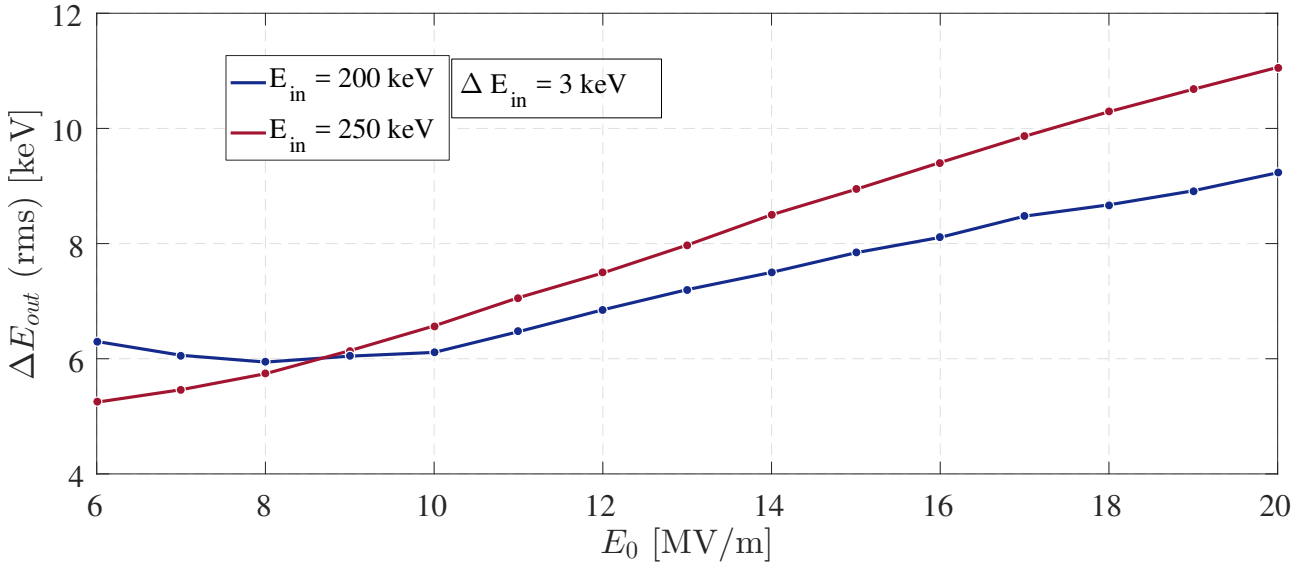

Figure 5.8: Dependence of the output beam rms longitudinal energy on the choice of the cavity operating E_0 value. The results are valid for the ϕ_{RF_0} value at which the output beam energy spread is minimal.

of the low charge concentration in it. The rms longitudinal energy spread of the beam grows by only 3 keV and 3.5 keV for the 200 keV and the 250 keV beam, respectively. Taking into account the fact that the cavity cell length is constant, the obtained values for the beam rms longitudinal energy spread are relatively low. Further minimisation of the rms energy spread growth is feasible by considering the other proposed cavity layouts, which would require a new capture section cryostat.

The 6-cell cavity can be operated in a wide range of accelerating field amplitudes of up to 10 MV/m and has a wide RF phase stability range of 10°. This is explained by the optimal number of the cavity cells and by the choice of the β_g value that has been discussed in Chapter 4.

6 Mechanical Stability of the 6-cell Cavity

The SRF cavity is mounted in a liquid helium cryostat where it is cooled down and operated at a temperature of 2-4 K. During operation, various mechanical loads act on the cavity walls. As a consequence, the EM field distribution of the cavity is perturbed. Due to that, the electromagnetic parameters of the cavity such as the accelerating mode resonance frequency and the field flatness deviate from the designed values. A mechanical tuner is installed in the cryostat in order to correct the resonance frequency of the cavity. In order to assess the mechanical stability of the 6-cell $\beta_g = 0.86$ cavity and in order to determine the mechanical characteristics of the cavity required for designing the cavity tuning, a structural analysis has been carried out in the ANSYS software [42].

After a short theoretical introduction the computed results are discussed. The presented theoretical introduction highlights only the information that is necessary in this framework. Detailed information related to mechanics of particle accelerators can be found in [43].

6.1 Introduction

The goal of this section is to briefly introduce the main sources of unwanted mechanical loads that act on the SRF cavity walls and to present the key analytic expressions that characterise the frequency detuning owe to perturbations of the cavity volume. In addition, the material properties that are required for the structural analysis of the metallic bodies, are introduced.

One of the sources of mechanical loads is the static pressure in the cryostat that acts on the cavity walls during cavity operation. For an elliptic cavity, a typical value of the shift of the resonance frequency is below 100 Hz, which can be compensated by the cavity tuning system.

Another source of external mechanical loads are mechanical vibrations of the cavity (microphonics). Microphonics arise when one of the vibration sources in the accelerator hall mechanically couples to the cavity and excites one of the resonance modes of the cavity structure. The microphonics sources can be ground motion, helium pressure fluctuations and pumping systems of the accelerator. The mechanical vibrations lead to geometric deformation of the cavity. It is challenging to compensate for field and phase detuning arising from the microphonics effect, due to its non-static behaviour. When it is not feasible to compensate the frequency detuning caused by microphonics, the strong overcoupling regime is introduced, which requires more generator power in comparison to operation at the cavity optimal Q_L value (See Chapter 4, Section 4.4.2).

The Lorentz force pressure that acts on the inside the walls of the cavity should also be mentioned as a source of cavity detuning. However, the impact of this effect is only relevant for cavities that are operated with high accelerating gradients in pulsed regime. More information regarding sources of cavity detuning can be found in [14] and [19].

The material properties of the cavity define the structure rigidity, along with the cavity geometry. In solid state mechanics, the Young modulus is a measure of the stiffness of the material, and is defined as:

$$Y_{\mathrm{m}} = \frac{\text{tensile stress}}{\text{tensile strain}} = \frac{F/A_0}{\delta L/L_0} = \frac{FL_0}{A_0 \Delta L} \tag{6.1}$$

where A_0 is the original cross-sectional area at which the force F is applied to the object, ΔL is the object length change and L_0 is the initial object length.

In addition to Young modulus, the second required figure of merit for the structural analysis of the cavity is the Poisson ratio. For compressable objects it is defined as:

$$\nu = -\frac{\text{transverse strain}}{\text{axial strain}} \tag{6.2}$$

Slater's Theorem

Slater perturbation theorem describes the dependence of the RF cavity resonance frequency on changes caused by mechanical perturbations to the magnetic and electric energies stored in the cavity. The dependence can be expressed as follows [10]:

$$\frac{\omega - \omega_0}{\omega_0} = \frac{1}{U}\left(\Delta U_{\mathrm{m}} - \Delta U_{\mathrm{e}}\right), \tag{6.3}$$

where ω and ω_0 are the perturbed and the unperturbed cavity angular resonance frequencies, respectively, U is the cavity unperturbed time-averaged stored energy, ΔU_{m} and ΔU_{e} are the time-averaged magnetic and electric stored energies removed as a consequence of the cavity perturbation.

A simple explanation of this phenomenon is given by referring to the LC analogy of the cavity. For that, imagine a single-cell elliptic cavity operated with the $\mathrm{TM}_{010};\pi$ mode, represented by a simple LC-circuit. In this case, the $\mathrm{TM}_{010};\pi$ mode resonance frequency ω_{010} is expressed as:

$$\omega_{010}^2 = \frac{1}{LC}, \tag{6.4}$$

where L is the cavity inductance and C is the cavity capacitance.

The introduction of an additional cavity volume in the cavity region of high electric field concentration (e.g. the cavity iris) will decrease the cavity capacitance C and increase the resonance frequency. The introduction of an additional volume in the cavity region with high magnetic field concentration (e.g. the cavity equator) will increase the inductance and decrease the resonance frequency.

6.2 Mechanical Model of the Cavity

The importance of a mechanical study prior cavity operation is motivated by two main factors: the stability of the cavity in operation and the tuning range of the cavity's resonance frequency in operation.

In the SRF engineering community, the longitudinal stiffness of the cavity k is a commonly used figure of merit for indicating the cavity's rigidity. Typical k values that have been reported to be reliable in operation are in the range of 3 kN/mm up to 10 kN/mm depending on the SRF cavity type and the used resonance frequency (transverse dimensions). Thus, by knowing the reliable range of the longitudinal SRF elliptic cavity stiffness it is possible to assess the rigidity of the 6-cell $\beta_g = 0.86$ cavity based on the results of a structural analysis and by referring to the data and operational experience that have been reported for similar cavities. The logic behind the cavity rigidity assessment is the following: a very low longitudinal stiffness of the cavity indicates that the cavity will be very sensitive to mechanical deformations and a compensation of the resonance frequency detuning can not be guaranteed in operation. On the other hand, a very high longitudinal stiffness of the cavity can lead to a situation where the cavity frequency detuning can not be compensated for, due to the insufficient force provided by the cavity tuning system. The solution for these problems can be either a modification of the cavity geometry or a modification of the cavity tuning system.

In addition to the longitudinal stiffness of the cavity, the dependence of the resonance frequency on the cavity length is required in order to complete the mechanical specification that is required as input for the design of the cavity tuning system. Furthermore, it is necessary to investigate the sensitivity of the accelerating mode resonance frequency to the outside static pressure that acts on the outside surface of the cavity walls. By knowing the average helium pressure fluctuations in the current setup of the capture section, the expected resonance frequency detuning of the 6-cell cavity due to the static helium pressure can be estimated.

6.2.1 Simulation Model

Prior to discussing the results of the mechanical simulations of the 6-cell cavity, it is necessary to describe the cavity model and to introduce the boundary conditions that have been implemented for the structural analysis of the cavity. The cavity model is the same in all mechanical simulations and, due to the cavity axial symmetry, consists of $\alpha = 18^\circ$ of the full cavity model, as can be seen in Fig. 6.1. Similarly to the cavity RF design, some model simplifications allow to reduce the computation time while making sure that the solutions converge with respect to the spatial resolution of the computational mesh. It is worth noting that a 2-D mechanical analysis of the cavity is a state-of-the-art technique. However, for the computation of the change of the accelerating mode frequency, caused by mechanical loads, it is necessary to apply 3-D simulation in ANSYS. The sensitivity of the cavity resonance frequency has been estimated using the following algorithm:

1. The resonance frequency of the unperturbed 6-cell cavity $TM_{010};\pi$-mode is computed by an EM simulation (see Chapter 4).

2. The mechanical load is applied to a 3-D model of the 6-cell cavity body to obtain the cavity deformation.

3. The deformed mesh (see Fig.6.2) from (2) is given back to the EM solver (1).

4. The resonance frequency of the $TM_{010};\pi$-mode is computed in the EM simulation with respect to the deformation obtained in (2).

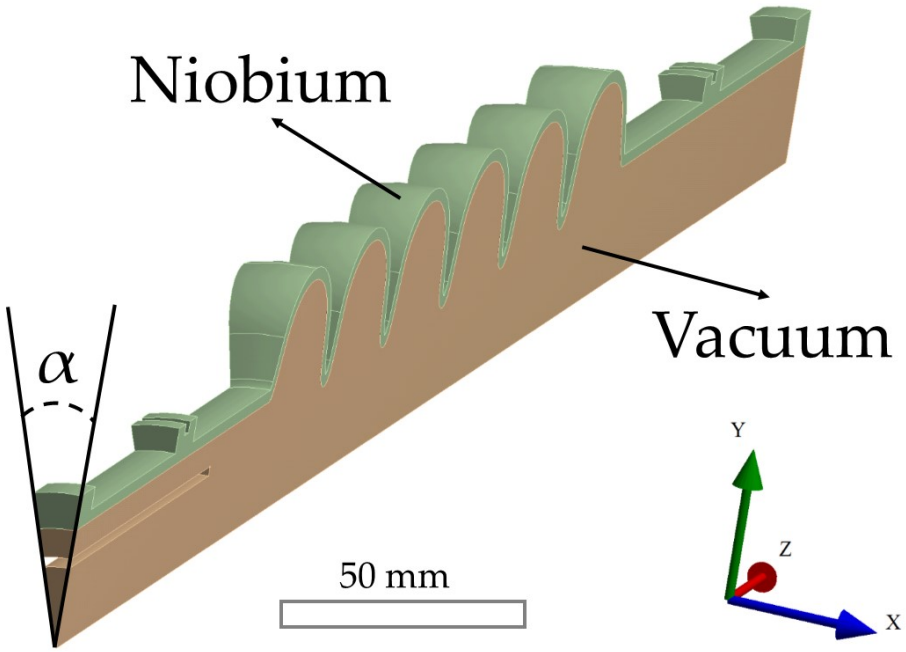

Figure 6.1: 3-D CAD model of the 6-cell cavity that has been used in the structural analysis and in the EM simulations. The model consists of pie piece of only $\alpha = 18°$ from the cavity total axial volume (360°)

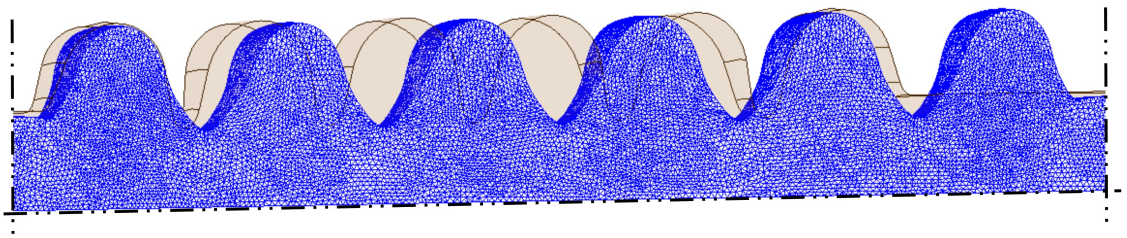

Figure 6.2: Partial illustration of the deformed mesh of the 6-cell cavity due to a 1 bar outside pressure applied to the cavity outside surface. The scale of the deformation is exaggerated for an improved visualisation. The unperturbed shape of the cavity is shown in a transparent brown colour.

For each computed mechanical parameter of the cavity, different mechanical loads have been introduced to the cavity simulation model. The boundary conditions have been defined in regions where the cavity is fixed to the cavity tuner holder (see Fig. 6.3 (A) and (B) region). The boundary conditions and mechanical loads that have been introduced

for the computations of the mechanical characteristics of the cavity are collected in Table 6.1. The mechanical properties of Niobium are characterised by a Young modulus Y_m = 118 GPa and a Poisson ratio $\nu = 0.38$ at an operating temperature of 2 K and a cavity wall thickness of 2.65 mm.

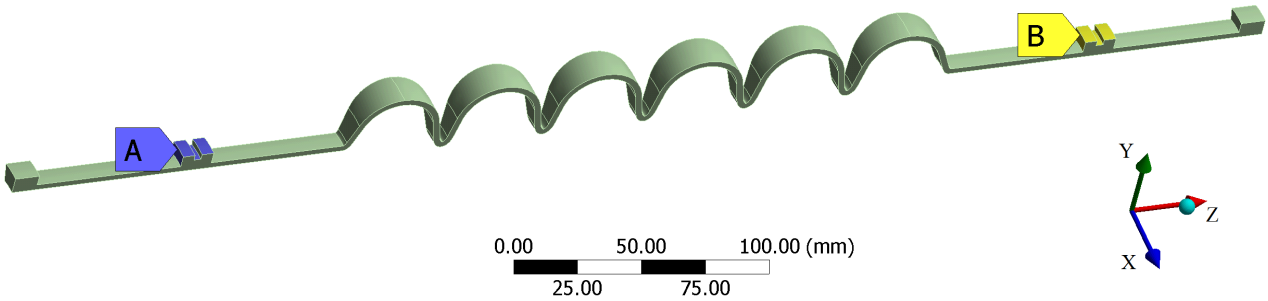

Figure 6.3: 3-D simulation model for the structural analysis of the 6-cell cavity with indicated regions at which the boundary conditions are defined (A and B surface).

Computed parameter	Applied load	A region	B region
k, kN/mm	1 kN axial force	fix.	(fix.,fix., fr.)
df/dl, kHz/um	1 mm axial displacement	fix.	(fix.,fix., fr.)
df/dp, Hz/mbar	1 bar outside pressure	fix.	(fix.,fix., fr.)
Vibration resonance frequencies	mechanical excitation	fix.	(fix.,fix., fr.)

Table 6.1: Boundary conditions and applied loads that have been introduced to compute the cavity mechanical parameters.

6.2.2 Mechanical Characteristics of the Cavity

The computed value of the longitudinal stiffness of the 6-cell β_g=0.86 cavity is:

$$k = 5.2 \, \frac{\text{kN}}{\text{mm}}. \tag{6.5}$$

The obtained k value indicates that the 6-cell cavity is rigid enough without further geometry optimisation, and that an implementation of cavity stiffening rings is not required. This conclusion has been made based on the data reported for the 3.9 GHz TESLA cavity [44]. It is worth noting, that the 6-cell cavity mechanical optimisation has been carried out for one of the first proposed layouts of the 6-cell reduced-β cavity, in which the end-cell iris radius was set the same as the mid-cell iris radius. The cavity structural analysis indicated that the non-smooth transition between the end-cells and the beam tubes decreases the 6-cell cavity's longitudinal stiffness by 1 kN/mm. The cavity layout with a lower iris radius is characterised by a higher *R-over-Q value*, however, the change of the mechanical stability of the cavity has a higher priority in this framework.

The sensitivity of the resonance frequency of the 6-cell cavity to the change of the longitudinal length is:

$$\frac{\mathrm{d}f}{\mathrm{d}l} = 2.1\ \frac{\mathrm{kHz}}{\mu\mathrm{m}}. \tag{6.6}$$

The obtained values for k and $\mathrm{d}f/\mathrm{d}l$ allow to easily estimate the required tuner step and the sensitivity of the frequency to the force F applied in the longitudinal direction:

$$\frac{\mathrm{d}f}{\mathrm{d}F} = 404\ \frac{\mathrm{kHz}}{\mathrm{kN}}. \tag{6.7}$$

As an example, the deformation of the cavity due to an applied longitudinal force of 1 kN to the cavity is illustrated in Fig. 6.4.

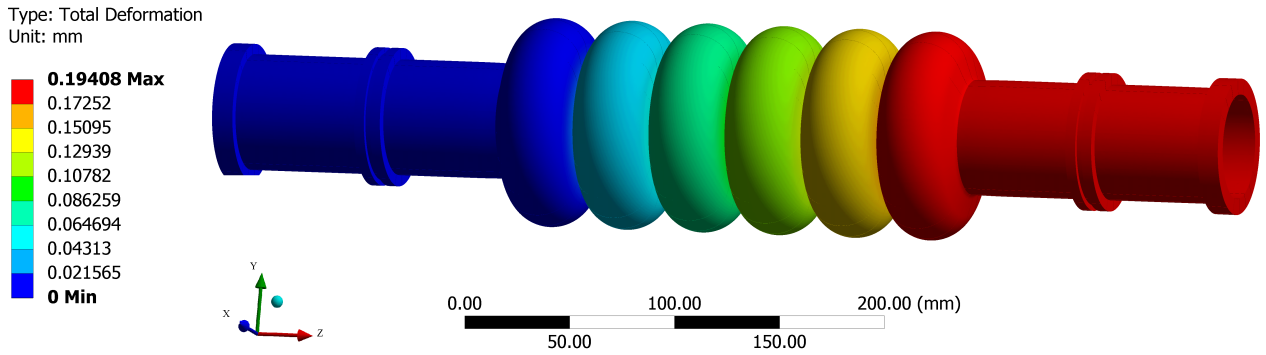

Figure 6.4: Illustration of the deformation of the 6-cell cavity caused by an axial force of 1 kN.

Further on, the computation of the sensitivity of the accelerating mode frequency on the outside pressure indicated the value of:

$$\frac{\mathrm{d}f}{\mathrm{d}p} = 26\ \frac{\mathrm{Hz}}{\mathrm{mbar}} \tag{6.8}$$

The expected average pressure acting on the outside surface of the cavity in the cryostat during operation is 1.5 mbar. Hence, in absence of uncontrollable pressure fluctuations, the cavity's average resonance frequency detuning caused by the helium pressure fluctuations in the cryostat is 39 Hz and can be compensated by the tuning system of the cavity during operation.

6.2.3 Microphonics

6-cell cavity microphonics simulations have been carried out with the aim to search for potential resonance modes of the cavity. In addition, there are microphonics measurements planned at the S-DALINAC facility. Thus, the sources and frequencies of vibrations in the accelerator hall can be determined and isolated from the 6-cell cavity.

There are two longitudinal mechanical vibration modes of the 6-cell cavity in the frequency range below 1 kHz, as can be seen in Table 6.2. The data and especially the resonance frequencies of the longitudinal modes must be taken into account when analysing

Mode number N	Mode type	Resonance frequency, Hz
1	longitudinal	288
2	transverse	385
3	transverse	796
4	longitudinal	921
5	transverse	1200
6	breathing	1341
7	transverse	1573
8	longitudinal	1613
9	transverse	1876
10	longitudinal	2304

Table 6.2: Resonance frequencies of the first ten mechanical vibration modes of the 6-cell cavity.

mechanical vibration sources at the S-DALINAC accelerator hall. The 6-cell cavity deformation maps of the first four mechanical vibration modes are illustrated in Fig. 6.5 with exaggerated amplitude.

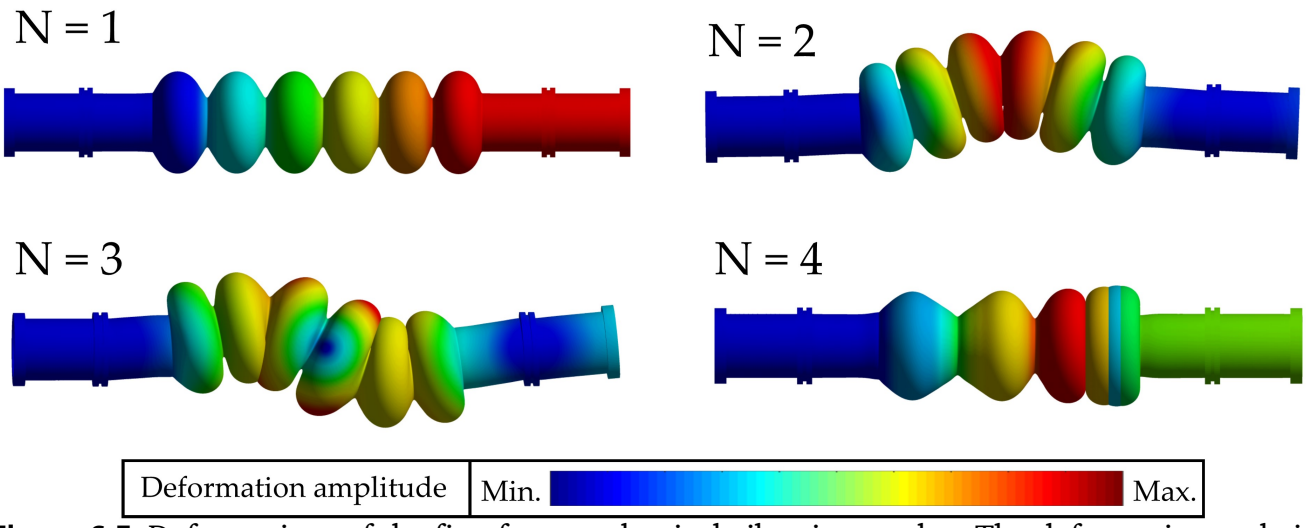

Figure 6.5: Deformations of the first four mechanical vibration modes. The deformation scale is exaggerated for an improved visualisation.

6.2.4 Mechanical Tuner of the Cavity

For tuning the 6-cell cavity, the tuner setup existing at the S-DALINAC is kept. This system has been modeled and modified by S. Weih (IKP, TU Darmstadt) such that the possibility of tuning the 6-cell cavity in operation is enabled. The existing tuning system has been previously implemented for the tuning of the 5-cell cavity. The 6-cell cavity has been designed in a way such that its dimensions fit into the existing SRF cavity tuner with minimised modifications to the tuner geometry. The tuner operation principle is

introduced shortly. For more details regarding the principle of operation the reader is referred to the work of S. Weih published in [45].

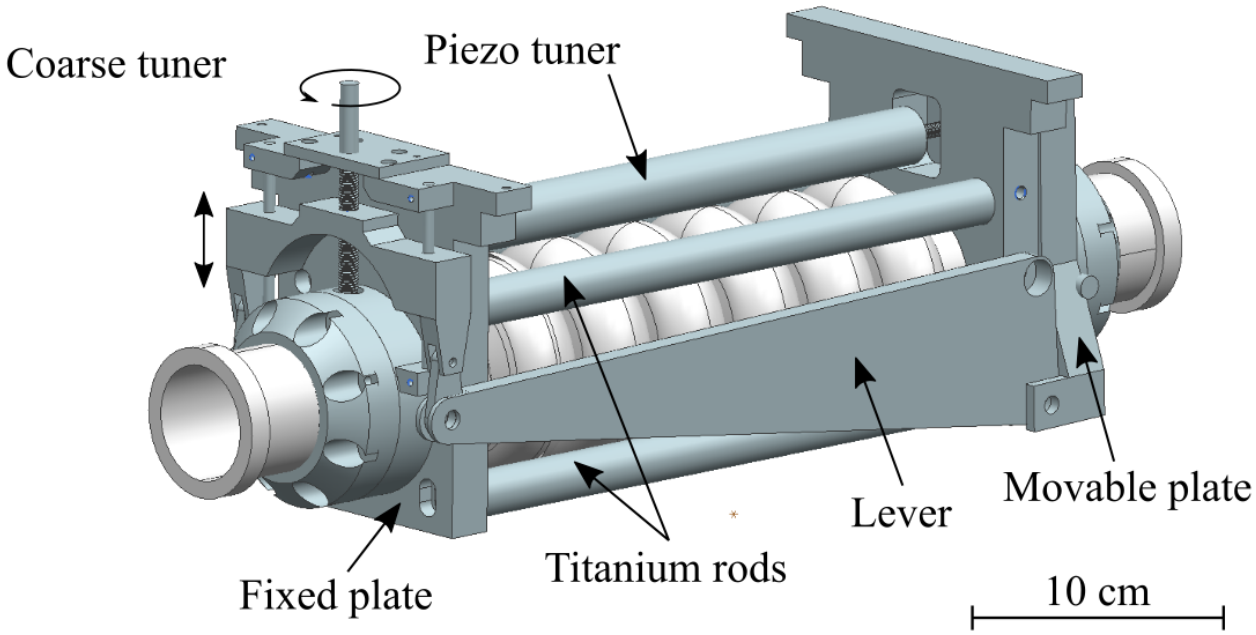

Figure 6.6: 6-cell cavity equipped with the tuner frame.

As can be seen from Fig. 6.6, the tuner is designed as a lever system where the force is applied by a stepper motor (coarse tuner). In addition, piezoelectric tuners are installed for the fast frequency tuning. One fixed plate and another movable plate are connected by four titanium rods. The cavity's holders are fixed on these plates. Hence, by driving the tuners it is possible to either stretch or compress the cavity depending on the required resonance frequency change of the cavity's accelerating mode. After the cavity is cooled down to the operating temperature of 2 K, the cavity body slightly shrinks, thus the resonance frequency changes as well. This resonance frequency change is compensated by the slow coarse tuner. Further on, the S-DALINAC LLRF field control system maintains the cavity accelerating mode with a relative field amplitude error of $7 \cdot 10^{-5}$ and rms phase error of 0.8° [46]. The existing tuner setup successfully covers the required tuning range for the 6-cell $\beta_g = 0.86$ cavity with the indicated mechanical parameters.

6.3 Conclusion

A structural analysis has been carried out and the main mechanical characteristics have been computed for the 6-cell cavity. The obtained data for the constant wall thickness of 2.65 mm allows to assess the cavity's rigidity. The longitudinal stiffness of $k = 5.2$ kN/mm indicates that the cavity is rigid enough and an implementation of cavity stiffening rings is not required. The sensitivity of the resonance frequency of the cavity to the applied force is 404 kHz/kN. This value together with the obtained value for k is sufficient to evaluate the necessary cavity tuner properties.

The sensitivity of the resonance frequency of the cavity to the pressure acting on the cavity's outside surface is below 100 Hz/mbar. The expected average helium pressure fluctuations in the cavity cryostat is 1.5 mbar. The obtained average frequency detuning of 39 Hz can be compensated by the S-DALINAC tuning system.

It is worth noting that the company appointed for manufacturing the cavity will introduce modifications to the cavity's outside geometry by reducing the cavity wall thickness in the cavity welding regions due to requirements related to the electron beam welding (EBW) procedure. Due to the fact that the details of these modifications are not available up to date, an additional computation of the longitudinal cavity stiffness has been carried out based on data available in literature. Preliminary estimations of the impact of the modifications to the cavity's outside shape predict a maximal cavity stiffness decrease by 1 kN/mm leading to a longitudinal stiffness of 4.2 kN/mm, which is still within a reliable range.

The final 6-cell cavity mechanical drawings that have been used for ordering the cavity are shown in Fig. 6.7. These drawings represent the 6-cell cavity in the cold state with a wall thickness of 2.65 mm. It is worth noting that the 6-cell cavity will be manufactured with a wall thickness of 2.8 mm. Further on, the cavity's inside surface will be post processed by chemical polishing (BCP) to eliminate inside surface defects. In that regard, 150 μm of the wall thickness will be removed, resulting to a final wall thickness of 2.65 mm.

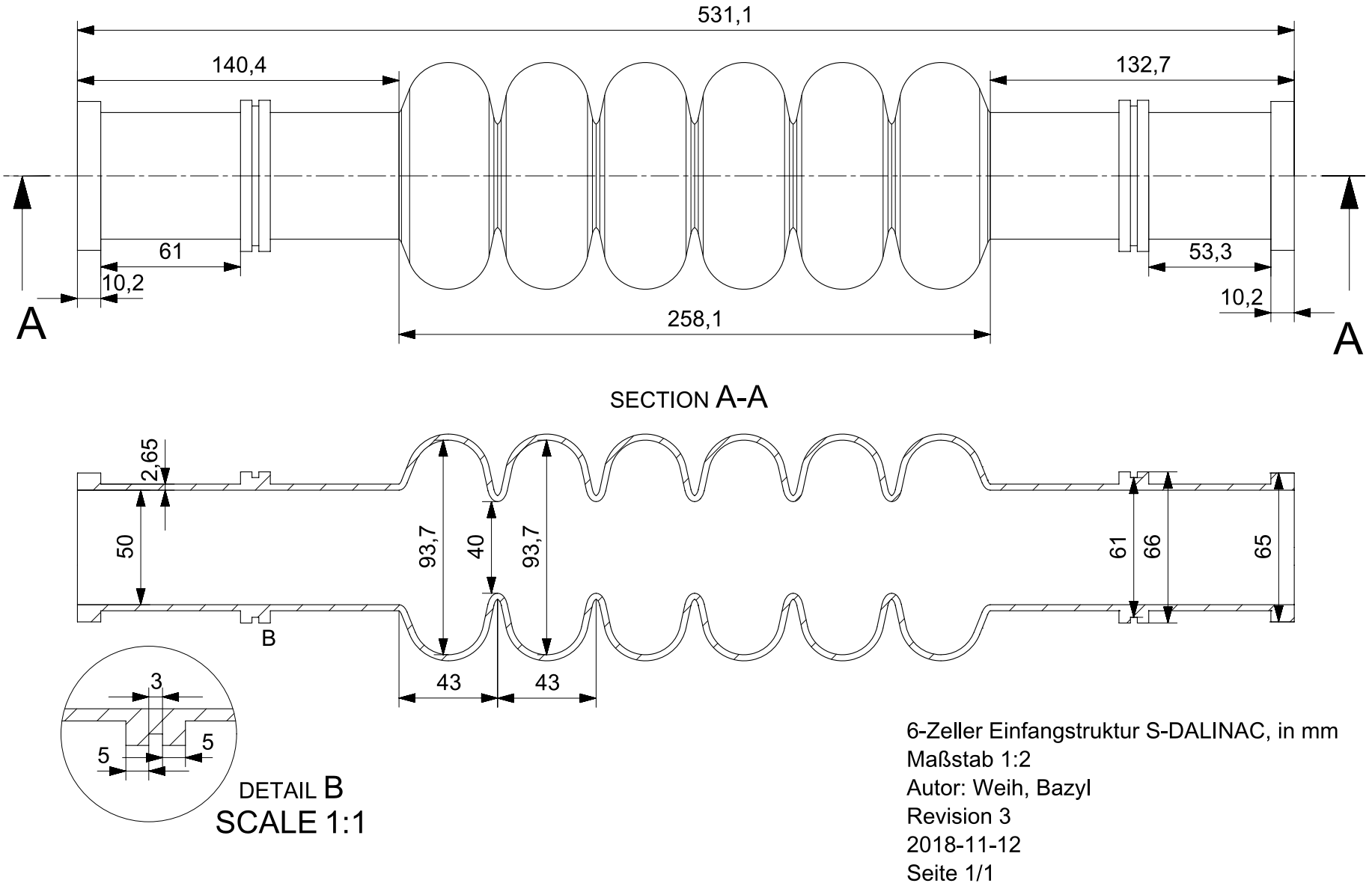

Figure 6.7: Mechanical drawings of the 6-cell cavity model.

7 Conclusion and Outlook

The idea of implementing a 3 GHz SRF 6-cell reduced-β cavity for acceleration of low energy electron beams, with a comparably low average current, has been justified qualitatively and quantitatively. The designed cavity is operated with the $TM_{010};\pi$ mode and allows to accelerate electron beams from an energies of 200 keV up to energies of up to 1.5 MeV, which is by 1 MeV larger compared to the current setup of the capture section of the S-DALINAC. The relative longitudinal energy spread of the beam accelerated in the 6-cell cavity is reduced, while the rms longitudinal energy spread of the output beam is almost 8 times lower compared to the current setup. The new cavity is fully compatible with the present capture section cryostat. The 6-cell cavity is also compatible with the existing tuning system of the cavity after minor modifications.

During the RF design of the cavity, its acceleration efficiency has been reduced for the sake of mechanical longitudinal rigidity of the cavity by increasing the half end-cells iris radius value of the cavity for obtaining a smooth transition between the end-cells and the beam tubes. Nevertheless, the designed accelerating gradient of 5 MV/m can be reached with moderate peak electric fields at the cavity's inside surface. The increased iris radius of the mid-cells provides an advantage in form of a large cell-to-cell coupling coefficient. The large cell-to-cell coupling coefficient, in turn, ensures a stable cavity operation due to a decreased sensitivity of the field flatness to the external mechanical loads.

Longitudinal beam dynamics simulations indicated a wide RF operating phase stability region. In addition, the operating value of the peak electric field on the cavity central axis can be chosen in the range of 7 MV/m up to 20 MV/m depending on the required beam parameters. It is worth noting that the main negative consequence of the cavity constant cell length and the large iris radius of the end-cells is the beam energy loss in the first and the last cavity cells. However, due to low charge of the beam at the S-DALINAC, the effect of the beam energy loss is negligible. In addition, a longitudinal rms energy spread growth of 3 keV of the output beam is being observed. A further minimisation of the rms energy spread growth is feasible by considering the other proposed cavity layouts at the cost of a new cryostat.

The mechanical properties of the 6-cell cavity has been investigated by structural analysis. The computed value of the longitudinal stiffness of the cavity of 5.2 kN/mm indicated that the cavity is rigid enough and stiffening rings are not required. The sensitivity of the resonance frequency to mechanical loads has been estimated and completes the basic mechanical description that is required for the tuning procedures. It is worth noting that the resonance frequency detuning due to the helium pressure fluctuations in the cryostat is expected to be below 40 Hz and is easily compensated by the tuning system of the cavity. In addition, microphonics frequencies of the cavity have been estimated. The obtained data allows to determine potential excitation sources of microphonics for the 6-cell cavity and isolate them if such mechanical vibration sources are present in the S-DALINAC accelerator hall.

The computation results indicated that the 6-cell cavity parameters match the upgrade requirements. Recently, the decision to start the cavity production has been made. Presently, the manufacturing order of the 6-cell cavity has been placed and the manufacturing process will begin early 2019. The cavity delivery to the S-DALINAC is expected to be end of 2019. The first commissioning tests of the cavity are planned early 2020.

This work has shown the feasibility of a reduced-β SRF cavity for capturing a low-energy electron beam with a limited space. By that, it has successfully contributed to accelerator physics providing a valuable alternative to existing principles such as normal conducting β-graded cavities and independently driven single-cell SRF cavities. In future, further optimisations can be carried out when practical restrictions are not present.

Acknowledgements

I would like to thank Prof. Dr.-Ing. Herbert De Gersem for accepting me as a PhD candidate at TEMF, TU Darmstadt, for his great scientific supervision, for supporting my participation in international conferences and for providing me with all the necessary scientific tools. I want to thank Dr. phil. nat. Wolfgang F.O. Müller for the great scientific guidance and for many work related discussions. In addition, I would like to thank Prof. Dr.-Ing. Herbert De Gersem and Dr. phil. nat. Wolfgang F.O. Müller for useful comments on this manuscript. I want to thank Prof. Joachim Enders for productive discussions related to this work and for being the second referee in this thesis.

I thank all TEMF and AccelencE graduate school colleagues for a nice working environment. Especially I want to thank Simon Weih from IKP, who is currently working on a project associated with this work, for valuable discussions related to aspects of a practical realisation of the outcome of this work. I want to thank Dr.-Ing. Wolfgang Ackermann for his valuable advises related to electromagnetic field simulations. Also I thank my former office colleague Dr. Lewin Eidam for a nice working atmosphere.

Finally, I thank my mother Elena and my fiancée Larisa for their never ending support during tough period of life.

This work is dedicated to my mother.

List of Figures

List of Tables

Acronyms

AC Alternating Current

BCS Bardeen–Cooper–Schrieffer

CW Continuous Wave

DC Direct Current

EM Electromagnetic

ERL Energy Recovery Linac

LHC Large Hadron Collider

linac linear accelerator

PT Particle Tracking

RF Radio Frequency

rms root mean square

S-DALINAC Superconducting - DArmstadt LINear ACcelerator

SPG Spin Polarised Gun

SRF Superconducting Radio Frequency

TG Thermionic Gun

Bibliography

[1] W. Panofsky, "Evolution of particle accelerators," *SLAC Beam Line*, vol. 27, no. 1, pp. 36–44, 1997. 1

[2] E. B. Podgorsak, "Particle accelerators in medicine," in *Radiation Physics for Medical Physics*, pp. 609–643, Berlin, Heidelberg: Springer Berlin Heidelberg, 2010. 1

[3] D. Mistry, T. Cross, and C. Weatherup, "RF sub-systems for cargo and vehicle inspection," *Proceedings of IPAC'14*, pp. 1917–1922, jul 2014. 1

[4] V. V. Bezuglov, A. A. Bryazgin, A. Y. Vlasov, L. A. Voronin, A. D. Panfilov, V. M. Radchenko, V. O. Tkachenko, and E. A. Shtarklev, "ILU industrial electron accelerators for medical-product sterilization and food treatment," *Physics of Particles and Nuclei Letters*, vol. 13, pp. 1012–1014, dec 2016. 1

[5] A. Richter, "Operational experience at the S-DALINAC," *Proceedings of EPAC'96*, 1996. 1

[6] M. Herbert, J. Enders, Y. Fritzsche, N. Kurichiyanil, and V. Wende, "Inverted geometry photo-electron gun research and development at TU Darmstadt," *Proceedings of IPAC'18*, 2018. 1

[7] M. Arnold, T. Kürzeder, N. Pietralla, and F. Hug, "Final design and status of the third recirculation for the S-DALINAC," *Proceedings of IPAC'16*, p. TUPOR026, 2016. 3

[8] H. Wiedemann, *Particle accelerator physics*. Springer, 2007. 5, 51

[9] S. Y. Lee, *Accelerator physics*. World Scientific, 2004. 5

[10] T. P. Wangler, *RF linear accelerators*. Wiley-VCH, 2008. 6, 7, 9, 36, 40, 46, 62

[11] I. Veksler, "New method for the acceleration of relativistic particles," *Doklady Akademii Nauk USSR*, vol. 43, no. 8, pp. 346–348, 1944. 7

[12] E. M. McMillan, "The synchrotron — a proposed high energy particle accelerator," *Physical Review*, vol. 68, pp. 143–144, sep 1945. 7

[13] J. D. Jackson, *Classical electrodynamics*. Wiley, 1999. 9

[14] H. Padamsee, J. Knobloch, and T. Hays, *RF superconductivity for accelerators*. Wiley-VCH, 2008. 9, 16, 21, 29, 31, 40, 42, 43, 47, 61

[15] Computer Simulation Technology GmbH. https://www.cst.com/. 12

[16] R. Wideröe, "Über ein neues Prinzip zur Herstellung hoher Spannungen," *Archiv für Elektrotechnik*, vol. 21, pp. 387–406, jul 1928. 13

[17] J. Bardeen, L. N. Cooper, and J. R. Schrieffer, "Theory of superconductivity," *Physical Review*, vol. 108, pp. 1175–1204, dec 1957. 16

[18] A. Gurevich, "Theory of RF superconductivity for resonant cavities," *Superconductor Science and Technology*, vol. 30, p. 034004, mar 2017. 16

[19] H. Padamsee, *RF Superconductivity*. Weinheim, Germany: Wiley-VCH Verlag GmbH & Co. KGaA, mar 2009. 16, 38, 61

[20] A. Grassellino, A. Romanenko, D. Sergatskov, O. Melnychuk, Y. Trenikhina, A. Crawford, A. Rowe, M. Wong, T. Khabiboulline, and F. Barkov, "Nitrogen and argon doping of niobium for superconducting radio frequency cavities: a pathway to highly efficient accelerating structures," *Superconductor Science and Technology*, vol. 26, p. 102001, oct 2013. 16

[21] A. Romanenko, A. Grassellino, A. C. Crawford, D. A. Sergatskov, and O. Melnychuk, "Ultra-high quality factors in superconducting niobium cavities in ambient magnetic fields up to 190 mG," *Applied Physics Letters*, vol. 105, p. 234103, dec 2014. 16

[22] S. Posen, M. Liepe, and D. L. Hall, "Proof-of-principle demonstration of Nb 3 Sn superconducting radiofrequency cavities for high Q 0 applications," *Applied Physics Letters*, vol. 106, p. 082601, feb 2015. 16

[23] F. Hug, A. Araz, R. Eichhorn, and N. Pietralla, "Reducing energy spread of the beam by non-isochronous recirculation at the S-DALINAC," *Proceedings of IPAC'10*, 2010. 17

[24] S. Noguchi, E. Kako, M. Sato, T. Shishido, K. Umemori, K. Watanabe, and Y. Yamamoto KEK, "Development of 2-cell sc cavity system for erl injector linac at KEK," *Proceedings of PAC'09*, 2009. 22

[25] S. A. Belomestnykh, E. P. Chojnacki, M. Liepe, V. Medjidzade, H. Padamsee, P. Quigley, J. Sears, V. D. Shemelin, and V. Veshcherevich, "The Cornell ERL superconducting 2 cell injector cavity string and test cryomodule," *Proceedings of the 2007 IEEE Particle Accelerator Conference (PAC 07). 25-29 Jun 2007*, p. 2572, 2007. 22

[26] R. Heine, "Injector linac for the MESA facility," in *AIP Conference Proceedings*, vol. 1563, pp. 272–275, American Institute of Physics, 2013. 23

[27] C. M. Anderson-Cook, "Practical genetic algorithms," *Journal of the American Statistical Association*, vol. 100, pp. 1099–1099, sep 2005. 23

[28] O. Aberle, S. Marque, R. Losito, J. Tückmantel, E. Chiaveri, R. Hanni, D. Boussard, S. Calatroni, and E. Häbel, "Technical developments on reduced beta superconducting cavities at CERN," tech. rep., CERN, Geneva, Switzerland, mar 1999. 25

[29] W. Singer, "SRF cavity fabrication and materials," *CERN Yellow Report CERN*, vol. 5, pp. 171–207, 2014. 26

[30] B. Aune and et al., "Superconducting TESLA cavities," *Physical Review Special Topics - Accelerators and Beams*, vol. 3, p. 092001, sep 2000. 29

[31] R. Geng, G. Eremeev, H. Padamsee, and V. Shemelin, "High gradient studies for ILC with single-cell re-entrant shape and elliptical shape cavities made of fine-grain and large-grain niobium," in *2007 IEEE Particle Accelerator Conference (PAC)*, pp. 2337–2339, IEEE, 2007. 30

[32] J. Sekutowicz, K. Ko, L. Ge, L. Lee, Z. Li, C. Ng, G. Schussman, L. Xiao, I. Gonin, T. Khabibouline, N. Solyak, Y. Morozumi, K. Saito, and P. Kneisel, "Design of a Low Loss SRF Cavity for the ILC," in *Proceedings of PAC'05*, pp. 3342–3344, IEEE, 2005. 30

[33] F. Brinker, "Commissioning of the european XFEL injector," *Proceedings of IPAC'16*, p. TUOCA03, 2016. 30

[34] D. Proch, "The TESLA cavity: design considerations and RF properties," *Proceedings of the Sixth Workshop on RF Superconductivity*, 1993. 31

[35] R. W. J. Sekutowicz, "A design of a 3rd harmonic cavity for the TTF 2 photoinjector," *TESLA-FEL 2002-05*, 2002. 31

[36] J. Shi, S. Zheng, R. Rimmer, H. Wang, D. Li, and H. Chen, "Comparison of measured and calculated coupling between a waveguide and an RF cavity using CST Microwave Studio," *Proceedings of EPAC'06*, vol. C060626, pp. 1328–1330, jun 2006. 32

[37] L. J. Foged, M. A. Saporetti, M. S. Castañer, E. Jorgensen, P. Voigt, F. Calvano, and D. Tallini, "Measurement and simulation of reflector antenna," in *9th European Conference on Antennas and Propagation (EuCAP)*, pp. 1–5, IEEE Computer Society, 2015. 32

[38] D. Li, J. W. Staples, and S. P. Virostek, "Detailed modelling of the SNS RFQ structure with CST Microwave Studio," *Proceedings of LINAC'06*, 2006. 32

[39] A. Facco, "Low and medium beta SC cavities," *Proceedings of EPAC'04*, 2004. 38

[40] S. An, "Superconducting RF cavity frequency and field distribution sensitivity simulation," *Proceedings of PAC'05*, 2005. 38

[41] A Space Charge Tracking Algorithm (ASTRA). http://www.desy.de/~mpyflo/. 51

[42] ANSYS. https://www.ansys.com/. 61

[43] G. Stupakov and G. Penn, *Classical mechanics and electromagnetism in accelerator physics*. Springer, 2018. 61

[44] I. G. N. Solyak, H. Edwards and M. Foley, "Development of the 3.9 GHz 3rd harmonic cavity at FNAL," *Proceedings of SRF'03*, 2003. 65

[45] S. Weih, M. Arnold, J. Enders, N. Pietralla, D. Bazyl, W. F. O. Müller, and H. De Gersem, "Development of an improved capture section for the S-DALINAC injector," *Proceedings of IPAC'18*, 2018. 68

[46] D. Bazyl, H. De Gersem, W. F. O. Müller, J. Enders, and S. Weih, "A 3 GHz SRF reduced-beta cavity for the S-DALINAC," *Proceedings of IPAC'18*, 2018. 68